Clays and Clay Minerals, Vol. 63, No. 1, 1–14, 2015.

MODIFICATION OF MONTMORILLONITE WITH ALKYL SILANES AND FLUOROSURFACTANT FOR CLAY/FLUOROELASTOMER (FKM) NANOCOMPOSITES

MARYAM KHAJEHPOUR, GENARO A. GELVES, AND UTTANDARAMAN SUNDARARAJ*

Department of Chemical and Petroleum Engineering, University of Calgary, Calgary, Canada, T2N 1N4

Abstract—The main objective of the present work was to functionalize nanoclays with organosilanes and surfactant in order to facilitate the dispersion of the nanofillers in the host fluoroelastomer (FKM) polymer matrix. Better dispersion was achieved by improving interaction between the clay polymer nanocomposite (CPN) constituents. The first part of this study investigated modification of montmorillonite (Mnt) using different saturated and unsaturated alkyl silanes and an alkyl hydrocarbon ammonium quaternary surfactant. Silicon magic angle spinning nuclear magnetic resonance spectroscopy, thermal gravimetric analysis (TGA), elemental analysis, X-ray diffraction (XRD), and Fourier transform infrared spectroscopy were used to characterize the silane-grafted clays. Results indicated that the amount of silane grafted depended on the specific structure of the silane. Silane-grafted Mnt was also modified with ionic surfactants intercalated between the clay layers. A 169% increase in the clay basal spacing (from initial spacing of 10.0 Å to 26.9 Å) was achieved. The second part of the study successfully synthesized FKM nanocomposites containing custom-functionalized Mnt, with the aim of producing reinforced high-performance materials. The effects of clay modification on the morphology and thermal properties of the CPN were studied using XRD, TGA, scanning electron microscopy, and transmission electron microscopy. The CPN made with the modified clay exhibited greater thermal stability than the CPN of the commercially available modified Mnt, with a degradation onset point ~40ºC higher.

Key Words—Clay, Fluoroelastomer, Montmorillonite, Nanocomposite, Silane Grafting.

INTRODUCTION

In recent decades, interest in inorganic nanofiller polymer nanocomposites has increased (Herrera *et al.*, 2004; He *et al.*, 2005). The most significant advantage of nanofillers over conventional micro-particles is the remarkable improvement in the properties of the final clay polymer nanocomposite (CPN), with very low filler content, due to the interaction between polymer and filler at the nano scale (Modesti *et al.*, 2005; Borse and Kamal, 2006; Al-haj Ali and Elleithy, 2011). Among nanofillers, silicate layers have attracted increased interest since the 1950s, because of their interesting structural features and the high aspect ratios of the nanoclays (Dennis *et al.*, 2001; Herrera *et al.*, 2004; Shanmugharaj *et al.*, 2006; Shen *et al.*, 2007; Bergaya *et al.*, 2011).

Incorporation of nanoclay can enhance the mechanical, thermal, and barrier properties of polymers (Wu *et al.*, 2004; Shanmugharaj *et al.*, 2006; Mingliang and Demin, 2008). The key factor in this improvement is the chemical compatibility and uniform dispersion of the clay layers within the host polymer (Dennis *et al.*, 2001; Chen *et al.*, 2005; Paul and Robeson, 2008; Qian *et al.*, 2009; Bergaya *et al*., 2013; Lambert and Bergaya, 2013). A complete delamination of the layered clays increases the interfacial interaction between the polymer chains and the nanoclays, leading to exfoliated clay/polymer nanocomposites (Xu *et al.*, 2009; Bergaya *et al.*, 2013; Lambert and Bergaya, 2013). Although the hydrophilic nature of silicate layers is generally incompatible with organic polymers (Park *et al.*, 2004; He *et al.*, 2005; Shanmugharaj *et al.*, 2006; Shen *et al.*, 2007; Mingliang and Demin, 2008; Joo *et al.*, 2008; Xu *et al.*, 2009; Das *et al.*, 2011; Heinz, 2012), with active sites such as hydroxyl groups and exchangeable interlayer cations, clay can be modified to be compatible with an organic polymer matrix (Shanmugharaj *et al.*, 2006).

Previous studies have demonstrated that the superior properties of CPN depend on the dispersion of the clay, the aspect ratio, and the interfacial interaction between the clay and polymer matrix (Mingliang and Demin, 2008; Qian *et al.*, 2009; Heinz, 2012). The size of large clay particles and the low affinity of natural clays to most organic polymers diminish their reinforcing ability in CPN (Bergaya *et al.*, 2011). It is important to make the particles compatible *via* organophylization to facilitate their intercalation with the hydrophobic polymer macromolecules (He *et al.*, 2005), in order to improve the clay dispersion in the matrix and enhance efficiency in modifying the final properties (Akelah and Moet, 1996; Zhu and Xanthos, 2004; Park *et al.*, 2004; He *et al.*, 2005; Joo *et al.*, 2008; Qian *et al.*, 2009; Daniel *et al.*, 2008; Monasterio, 2010; Das *et al.*, 2011; Bergaya *et al.*, 2011). While both the basal spacing and the

* E-mail address of corresponding author:
u.sundararaj@ucalgary.ca
DOI: 10.1346/CCMN.2015.0630101

chemical affinity of silicate layers are important for their dispersion, two approaches are used for clay modification: interlayer ion exchange with surfactant, and treatment of functional groups on the clay surface and edges by organic compounds such as silane (Hussain *et al.*, 2006; Shen *et al.*, 2007; Joo *et al.*, 2008; Daniel *et al.*, 2008; Qian *et al.*, 2009; Monasterio, 2010; Bergaya *et al.*, 2011).

Montmorillonite (Mnt) is one of the most commonly studied clay minerals for polymer nanocomposites and is also the one used most in different applications of CPN (Bergaya and Lagaly, 2001; Bergaya *et al.*, 2011). One of the most successful ways to organophilize clay is by silane grafting through the reaction between the alkoxy groups of silane and the hydroxyl groups of Mnt (Bergaya *et al.*, 2011). Grafting of clays with bifunctional silanes not only improves interfacial interaction but also enables chemical reactions between clays and functional groups in the macromolecules (Chen *et al.*, 2005; Xu *et al.*, 2009). The end groups of the grafted silanes can react with monomers before polymerization and/or with polymer chains during melt mixing or vulcanization (Qian *et al.*, 2009).

The thermal stability of Mnt/polymer nanocomposites can be improved by replacing ion-exchanged ammonium intercalants with covalently bonded silane (Qian *et al.*, 2009; Xu *et al.*, 2009). Enhanced mechanical properties and an increased crystallization temperature are expected as a result of edge grafting of clay with silane (Xu *et al.*, 2009). While the size of the surfactant molecules is much larger than the cations that normally occur between the silicate layers in pristine clay, the replacement of cations with surfactant should help to open up the interlayer spaces.

The reinforcement of elastomers through the incorporation of clay has a wide range of applications, due to their light weight, greater 'processability' relative to metals (Mittal *et al.*, 2011), and enhanced mechanical properties compared to traditional elastomers (Lakshminarayanan *et al.*, 2009; Mittal *et al.*, 2011). Although many CPN studies with thermoplastics and thermosets have been carried out, much less attention has been paid to elastomers (Hrachova, 2008). Most applications of elastomers, however, are impossible without reinforcement (Wu *et al.*, 2004). Fluoroelastomer (FKM) is a type of elastomer that shows excellent performance when high temperatures and chemical resistance are required (Ameduri *et al.*, 2001). These materials are proposed for applications where elastic behavior is needed for severe environments demanding special improved material performance such as high-temperature stability and oil resistance (Valsecchi *et al.*, 2011).

In the present study, modification of Mnt, to make it more compatible with and well dispersed in FKM, was investigated using both organosilane as a chemical compatibilizer and surfactant as a dispersion aid. The effectiveness of silane grafting and the use of surfactant for increasing intercalation in the clay were investigated here. The modification was carried out using saturated and unsaturated alkyl silanes: octadecyltrimethoxysilane, 7-octenyltrimethoxysilane, and 10-undecenyltrimethoxysilane. A quaternary ammonium surfactant was used as a cation exchanger. By incorporating the modified nanoclay in FKM, the nanocomposite was produced and its properties studied. The unsaturated functionalities in the silane-modified clays provide for better interaction between clays and polymers, and make it easier to fabricate reinforced elastomer nanocomposites that are vulcanized through free radical mechanisms.

EXPERIMENTAL

Materials

Montmorillonite clay, Nanofil 116 (pure unmodified Mnt), and Cloisite 20A (organo-modified Mnt with dimethyl dihydrogenated tallow quaternary ammonium surfactant) were obtained from Southern Clay Products Inc, Texas, USA. The structure of the unmodified Mnt is available from the literature (Herrera *et al.*, 2004; He *et al.*, 2005; Hussain *et al.*, 2006). Octadecyltrimethoxysilane (90%) was purchased from Sigma-Aldrich Chemistry Company Inc., Ontario, Canada, and 7-octenyltrimethoxysilane (95%) and 10-undecenyltrimethoxysilane from Gelest, Inc., Pennsylvania, USA. Masurf® FS-1620 fluoroaliphatic quaternary fluorosurfactant and Viton® fluoroelastomer (grade GF-200S) were supplied by Mason Chemical Company, Ohio, USA and DuPont, Ontario, Canada, respectively.

Clay modification

The two main methods of Mnt modification were examined here, as illustrated in Figure 1: (1) silane grafting, and (2) ion exchange with surfactant. Silane grafting is the reaction of alkoxysilane Si-O-R functionalities with hydroxyl groups on the edges of the clay forming Si−O−Si bridges with elimination of alcohols (R-OH) (Bergaya *et al.*, 2011). Typically, adding surfactant reduces the surface and interfacial tension. In the present study, three different silanes were used for silylation: octadecyltrimethoxysilane, 7-octenyltrimethoxysilane, and 10-undecenyltrimethoxysilane. The exchangeable cations between the clay layers were replaced by a cationic surfactant (trimethyloctadecyl ammonium chloride) to increase the basal spacing between layers.

With both silane and surfactant used in Mnt modification, two different procedures were tested. In method 1, the surfactant was added first, followed by the silane. In method 2, silane was added to the clay prior to the surfactant. Modification procedures, using 100 mL of a mixture of methanol (90 vol. %) and water (10 vol. %) as the dispersing medium for 1 g of clay, were carried out at 70ºC. 1 mL of the organosilane and/or surfactant was used per gram of clay and the times for the silane

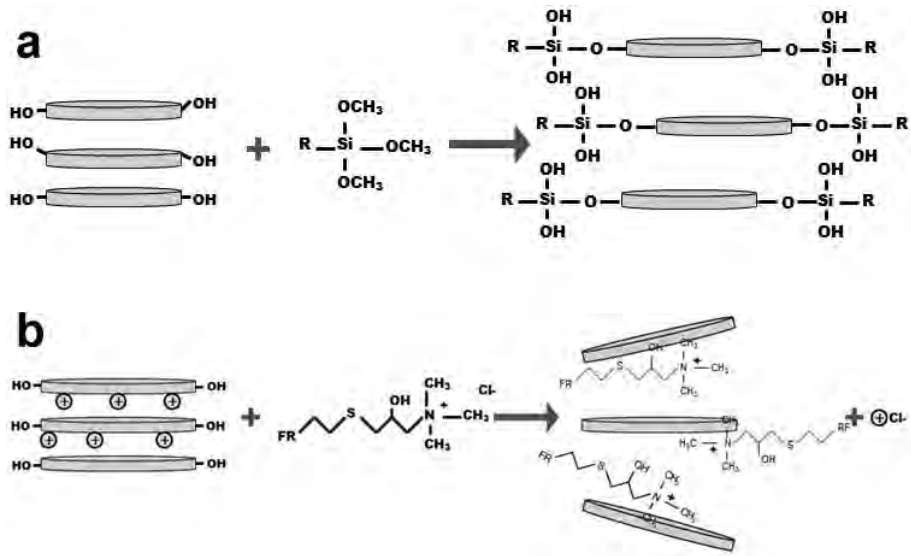

Figure 1. Schematics for (a) Mnt modification with alkylsilanes and (b) Mnt modification with surfactant.

reaction and cation exchange with the surfactant were 4 h and 1 h, respectively. Above a certain concentration of surfactant, no effect was found of concentration on the layer spacing, and 1 mL of surfactant was more than the critical amount required for this system. The modified clay was dried in a vacuum oven at 60ºC for 24 h, milled in a mortar and sieved through a mesh to <63.5 μm with a USA standard test sieve.

Clay polymer nanocomposite preparation

Organically treated Mnt from the previous phase was used in the preparation of the FKM nanocomposite. Melt intercalation is the most favored method in industry (Dennis *et al.*, 2001; Hrachova *et al.*, 2008; Al-haj Ali and Elleithy, 2011) and, as such, was chosen for the production of CPN in this work. Two common, commercially available fillers used for making elastomeric nanocomposites are carbon black and Cloisite 20A (Lakshminarayanan *et al.*, 2009; Bergaya *et al.*, 2013; Lambert and Bergaya, 2013). Some comparisons were made between the results using these fillers and those of the synthesized clays using the same mixing conditions.

The melt was compounded using a Haake internal mixer. The elastomer was first masticated for 3 min, and the clay (at a concentration of 9.1 wt.%) was added to the polymer and melt mixed for ~17 min. The mixer temperature was set at 50ºC; elastomer mastication caused the melt temperature to rise to 80ºC, however. The modified clay dispersion in the polymer matrix is illustrated schematically in Figure 2.

Characterization

A TA Instruments Q500 series (New Castle, Delaware, USA) thermogravimetric analyzer was used to determine the thermal stability of the modified clay and CPN. The thermogravimetric analysis (TGA) testing was done on a 10-mg sample under a nitrogen (N_2) atmosphere at a heating rate of 20ºC/min from 30ºC to 850ºC. Fourier transform infrared (FTIR) spectroscopy was used to characterize the modified clay. Clay samples were prepared as potassium bromide (KBr) discs (~20 mm in diameter) using compression molding of ~2 mg of the clay mixed with KBr. The FTIR spectroscopy was run on a Nicolet Nexus 470 FTIR ESP (Thermo Fisher Scientific Inc., Massachusetts, USA) with a cesium iodide (CsI) detector. Solid-state silicon magic angle spinning nuclear magnetic resonance (^{29}Si MAS NMR) spectroscopy was performed with a Bruker AMX spectrometer (Billerica, Massachusetts, USA), operating at an applied magnetic field of 7.05 T, using a BL4 magic-angle spinning probe and 4 mm (OD) zirconia oxide rotors. The ^{29}Si MAS NMR spectra were referenced to an external sample of 4,4-Dimethyl-4-Silapentane-1-Sulfonic acid (DSS) at 8.8 ppm. Clay samples were packed and spun at the magic angle at a frequency of 4.0 kHz and the delay time was 10 s. Elemental analysis was achieved using a Perkin Elmer Model 2400 series II instrument (Waltham, Massachusetts, USA) to analyze the CHN (carbon, hydrogen, nitrogen) content.

The basal spacing of clay layers and the intercalation level of clay/FKM nanocomposites were determined by X-ray diffraction (XRD) (Rigaku Ultima III, Scottsdale, Arizona, USA) with CuKα radiation and λ = 1.54 Å. The X-ray diffractometer has a theta-theta goniometer with 185 mm radius. Scans were performed over the range of $2 < º2\theta < 10$ with step size of 1º and a scan rate of 1º/min. For characterization by XRD, the CPN samples, with diameters of 25 mm and thicknesses of 2 mm, were compression molded at 90ºC and 6 MPa for 2 min. The generator was operated at 40 kV and 44 mA. Transmission electron microscopy (TEM) and scanning electron microscopy

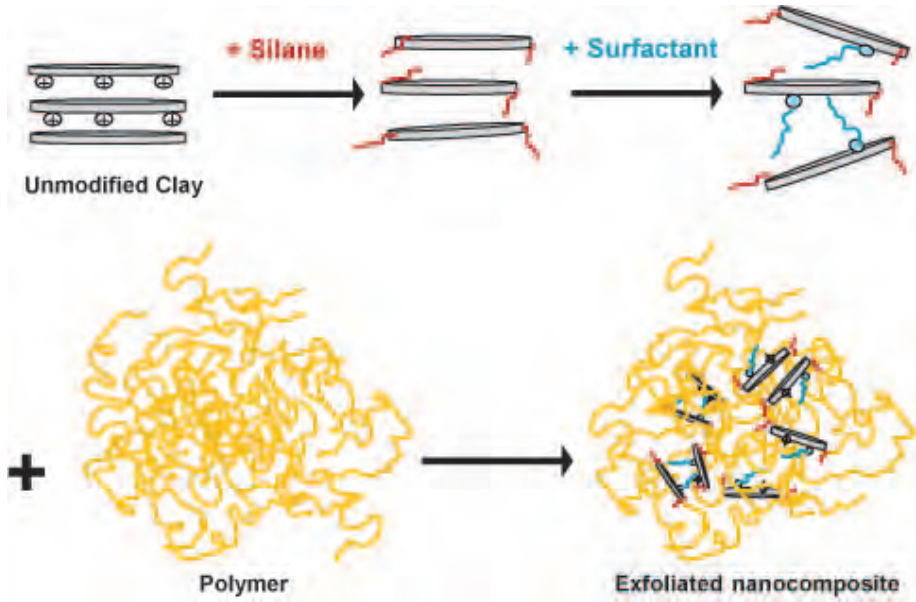

Figure 2. Preparation of modified clay/FKM nanocomposite.

(SEM) were used to examine the morphology of the CPN. For the TEM a Tecnai TF20 G2 FEG-TEM instrument (FEI, Hillsboro, Oregon, USA) was used at 200 kV acceleration voltage with a standard single-tilt holder with a spot size between 3 and 4 nm. Cryo ultra-microtome sectioning of the samples for TEM was done by means of a Leica EM FC6 device (Concord, Ontario, Canada) at −160ºC using liquid nitrogen. The TEM images were captured on a Gatan UltraScan 4000 CCD (Gatan, Pleasanton, California, USA) camera at 2048 × 2048 pixels from samples with thicknesses of 50−70 nm. The SEM analysis was carried out using an SEM, FEI XL30 (FEI, Hillsboro, Oregon, USA) with adjustable voltage between 0.5 and 30 kV. The accelerating voltage of the beam was 20 kV and the secondary electron mode with a spot size of 4 nm were used for SEM imaging. The rectangular 2 mm × 10 mm surfaces of the samples for SEM imaging were trimmed with the microtome and were coated with gold prior to examination.

RESULTS AND DISCUSSION

Clay modification

Silane grafting. The three methoxy groups in the silane structure can be hydrolyzed in the presence of methanol/water mixtures, and the resulting hydroxyl (OH) groups enable grafting reactions with the OH groups on the clay. In this work, silane compounds, containing saturated (octadecyltrimethoxysilane) and unsaturated (10-undecenyltrimethoxysilane, 7-octenyltrimethoxysilane) alkyl chains, were grafted successfully to Mnt and their effects were compared.

From the TGA results (Figure 3) for unmodified and silane-modified Mnt, and Cloisite 20A, a loss of mass below 200ºC was observed, which corresponds to the residual solvents, organics, and gases absorbed to the clay. In the range 100−400ºC, pristine Mnt typically showed loss of water absorbed inside the platelets (interlayer) and of water hydrating the cations that were intercalated in the interlayer. The dehydroxylation of the aluminosilicate typically occurred between 500 and 700ºC (Xie *et al.*, 2001).

The onset temperature of degradation (Table 1) is defined here as the temperature at which the modified clays lost 5 mass%. Assuming that the same amount of dehydroxylation occurred for silane-grafted Mnt, the difference between the mass lost at temperatures between 200 and 700ºC would correspond to the amount of silane grafted on Mnt for each compound. Moreover, the specific molar amount of silane grafted on the functionalized clays can be calculated from the mass loss percentage using this formula (Table 1):

$$X = \frac{(\text{mass\% loss of modified clay}) - (\text{mass\% of pure Mnt})}{100 - (\text{mass\% loss of modified clay}) - (\text{mass\% of pure Mnt})} \times \frac{1}{MW}$$

Where X is the molar amount of grafted silane per gram of Mnt, and MW is the molecular weight of the organosilane used as the modifier. The unmodified Mnt used in the present study exhibited a mass loss of 1.8% up to 200ºC and of 8.2% between 200 and 700ºC. The TGA of silylated clays showed that the most significant mass loss took place at 460ºC for 7-octenyltrimethoxysilane-modified Mnt (Figure 3b), 505ºC for octadecyltrimethoxy-silane-modified Mnt (Figure 3c), and 510ºC for 10-undecenyltrimethoxysilane-modified Mnt (Figure 3d).

The amount of silane grafted onto modified clays, calculated according to the mass-loss results (Table 1),

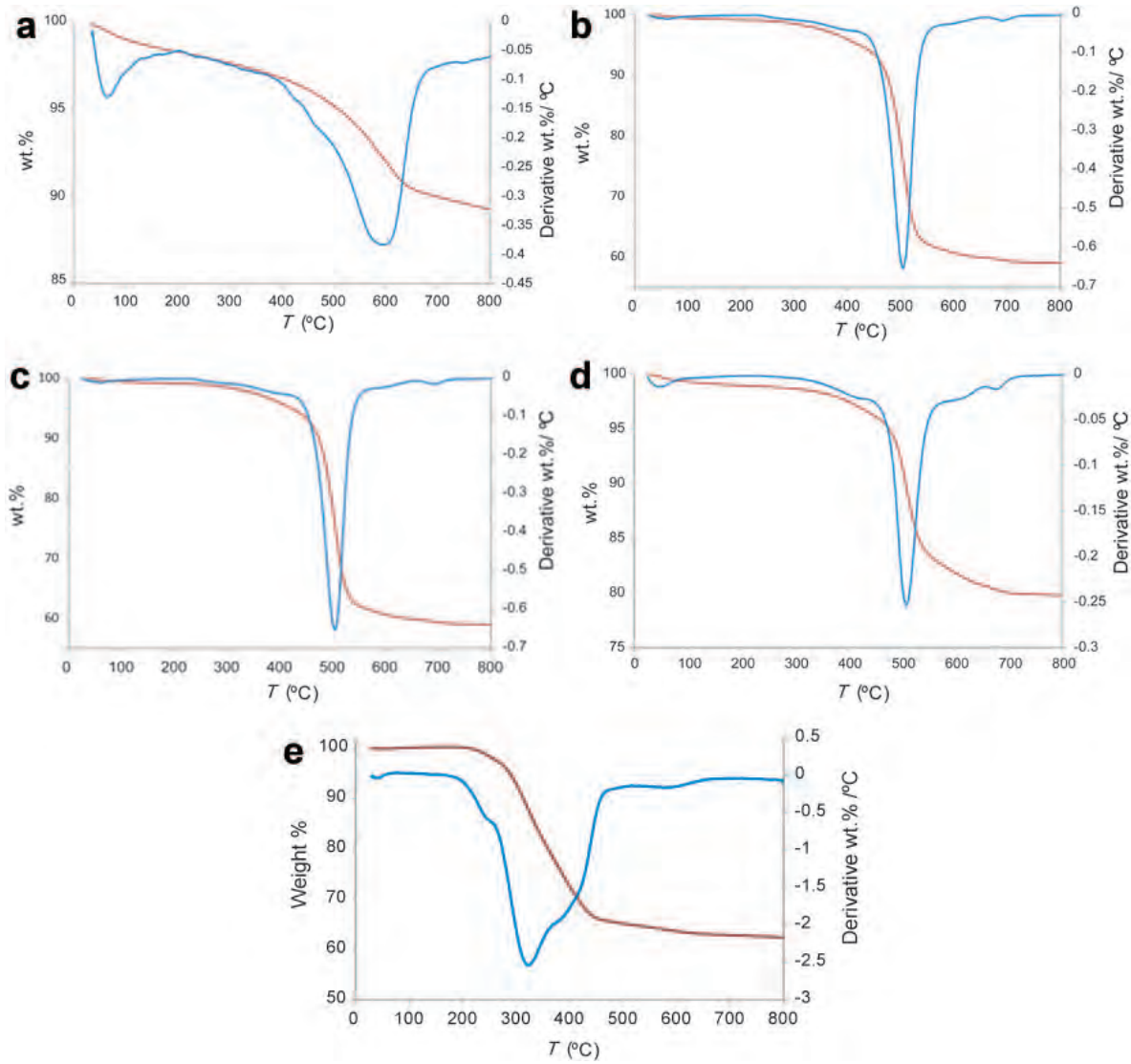

Figure 3. TGA and differential TGA results for: (a) unmodified Mnt; (b) Mnt modified with 7-octenyltrimethoxysilane; (c) Mnt modified with octadecyltrimethoxysilane; (d) Mnt modified with 10-undecenyltrimethoxysilane; and (e) Cloisite 20A.

indicates the differences in grafting-reaction efficiency for different organosilanes. Silane-grafted Mnt over the temperature range 200−700ºC showed mass losses of 13.1% for 7-octenyltrimethoxysilane-Mnt, 18.9% for 10-undecenyltrimethoxysilane-Mnt, and 39.8% for octadecyltrimethoxysilane-Mnt. Considering these amounts alongside ~8.2% of mass-loss for the unmodified Mnt over the same temperature range, the moles of grafted silane per gram of clay for each modified clay were calculated. The results confirm that of the three

Table 1. Degradation onset points for modified Mnt and the amount of silane reacted with the clay surface for different organosilane modifiers.

Clay	Temperature at 5% mass loss (ºC)	Mass loss % (200−700ºC)	mmoles of silane/g of Mnt
10-undecenyltrimethoxysilane-Mnt	475	18.9	0.849
Octadecyltrimethoxysilane-Mnt	420	39.8	1.233
7-octenyltrimethoxysilane-Mnt	300	13.1	0.64
Cloisite 20A	287	38	–

Table 2. Elemental analysis of unmodified and silane-modified Mnt.

Clay	Element (%)	
	Carbon	Hydrogen
Mnt	0.96	1.50
Octadecyltrimethoxysilane-Mnt	31.86	5.78
10-undecenyltrimethoxysilane-Mnt	13.08	2.57
7-octenyltrimethoxysilane-Mnt	9.62	2.09

organosilanes, the most efficient grafting reaction was with octadecyltrimethoxysilane; 7-octenyltrimethoxysilane grafted least.

The differential TGA (D-TGA) results show that the thermal degradation of unmodified Mnt occurred in the range 400 to 700ºC, due to the dehydroxylation of the structural OH units of Mnt. Silane-modified Mnt exhibited decomposition in the range between 400 and 600ºC. The thermal dehydroxylation of the aluminosilicate, therefore, should overlap with the decomposition of the silane from the clay surface. For comparison purposes, the onset temperature, based on the same criteria for a commercial Mnt modified with dimethyl dihydrogenated tallow quaternary ammonium surfactant (i.e. Cloisite 20A), is 287ºC (Table 1). The results show clear evidence of better thermal modification of the clay by the silanes, relative to that of Cloisite 20A. The TGA and D-TGA results indicate that the order of thermal stability for the silane-modified clays was: 10-undecenyltrimethoxy > octadecyltrimethoxy >> 7-octenyltrimethoxy > Cloisite 20A.

The elemental analyses (Table 2) confirm silane grafting to the surfaces of the clays, and indicate the amount of modifier grafted to the clays. Note that the amount of silane grafting was greater for silanes with longer chains.

The FTIR spectra of pure Mnt and of silylated clays (Figure 4) show evidence of organosilane grafting of the modified Mnt. Peaks in the range 1130−1000 cm^{-1} and the signal at ~1430 cm^{-1} were attributed to Si−O−Si bonds (Marynick and Dixon, 1977; Pramanik *et al.*, 2013) which existed for both the unmodified and modified clays. The IR peaks in the ranges 1470−1400 cm^{-1} and 1450−1410 cm^{-1} are generally attributed to combination of C−H stretching and C−O stretching in carbonate, respectively, however (Stuart, 2004; Smidt *et al.*, 2011). The signals in this region may, therefore, be considered as overlapped signals related to organosilane alkyl chains and the Mnt. More specifi-

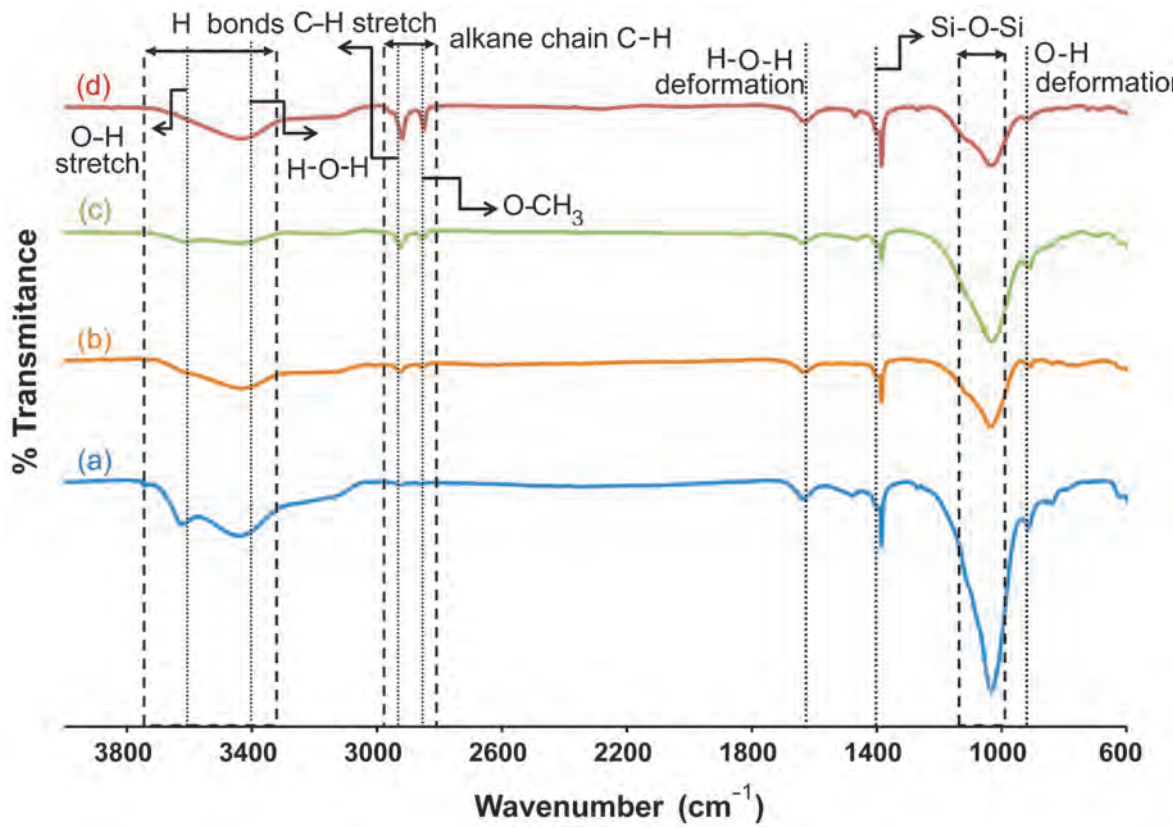

Figure 4. FTIR results for (a) unmodified Mnt, and Mnt modified with (b) 7-octenyltrimethoxysilane, (c) 10-undecenyltrimethoxysilane, and (d) octadecyltrimethoxysilane.

cally, the peak at ~1040 cm^{-1} corresponded to Si−O−Si stretching (Lakshminarayanan *et al.*, 2009). The absorption at ~900 cm^{-1} was related to OH deformation, which is linked to cations; the peak at 1635 cm^{-1} corresponded to hydrogen-oxygen-hydrogen (H-O-H) deformation (Bukka and Miller, 1992).

Generally, the absorption peaks in the range 2960−2850 cm^{-1} can be attributed to C−H (carbon–hydrogen) from alkyl chains (Morrison and Boyd, 1983). The peak at 2940 cm^{-1} showed the C−H stretch (Orprecio and Evans, 2003) for C atoms that are bound to OH groups. The peak at 2830 cm^{-1} confirmed the oxygen-methyl (O−CH_3) bond (Zumdahl, 1999), but this may also indicate unreacted methoxy groups of the silane. The peak at 2850 cm^{-1} may also be related to CH_2 stretching modes (He *et al.*, 2004), which is again an indication of alkyl chains of the grafted organosilanes. A small broad peak at ~3100 cm^{-1} corresponds to O−H stretching (Dong *et al.*, 1997), whereas the broad peaks in the range 3500−3200 cm^{-1} can be assigned to intermolecular H bonds, which could be seen for modified and unmodified clays (Coates, 2000). Hydrogen bonding is possible between nitrogen or hydroxyl groups of the molecules of the modifiers, *i.e.* organosilane and surfactant, with hydroxyl groups of the neighboring molecules or remaining OH on the clay surface. The peak at 3400 cm^{-1} corresponded to H−O−H hydrogen-bonded water (Bukka and Miller, 1992), which existed in octadecyltrimethoxy silane-modified clay. This may be due to the O−H bonds on the platelet surface and substitution of methoxy groups of the silane after synthesis. The same is true of the peak at 3634 cm^{-1}, which can be attributed to O−H stretching vibration (Bukka and Miller, 1992).

^{29}Si MAS NMR spectroscopy (Figure 5) was used to confirm the grafting of Mnt with different silanes. The chemical shifts are summarized for both the unmodified and silane-modified clays (Table 3). The spectrum for unmodified Mnt displayed only one peak at −86.7 ppm; whereas silane-grafted Mnt exhibited additional peaks at −68.2 ppm and −61.1 ppm for octadecyltrimethoxy silane, −55.1 ppm and −44 ppm for undecenyltrimethoxy silane, and −53.4 ppm and −51.2 ppm for octenyltrimethoxy. The resonance signal at −86.7 ppm corresponded to Q^3 [$Si(OSi)_3O$(Al, Mg)], which is characteristic of the silicon atom forming the layered silicate. No signal was detected for Q^4 [$Si(OSi)_4$], indicating that silica was not present in the unmodified Mnt while also demonstrating the purity of the unmodified Mnt (Huskic *et al.*, 2013). Generally, signals in the range −80 to −120 ppm show Q^1, Q^2, Q^3, or Q^4 silicon types with four attached oxygens which by substitution of any methyl group would be shifted to T types in the range −70 to +10 ppm (Process NMR Associates webpage, www.process-nmr.com, 2012). The resonance signals that appeared at ~−60 to −70 ppm for octadecyltrimethoxysilane-Mnt correspond to T^3 [$Si(OSi)_3R$] (Abbehausen *et al.*, 2010), where R corresponds to the alkyl chain of the silane used for grafting. The signals at −55 ppm and −44 ppm for undecenyltrimethoxysilane-Mnt are due to T^2 [$Si(OSi)_2(OH')R$] and T^0, respectively. T^0 is an indication of hydrolyzed intermediate with no condensed Si−OH groups (Abbehausen *et al.*, 2010). Also, the signals between −50 and −55 for the octenyltrimethoxysilane-Mnt should be related to T^2 and T^3 [$Si(OSi)_3R$]. Taking the NMR spectra into account, the appearance of new signals and decrease in the intensity of Q^3 signals confirms the condensation reaction of the surface silanol groups of the clays (Huskic *et al.*, 2013) and grafting of different organosilanes on Mnt. Assuming the small signals at −100 ppm to be an indication of Q^4 means that limited grafting with condensation of silanes occurred as a result of clay modification for the modified clays. The appearance of T^n signals is further evidence of grafting reactions. The results clearly indicate that more grafting occurred for octadecyltrimethoxysilane-Mnt and undecenyltrimethoxysilane-Mnt and less for octenyltrimethoxysilane-Mnt, while the intensity of Q^3 hadn't changed noticeably for octenyltrimethoxysilane-Mnt. In addition, signals for T^2 and T^3 for this sample can also be considered as evidence of grafting.

Basal spacings for different silane-grafted Mnt and the pristine unmodified Mnt (Table 4) can be calculated

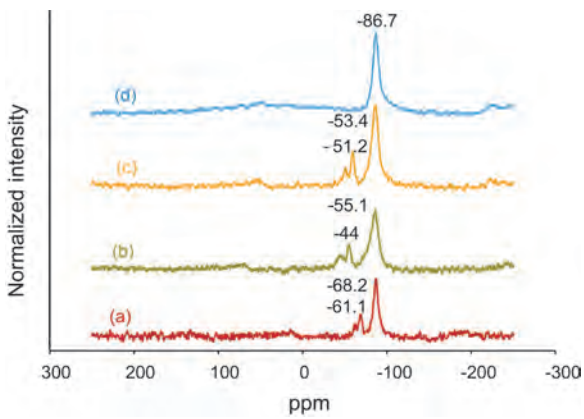

Figure 5. NMR results for: (a) Mnt modified with octadecyltrimethoxysilane; (b) Mnt modified with 10-undecenyltrimethoxysilane; (c) Mnt modified with 7-octenyltrimethoxysilane; and (d) unmodified Mnt.

Table 3. NMR chemical shifts for silane-modified and unmodified Mnt.

Sample	Chemical shifts (ppm)
Mnt	−86.7
Octadecyltrimethoxysilane-Mnt	−86.7, −68.2, −61.1
10-undecenyltrimethoxysilane-Mnt	−86.7, −44, −55.1
7-octenyltrimethoxysilane-Mnt	−86.5, −53.4, −51.1

Table 4. Basal spacing for modified and unmodified Mnt.

Sample	d_{001} (Å)
Mnt (Norrish, 1954; Lakshminarayanan *et al*., 2009)	9.5−11.7
Mnt (experimental result)	10.03
Octadecyltrimethoxysilane/Mnt	12.2

from wide-angle XRD results using Bragg's law, $2d(\sin\theta) = n\lambda$, where d is the basal spacing (Å), θ is the diffraction angle (º), and λ is the wavelength (Å), 1.54 Å for CuKα radiation. The d value for Mnt has been reported in the literature as 9.5−11.7 Å (Norrish, 1954; Lakshminarayanan *et al.*, 2009). The results of the present study indicate that the initial interlayer d_{001} spacing (i.e. 10.0 Å) increased slightly after silane grafting. Some silanes, therefore, had been intercalated between clay layers while the rest of the silanes were grafted at the edges *via* a condensation reaction with hydroxyl groups (Shanmugharaj *et al.*, 2006).

Effect of surfactant modification

Previous studies on the silane modification of clay reported the possibility of a blockage of the interlayer spaces between the clay platelets by silane molecules grafted on the clay edges (*e.g.* Shanmugharaj *et al.*, 2006). Experiments with a quaternary ammonium surfactant were carried out to determine if the silanes at the clay edges prevent intercalation. The outcomes of different clay-treatment procedures were different, depending on the order of the (two) steps of modification (*i.e*. the order in which the silane and the surfactant were added).

The XRD results (Figure 6) show a significant increase in the basal spacing for the Mnt that was modified with both silane and surfactant compared to that of unmodified clay. The basal spacing (d_{001}) had increased considerably, indicating that the surfactant was intercalated successfully in the clay. While the modification of the clay with both species can be carried out in either order to result in intercalated/silanated clay, a larger interlayer space was achieved with method 1. Method 1 showed an additional expansion of 3 Å over method 2, an increase of ~30% based on the initial basal spacing. The reason for the difference may be that the surfactant increased the interlayer space initially in the first method; however, with the addition of silane, some surfactant was flushed out from the interlayer spaces.

The FTIR results for both the modified and unmodified Mnt (Figure 7) show the effects of the two methods of modification on the chemical bonds in the clays. The peaks in the range 3000−2800 cm^{-1} show the alkyl chain of both the surfactant and the silane, indicating their attachment to the clay surface. The decrease in the intensity of peaks at 3600−3200 cm^{-1} region, which corresponds to stretching vibration H-bonded Si−OH groups, compared to unmodified Mnt is due to organic surfactant intercalated into the Mnt interlayers. The decrease in peaks at 3450 and 3730−3600 cm^{-1}, which

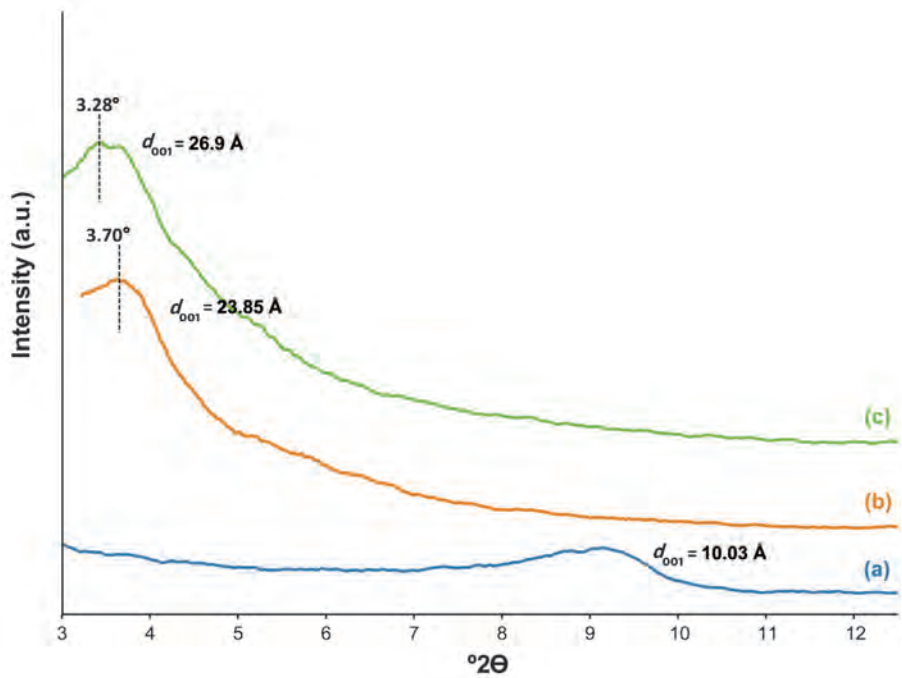

Figure 6. XRD results for: (a) unmodified Mnt; and (b) modified Mnt using method 2 − surfactant addition prior to that of silane; and (c) modified Mnt using method 1 − silane addition prior to that of surfactant.

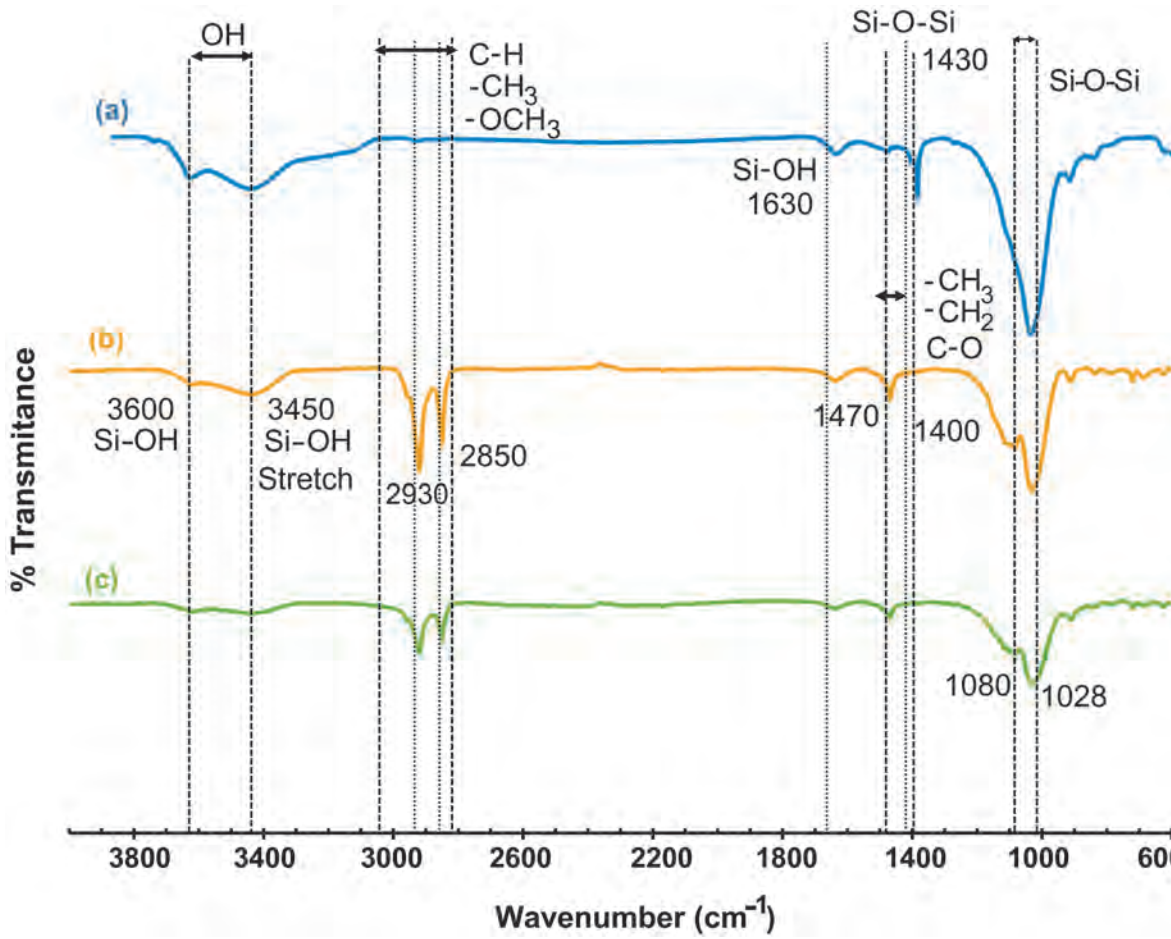

Figure 7. FTIR results for: (a) unmodified Mnt and modified Mnt using silane and surfactant with; (b) method 1 – surfactant addition prior to that of silane; and (c) method 2 – silane addition prior to that of surfactant).

correspond to the stretching vibration of surface Si-OH groups, confirms the reaction of modifiers with the surface of the clay (Hermosin and Cornejo, 1986; El Rassy *et al.*, 2005).

The development and increase in the intensity of the peaks at 2850 and 2930 cm^{-1} indicate O–CH_3 and –CH_2 groups (Hermosin and Cornejo, 1986) or can be assigned to symmetric and antisymmetric CH_2 stretching modes (He *et al*., 2004). Either way, the peaks demonstrate the attachment of the alkyl chain of the organic modifiers to the clay surface.

As mentioned for the results shown in Figure 4, the peaks in the region 1470–1400 cm^{-1} and specifically at 1430 cm^{-1} can be related to alkyl chain of organosilanes and the Si–O–Si bonds for Mnt (Stuart, 2004; Smidt *et al.*, 2011; Pramanik *et al.*, 2013). Generally, the peaks between 1260 and 1000 cm^{-1} correspond to Si–O bonds that can be from silica, silane-silica, or silane-silane sources (Tian *et al.*, 2010). The appearance of the new shoulder at 1080 cm^{-1} in modified Mnt proves the existence of Si–O–Si, however, and further indicates grafting of organosilanes on the Mnt surface (Abbehausen, 2010). The surfactant may have been a factor in creating these Si–O–Si bonds as the shoulder at 1080 cm^{-1} is not visible in Figure 4. Up to this point, the characterization results have indicated strongly that

Table 5. Intercalation of modified and unmodified Mnt/FKM nanocomposites.

Sample	Filler	d_{001} (Å)
18CSI-SF-Mnt/FKM	Octadecyltrimethoxysilane-fluorosurfactant-Mnt	14.47
18CSI-Mnt/FKM	Octadecyltrimethoxysilane-Mnt	14.17
Mnt/FKM	Mnt	11.68

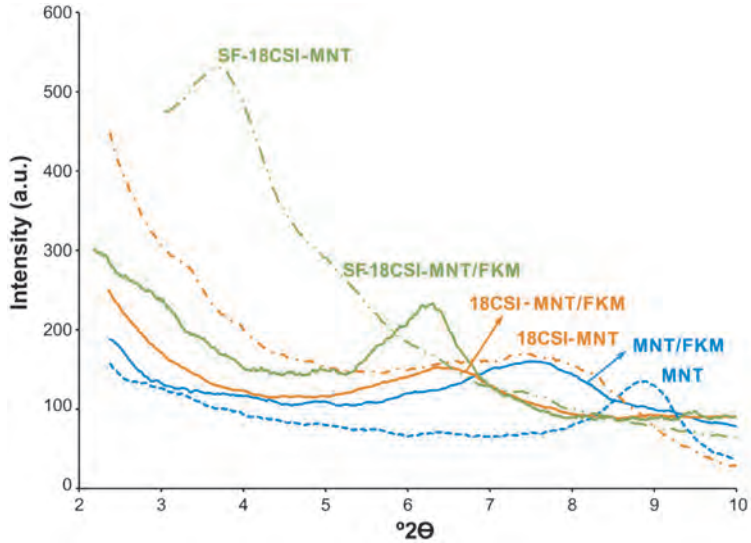

Figure 8. XRD results for unmodified Mnt (dotted line), octadecyltrimethoxysilane-Mnt clay; 18CSI-Mnt (dash-dot line), clay modified with silane and surfactant; SF-18CSI-Mnt (dash-dot-dot line), and the respective nanocomposites with FKM; Mnt/FKM (dash line); 18SCI-Mnt/FKM (solid line); SF-18SCI-Mnt/FKM (double dot and dash line).

Mnt was both modified at the clay edges by alkylsilanes and in the interlayer space by ionic surfactants.

Modified clay/FKM nanocomposites

Dispersion and morphology. The intercalation of FKM in CPN is represented by the interlayer space (d_{001}) of clay layers in the FKM matrix (Table 5, Figure 8). The results demonstrate that larger *d*-spacing values can be obtained for modified clays than for unmodified clay. The treatment of the clay by surfactant, in addition to silane modification, caused slightly more intercalation of clay. When introduced in the polymer matrix, however, the final basal spacing for the nanocomposites was similar for all the clays. This may be a consequence of interaction of clay and polymer during CPN production. The decrease in basal spacing for the 18CSI-SF-Mnt/FKM may be attributed to unbound surfactant in the interlayer spaces of the clays which was extruded by the polymer chains during intercalation.

The effect of these modifications on d_{001} values is more significant for pristine clay, which was not introduced into the polymer matrix. This may be a consequence of the interaction the clay and polymer during CPN production. One possible cause of this phenomenon may have been the excess unbound fluorosurfactant intercalated in the space between the clay layers. These excess unbound molecules cause an increase in the interlayer space of the clay layers while they will be flushed out by polymer molecules during the melt-mixing process. As illustrated in Figure 9, some of the surfactant molecules are bound to the clay and others, in excess, are not. Having great affinity with the fluoroelastomer polymer matrix, these unbound molecules may be flushed out of the interlayer space to the polymer matrix and thus, the basal spacing between the clay layers is reduced.

Through investigation of the morphology of different fillers and FKM nanocomposites, significant improvement in the dispersion of nanoclays into the FKM matrix was obtained by combined silane grafting and surfactant treatment. From TEM images (Figure 10) less agglomeration was observed for the silylated Mnt than the

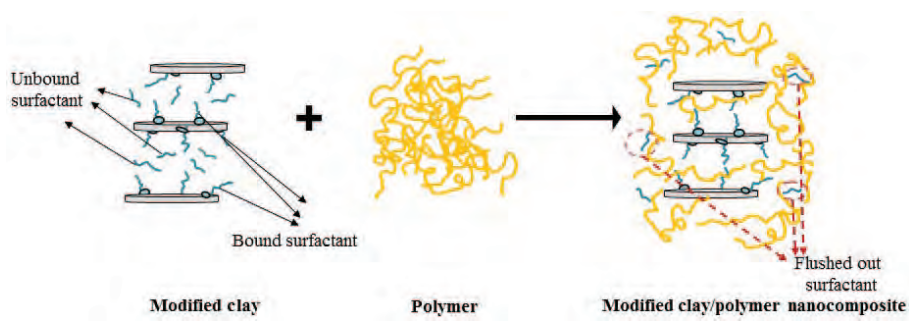

Figure 9. Decrease in *d* spacing during production of nanocomposites.

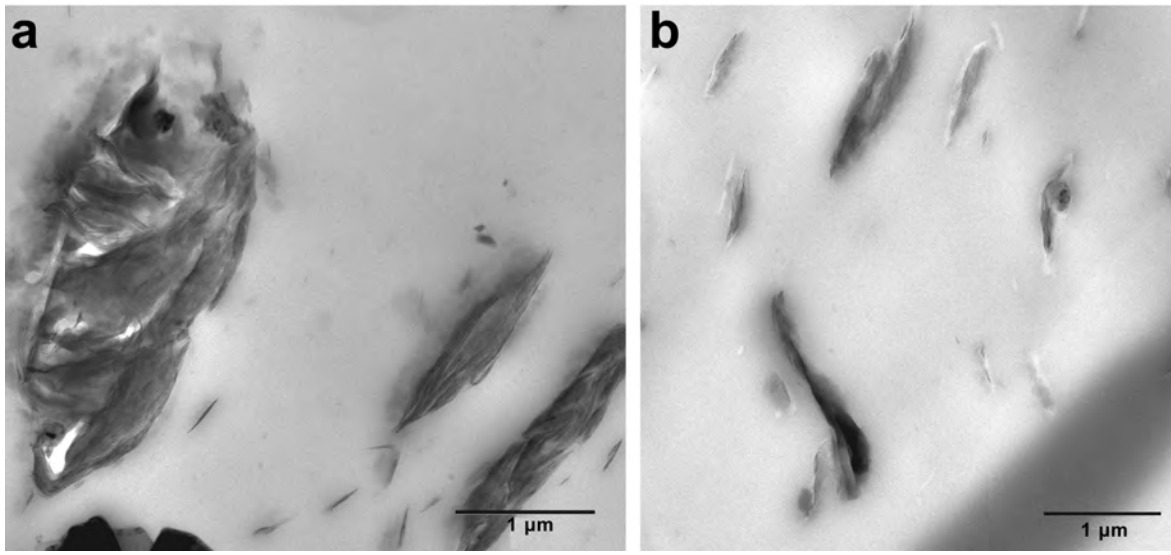

Figure 10. TEM images of: (a) unmodified Mnt/FKM; and (b) organosilane-modified Mnt/FKM.

unmodified one. Consequently, improved distribution and greater intercalation can be achieved by silane modification of nanoclays.

The effects of surfactant on the dispersion of modified clay were also investigated by TEM and SEM imaging. The effect of surfactant modification of nanoclays, as can be observed from TEM images (Figure 11), confirms that the ion exchange in clays by surfactant resulted in enhanced intercalation of clay particles into the CPN.

Better dispersion of the surfactant-silane-modified clays than of the silane-modified clays in the FKM matrix was also observed in SEM images (Figure 12). The better dispersion is due to greater intercalation between the clay layers because of the existence of surfactant molecules in the interlayer space. As a result of enhanced dispersion of fillers, improved mechanical properties (Heinz, 2012) and oil or chemical resistance are expected.

Thermal stability. Another important property of CPN is its thermal resistance to high-temperature applications. The effect of the applied modifications on the thermal stability of the resultant CPN was studied also for this

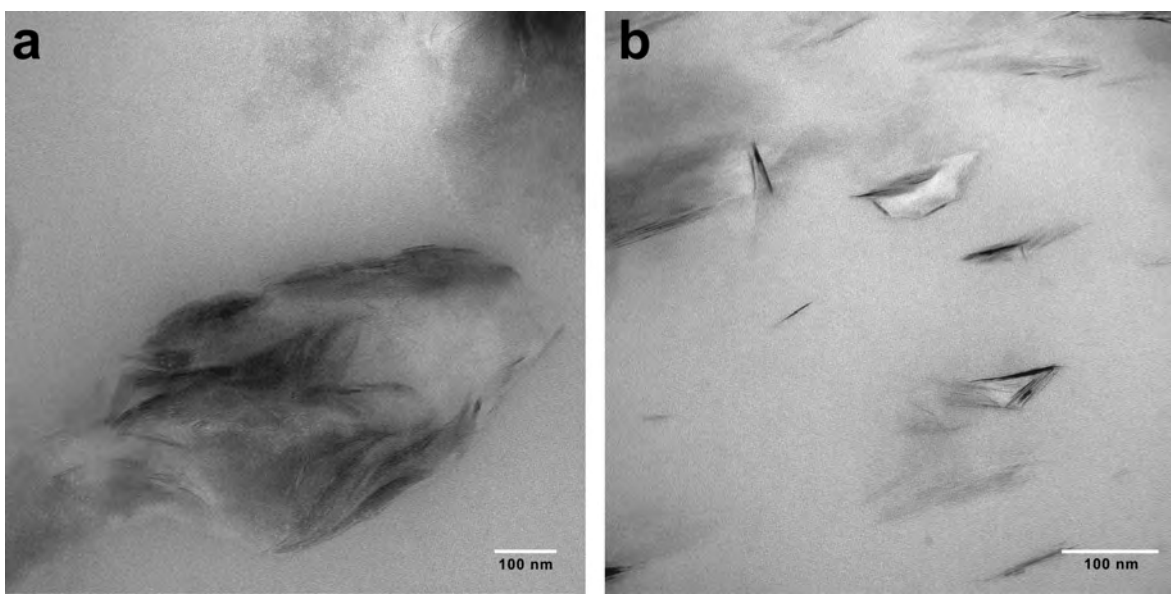

Figure 11. TEM images of: (a) silane-modified Mnt/FKM; and (b) surfactant- and silane-modified Mnt/FKM.

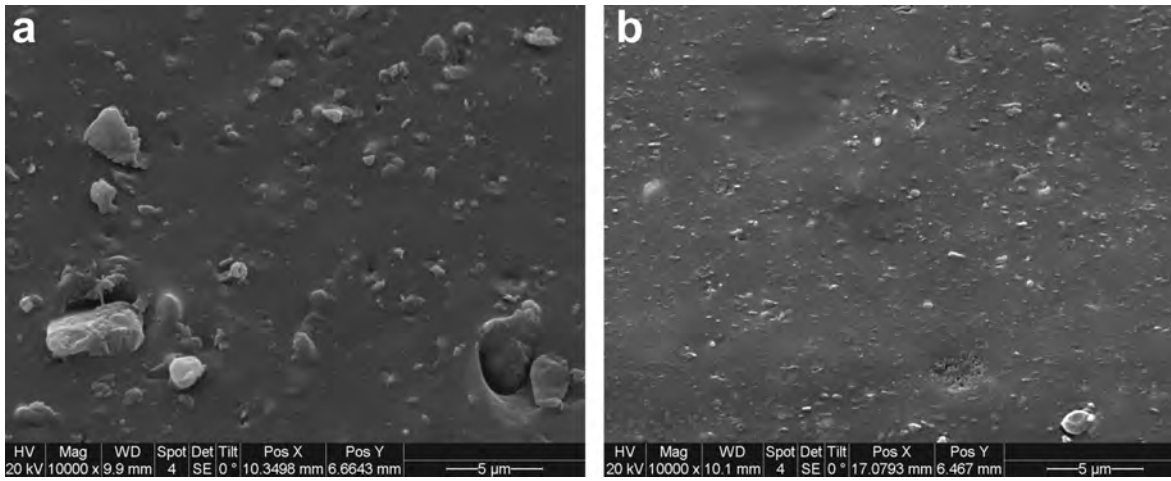

Figure 12. SEM images of: (a) silane-modified Mnt/FKM; and (b) silane- and surfactant-modified Mnt/FKM.

reason. Testing by TGA of the different clay/FKM nanocomposites was carried out (Table 6). Considering a mass loss of 5% as the onset degradation point, silane modification clearly brought about an increase in the thermal stability of the CPN, relative to Cloisite 20A. The use of ammonium ions as a surfactant for clay treatment, however, has a negative effect on the thermal stability of the CPN (Wang *et al.*, 2011). Moreover, the use of carbon black as the second filler caused a decrease in the temperature at which degradation began. The optimum treatment of the clay depends, therefore, on the final application and the favored properties of the elastomer nanocomposite in which the clay is incorporated. Note that for the composites, the data were normalized by dividing the loss by the fraction of polymer (in nanocomposites studied here, the fraction of polymer is 0.909 and of course, for pure FKM, the fraction is 1.0).

CONCLUSIONS

Considering the fact that both chemical compatibility and dispersion of nanoclays in polymer affect the final properties of CPNs, simultaneous modification using organosilane and surfactant has been performed successfully here by two different methods. Montmorillonite with both intercalated fluorosurfactant and silane modification on the edges was produced. This is the first report of using both fluorosurfactant and silane for clay functionalization. By using different saturated and unsaturated silanes on Mnt, the amount of silane grafting and the thermal stability of the clay were both varied depending on the silane chemical structure. The results demonstrated that addition of surfactant and silane could increase noticeably the basal spacing of Mnt from an initial spacing of 10.0 Å up to 26.9 Å, a 169% increase. This is one of the few studies that have investigated silanes of different lengths for the modification of clay surfaces. Silanes with longer alkyl chains were grafted more readily on the clay edges relative to those with shorter alkyl chains. The thermal stability of silane-modified Mnt was greater than that of Cloisite 20A, the latter of which was modified by a tallow surfactant. Further modification of clay, with a fluorosurfactant to increase the spacing between the clay layers, was performed successfully. These materials were also more thermally stable than the Cloisite 20A. A significant increase in the interlayer spaces of the clay was achieved with the ion-exchange reaction as the result of surfactant modification of Mnt; this increase in basal *d* spacing was shown to lead to a better dispersion of clays in the nanocomposites (Bukka and Miller, 1992).

Table 6. 5% mass degradation start point for modified and unmodified Mnt/FKM nanocomposites*.

Clay polymer nanocomposite	Filler	*T* (ºC)
18CSI-Mnt/FKM	Octadecyltrimethoxysilane-Mnt	492
CB-18CSI-Mnt/FKM	Carbon black/octadecyltrimethoxysilane-Mnt	485
18CSI-SF-Mnt/FKM	Octadecyltrimethoxysilane-fluorosurfactant-Mnt	447
Cloisite 20A/FKM	Cloisite 20A	445
FKM	N/A	416

* Temperatures are normalized based on the amount of polymer in the composites.

Enhanced interaction between the modified clay and the FKM, and hence, improved dispersion of the nanoclay in polymer matrix, was achieved. The best intercalation and exfoliation of the clays was obtained by clay modification with surfactant prior to silane grafting.

ACKNOWLEDGMENTS

The authors acknowledge the Natural Sciences and Engineering Research Council of Canada (NSERC) and Weatherford Canada Partnership for funding. They are also grateful to the University of Calgary's Department of Chemical and Petroleum Engineering, Health Sciences Centre, Department of Chemistry, and Department of Geosciences for help with characterization of the samples.

REFERENCES

Abbehausen, C., Formiga, A.L.B., Sabadini, E., and Yoshid, I.V.P. (2010) A β-cyclodextrin/siloxane hybrid polymer: synthesis, characterization and inclusion complexes. *Journal of Brazilian Chemical Society*, **21**, 1867−1876.

Akelah, A. and Moet, A. (1996) Polymer-clay nanocomposites: Free-radical grafting of polystyrene on to organophilic montmorillonite interlayers. *Journal of Materials Science*, **31**, 3589−3596.

Al-haj Ali, M. and Elleithy, R.H. (2011) Viscoelastic properties of polypropylene/organo-clay nano-composites prepared using miniature lab mixing extruder from masterbatch. *Journal of Applied Polymer Science*, **121**, 27−36.

Ameduri, B., Boutevin, B., and Kostov, G. (2001) Fluoroelastomers: synthesis, properties and applications. *Progress in Polymer Science*, **26**, 105−187.

Bergaya, F. and Lagaly, G. (2001) Surface modification of clay minerals. *Applied Clay Science*, **19**, 1−3.

Bergaya, F., Jaber, M., and Lambert, J.F. (2011) Clays and clay minerals. Pp. 1−44 in: *Rubber-Clay Nanocomposites, Science, Technology and Applications* (M. Galimberti, editor). Wiley, Hoboken, New Jersey.

Bergaya, F., Detellier, C., Lambert, J.-F., and Lagaly, G. (2013) Introduction to clay polymer nanocomposites. Pp. 655−678 in: *Handbook of Clay Science*, 2nd edition. Developments in Clay Science, Volume **5**, Elsevier, Amsterdam.

Borse, N.K. and Kamal, M.R. (2006) Melt processing effects on the structure and mechanical properties of PA-6/clay nanocomposites. *Polymer Engineering and Science*, **46**, 1094−1103.

Bukka, K. and Miller, J.D. (1992) FTIR study of deuterated montmorillonites: Structural features relevant to pillared clay stability. *Clays and Clay Minerals*, **40**, 92−102.

Chen, G.X., Choi, J.B., and Yoon, J.S. (2005) The role of functional group on the exfoliation of clay in poly(L-lactide). *Macromolecular Rapid Communication*, **26**, 183−187

Coates, J. (2000) Interpretation of infrared spectra, a practical approach. *Encyclopedia of Analytical Chemistry*, 10815−10837.

Daniel, L.M., Frost, R.L., and Zhu, H.Y. (2008) Edge-modification of Laponite with dimethyl-octylmethoxysilane. *Journal of Colloid Interface Science*, **321**, 302−309.

Das, A., Stöckelhuber, K.W., Jurk, R., Jehnichen, D., and Heinrich, G. (2011) A general approach to rubber–montmorillonite nanocomposites: Intercalation of stearic acid. *Applied Clay Science*, **51**, 117−125.

Dennis, H.R., Hunter, D.L., Chang, D., White, J.L., Cho, J.W., and Paul, D.R. (2001) Effect of melt processing conditions on the extent of exfoliation in organoclay-based nanocomposites. *Polymer*, **42**, 9513−9522.

Dong, J., Ozaki, Y., and Nakashima, K. (1997) Infrared, Raman, and near-infrared spectroscopic evidence for the coexistence of various hydrogen-bond forms in poly(acrylic acid). *Macromolecules*, **30**, 1111−1117.

El Rassy, H. and Pierre, A.C. (2005) NMR and IR spectroscopy of silica aerogels with different hydrophobic characteristics. *Journal of Non-Crystalline Solids*, **351**, 1603−1610.

He, H., Frost, L.R., and Zhu, J. (2004) Infrared study of $HDTMA^+$ intercalated montmorillonite. *Spectrochimica Acta Part A*, **60**, 2853−2859.

He, H., Duchet, J., Galy, J., and Gerard, J.F. (2005) Grafting of swelling clay materials with 3-aminopropyltriethoxysilane. *Journal of Colloid and Interface Science*, **288**, 171−176.

Heinz, H. (2012) Clay minerals for nanocomposites and biotechnology: surface modification, dynamics and responses to stimuli. *Clay Minerals*, **47**, 205−230.

Hermosin, M.C. and Cornejo, J. (1986) Methylation of sepiolite and palygorskite with diazomethane. *Clays and Clay Minerals*, **34**, 591−596.

Herrera, N.N., Letoffe, J.M., Putaux, J.L., David, L., and Bourgeat-Lami, E. (2004) Aqueous dispersions of silane-functionalized Laponite clay platelets. A first step toward the elaboration of water-based polymer/clay nanocomposites. *Langmuir*, **20**, 1564−1571.

Hrachová, J., Komadel, P., and Chodák, I. (2008) Effect of montmorillonite modification on mechanical properties of vulcanized natural rubber composites. *Journal of Materials Science*, **43**, 2012−2017.

Hussain, F., Hojjati, M., Okamoto, M., and Gorga, R.E. (2006) Polymer-matrix nanocomposites, processing, manufacturing, and application: An overview. *Journal of Composite Materials*, **43**, 3107−3123.

Huskic, M., Zigon, M., and Ivanković, M. (2013) Comparison of the properties of clay polymer nanocomposites prepared by montmorillonite modified by silane and by quaternary ammonium salts. *Applied Clay Science*, **85**, 109−115.

Joo, J.H., Shim, J.H., Choi, J.H., Choi, C.H., Kim, D.S., and Yoon, J.S. (2008) Effect of the silane modification of an organoclay on the properties of polypropylene/clay composites. *Journal of Applied Polymer Science*, **109**, 3645−3650.

Lakshminarayanan, S., Lin, B., and Sundararaj, U. (2009) Effect of clay surfactant type and clay content on the rheology and morphology of uncured fluoroelastomer/clay nanocomposites prepared by melt-mixing. *Journal of Applied Polymer Science*, **112**, 3597−3604.

Lambert, J.-F. and Bergaya, F. (2013) Smectite-polymer nanocomposites. Pp. 670−706 in: *Handbook of Clay Science*, 2nd edition. Developments in Clay Science, Volume **5**, Elsevier, Amsterdam.

Marynick, D.S. and Dixon, D.A. (1977) Electron affinity of the methyl radical: Structures of CH_3 and CH_3^-. *Proceedings of the National Academy of Sciences of the United States of America*, **74**, 410−413.

Mingliang, G. and Demin, J. (2008) Influence of organoclay prepared by solid state method on the morphology and properties of polyvinyl chloride/organoclay nanocomposites. *Journal of Elastomers and Plastics*, **40**, 223−235.

Mittal, V., Kim, J.K., and Pal, K. (2011) *Recent Advances in Elastomeric Nanocomposites*. Springer-Verlag, Berlin, Heidelberg.

Modesti, M., Lorenzetti, A., Bon, D., and Besco, S. (2005) Effect of processing conditions on morphology and mechanical properties of compatibilized polypropylene nanocomposite. *Polymer*, **46**, 10237−10245.

Monasterio, F.E. (2010) Effect of the organic groups of difunctional silanes on the preparation of coated clays for olefin polymer modification. *Clay Minerals*, **45**, 489−502.

Morrison, R.T. and Boyd, R.N. (1983) *Organic Chemistry*, 4th edition. New York University, New York.

Norrish, K. (1954) *The Swelling of Montmorillonite.* Division of Soils, C.S.I.R.O., Adelaide, Australia.

Orprecio, R. and Evans, C.H. (2003) Polymer-immobilized cyclodextrin trapping of model organic pollutants in flowing water streams. *Journal of Applied Polymer Science*, **90**, 2103–2110.

Park, M., Shim, I.K., Jung, E.Y., and Choy, J.H. (2004) Modification of external surface of Laponite by silane grafting. *Journal of Physical Chemistry of Solids*, **65**, 499–501.

Paul, D.R. and Robeson, L.M. (2008) Polymer nanotechnology: Nanocomposites. *Polymer*, **49**, 3187–3204.

Pramanik, S., Das, G., and Karak, N. (2013) Facile preparation of polyaniline nanofibers modified bentonite nanohybrid for gas sensor application. *The Royal Society of Chemistry Advances*, **3**, 4574–4581.

Qian, Z., Zhou, H., Xu, X., Ding, Y., Zhang, S., and Yang, M. (2009) Effect of the grafted silane on the dispersion and orientation of clay in polyethylene nanocomposites. *Polymer Composite*, **30**, 1234–1242.

Shanmugharaj, A.M., Rhee, K.Y., and Ryu, S.H. (2006) Influence of dispersing medium on grafting of aminopropyltriethoxysilane in swelling clay materials. *Journal of Colloid and Interface Science*, **298**, 854–859.

Shen, W., He, H., Zhu, J., Yuan, P., and Frost, R.L. (2007) Grafting of montmorillonite with different functional silanes via two different reaction systems. *Journal of Colloid and Interface Science*, **313**, 268–273.

Stuart, B.H. (2004) *Infrared Spectroscopy: Fundamentals and Applications*. Wiley, New Jersey.

Smidt, E., Bhm, K., and Schwanninger, M. (2011) The application of FT-IR spectroscopy in waste management. Pp. 405–430 in: *Fourier Transforms – New Analytical Approaches and FTIR Strategies* (G. Nikolic, editor). InTech, Rijeka, Croatia.

Tian, R., Sitez, O., Li, M., Hu, W., Chabal, Y.J., and Gao, J. (2010) Infrared characterization of interfacial Si-O bond formation on silanized flat SiO_2/Si surfaces. *Langmuir*, **26**, 4563–4566.

Valsecchi, R., Torlaj, L., Turri, S., Tonelli, C., and Levi, M. (2011) Barrier properties in hydrogenated acrylonitrile butadiene rubber compounds containing organoclays and perfluoropolyether additives. *Journal of Applied Polymer Science*, **119**, 3476–3482.

Wang, Y., Wang, X., Duan, Y., Liu, Y., and Du, S. (2011) Modification of montmorillonite with poly(oxypropylene) amine hydrochlorides: Basal spacing, amount intercalated, and thermal stability. *Clays and Clay Minerals*, **59**, 507–517.

Wu, Y.P., Jia, Q.X., Yu, D.S., and Zhang, L.Q. (2004) Modeling Young's modulus of rubber–clay nanocomposites using composite theories. *Polymer Testing*, **23**, 903–909.

Xie, W., Gao, Z., Pan, W.P., Hunter, D., Singh, A., and Vaia, R. (2001) Thermal degradation chemistry of alkyl quaternary ammonium montmorillonite. *Chemistry of Materials*, **13**, 2979–2990.

Xu, X., Ding, Y., Wang, F., Wen, B., Zhang, J., Zhang, S., and Yang, M. (2009) Effects of silane grafting on the morphology and thermal stability of poly(ethylene terephthalate)/clay nanocomposites. *Polymer Composite*, **31**, 825–834.

Zhu, L. and Xanthos, M. (2004) Effects of process conditions and mixing protocols on structure of extruded polypropylene nanocomposites. *Journal of Applied Polymer Science*, **93**, 1891–1899.

Zumdahl, S.S. (1999) *Chemistry*. 5th edition. Houghton Mifflin Harcourt, Boston, Massachusetts, USA.

(*Received 8 July 2014; revised 6 January 2015; Ms. 894; AE: H. He*)

Clays and Clay Minerals, Vol. 63, No. 1, 15–29, 2015.

REVISITING THE INFRARED SPECTRUM OF THE WATER–SMECTITE INTERFACE

ARTUR KULIGIEWICZ[1], ARKADIUSZ DERKOWSKI[1,*], MAREK SZCZERBA[1], VASSILIS GIONIS[2], AND GEORGIOS D. CHRYSSIKOS[2]

[1] Institute of Geological Sciences, Polish Academy of Sciences, ul. Senacka 1, 31-002 Krakow, Poland
[2] Theoretical and Physical Chemistry Institute, National Hellenic Research Foundation, 48 Vassileos Constantinou Av., Athens 11635, Greece

Abstract—An overlap of bands produced by the O–H stretching vibrations of H_2O (O–H_w) and structural OH (O–H_s) in smectite hampers the study by infrared spectroscopy (IR) of both their layer and interlayer structure. The present study re-evaluated the D_2O saturation of smectite as a tool to enable separation of the overlapping bands at ambient conditions. Real-time monitoring by Attenuated Total Reflectance infrared spectroscopy (ATR-IR) was employed during *in situ* sample drying and H_2O or D_2O saturation at ambient temperature. Six dioctahedral and one trioctahedral pure smectites in Ca^{2+}-, Na^{+}-, and Cs^{+}-cationic forms were studied to explore variability in total layer charge, charge location, and interlayer cation. The IR data showed the interlayer O–D_w signature at 2700–2200 cm^{-1} as a proxy for the O–H_w signature in the 3700–3000 cm^{-1} region. In addition to the expected liquid-like bands of D_2O in the interlayer, these O–D_w spectra exhibited an additional sharp stretching feature in the 2695–2680 cm^{-1} range. No significant cation dependence of the sharp band position was observed between pairs of Ca- and Na-smectites for relative humidity (RH) between 60 and 80%, despite the large difference in the ionic potential between these interlayer cations. The intensity of the sharp band was found to be almost insensitive to changes in water content within the range 60–80% RH. The sharp band frequency decreased linearly with increasing total charge of the 2:1 layer (and can be used as a proxy for it), but no effect of charge location could be discerned. In agreement with early studies, this band was attributed to D_2O located on the surface of the interlayer, pointing one O–D group toward the siloxane surface. Based on its high frequency, this band was indicative of free O–D oscillators, with very little or no involvement in hydrogen bonding ("dangling OD"). By analogy to the spectra of D_2O-smectites, the spectrum of H_2O-smectites also involves a sharp O–H_w analog at ~3630 cm^{-1} overlapping with typical OH_s bands (*e.g.* Al_2OH). As a result of this overlap, the sharp 3630 cm^{-1} O–H_w contribution was often missed or attributed solely to O–H_s.

Key Words—Adsorbed Water, ATR, Deuteration, Infrared Spectroscopy, Layer Charge, Smectite.

INTRODUCTION

Analysis of the mid-IR spectra of clay minerals is often hampered by the overlap of bands originating from structural OH groups (OH_s) and OH groups of adsorbed water (OH_w) in the O–H stretching region (3700–3000 cm^{-1}). Unambiguous distinction between the different types of O–H_s and O–H_w stretching modes of clay mineral samples is a crucial prerequisite for their further systematic investigation by IR. This is especially true in the case of dioctahedral smectites. The lack of distinction between O–H_s and O–H_w in the 3640–3610 cm^{-1} range impedes both the study of interlayer H_2O and the identification of individual O–H_s stretching components, and hence, also, the establishment of correlations between O–H_s stretching and the octahedral-sheet composition (*e.g.* Madejová *et al.*, 1994; Fialips *et al.*, 2002; Petit *et al.*, 2002; Zviagina *et al.*, 2004).

Following the seminal work of V.C. Farmer and his group at the Macaulay Institute, Aberdeen, UK, a number of monographs and review papers have dealt in depth with the application of IR to the identification and structural characterization of clay minerals, raising the issue mentioned above (Farmer, 1974; Russell and Fraser, 1994; Petit *et al.*, 1995; Besson and Drits, 1997; Madejová and Komadel, 2001; Madejová, 2003; Gates, 2005). Early IR research was based mostly on thin self-supported clay films measured in transmission using dispersive instruments fitted with suitable environmental cells. More recent studies have benefited from the advent of Fourier transform spectrometers and Attenuated Total Reflectance (ATR) collection optics offering improved spectral quality, convenient non-invasive spectral acquisition, and new possibilities for real-time monitoring (*e.g.* Johnston *et al.*, 1992; Yan *et al.*, 1996; Ras *et al.*, 2007).

Despite the widespread application of IR to clays and clay-based materials, it appears that some of the early pioneering work is fading out without being followed or challenged by modern findings. Early IR work based on substituting interlayer H_2O with D_2O provided evidence that the sharp, high-frequency bands observed at

* E-mail address of corresponding author:
ndderkow@cyfronet.pl
DOI: 10.1346/CCMN.2015.0630102

~3640−3610 cm^{-1} involve a significant contribution from weakly hydrogen-bonded (H-bonded) adsorbed $O-H_w$ (Russell and Farmer, 1964; Farmer and Russell, 1971; Suquet *et al.*, 1977; Sposito and Prost, 1982; Cariati *et al.*, 1981, 1983; Sposito *et al.*, 1983). More recent assignments of the same high-frequency feature in dioctahedral smectites vary. Some authors adopt the aforementioned assignment of an $O-H_w$ stretching mode (*e.g.* Bishop *et al.*, 1994; Madejová *et al.* 1994) and others assign it only to $O-H_s$, and not $O-H_w$ (Bukka *et al.*, 1992; Xu *et al.*, 2000; Madejová and Komadel 2001).

Substitution of interlayer H_2O with D_2O seemed to offer an elegant solution to the problems described above, as D_2O band positions are shifted by a factor of ~1.36 toward lower wavenumbers. The effectiveness of this technique seemed to be confirmed (Farmer and Russell 1971); D_2O saturation can be considered as useful provided that no deuteration of OH_s is assured. Russell *et al.* (1970) studied *in situ* deuteration of structural OH in a number of smectites. Relatively high temperatures and long reaction times (300−400ºC, 1−14 h) were needed for the complete H/D exchange of the structural OH. The progress of OH_s deuteration was manifested by the growing intensity of the structural δ OD bending modes: Al_2OD was observed at 700−690 cm^{-1}, AlFe(III)OD at ~675 cm^{-1}, and AlMgOD at ~650 cm^{-1} (compared to the corresponding δ OH modes at ~915, 880, and 840 cm^{-1}, respectively). The appearance of these bands in spectra of smectites after saturation with D_2O can be treated as an indicator of OH_s deuteration. Some effects interpreted as partial deuteration of OH_s were, however, observed at lower temperatures (98ºC, Bukka *et al.*, 1992).

The aim of the present study was to re-evaluate D_2O saturation as a convenient spectrochemical tool for the separation of the $O-H_s$ and $O-H_w$ ($O-D_w$) stretching modes of smectite at ambient hydration conditions. Seven smectite samples in three cation-exchanged forms were selected to represent most of the variability found in nature. The spectrum of water (as D_2O) was obtained free from the interference of structural OH groups and analyzed in terms of layer charge, charge location, and exchangeable cation.

EXPERIMENTAL

Materials

The present study was based on six natural dioctahedral smectites from the collection of the Source Clays Repository of The Clay Minerals Society and one synthetic saponite (Table 1). SCa-3 and SAz-2 are high-charge montmorillonites with almost no tetrahedral charge. SWy-2 (Wyoming) is a low-charge beidellitic montmorillonite. SWa-1 is a low-charge Fe-rich smectite/nontronite with almost equal amounts of tetrahedral and octahedral charge. SbCa-1 and SbId-1 are beidellites with high and low charges, respectively. The synthetic saponite (SAP) is a high-charge member of the trioctahedral series reported by Pelletier *et al.* (2003).

All dioctahedral smectite samples were purified by removing carbonates, organics, and Fe-oxides/hydroxides (except SWa-1) by a sequence of acetic acetate buffer, peroxide, and buffered sodium dithionite treatments (Jackson, 1969). Subsequently, particle-size fractions were separated by centrifugation and dialyzed in deionized water. All fine fractions were found to be mineralogically pure, with the exception of SbId-1 which contained a kaolinite admixture, clearly evident in the IR spectra. Homoionic forms of each smectite were prepared by five washings with appropriate 0.5 M Ca^{2+}, Na^+, and Cs^+ chloride solutions of reagent-grade purity and dialysis in deionized water.

The literature on smectite samples from the Source Clays Repository reports various size fractions with different mineral formulae and layer-charge density (*e.g.* Zviagina *et al.*, 2004; Gates, 2005). Moreover, the determination of the total exchangeable cations as a way to measure layer-charge density is method-dependent (Wolters *et al.*, 2009) and literature values may not be comparable to each other unless determined by the same method. For these reasons, the total layer charge per half unit cell (Q_{tot}) of the actual particle fractions used in the study was determined independently (Table 1). This charge determination was based on the measurement of the Na content in the Na-exchanged samples subjected to conventional acid digestion, using a flame photometer (Sherwood 420 by Sherwood Scientific Ltd., Cambridge, UK) calibrated against NIST standards 76a and 70a.

Table 1. Smectites used in the study.

Sample	Layer type	Charge location	Particle size fraction	Total layer charge Q_{tot}
SCa-3	montmorillonite	octahedral	<1.0 μm	0.51(1)
SAz-2	montmorillonite	octahedral	<2.0 μm	0.52(1)
SWy-2	montmorillonite	octahedral/tetrahedral	<0.1 μm	0.36(1)
SWa-1	nontronite	tetrahedral/octahedral	<1 μm	0.31(1)
SbCa-1	beidellite	tetrahedral	<1.0 μm	0.50(1)
SbId-1	beidellite	tetrahedral	<0.1 μm	0.39(1)
Saponite	saponite, trioctahedral	tetrahedral	<2 μm	0.58(1)

Estimates of the molecular weights for each smectite were based on literature compositions.

ATR-IR experiments

Infrared spectra (4000−580 cm^{-1}) were collected on two Fourier transform instruments (Equinox 55 by Bruker Optics and Nicolet 6700 by Thermo Scientific) equipped with single-reflection diamond ATR accessories (DuraSampl IR II by SensIR Technologies and high-temperature Golden Gate by Thermo Scientific, respectively). The spectra were measured as 100-scan averages with 4 cm^{-1} resolution ($\Delta\nu$ = 2 cm^{-1} by interferogram zerofill) and reported after correction for the dependence of the penetration depth on wavelength. Second derivatives were calculated with Savitzky-Golay routines.

Spectra were measured from ~5−10 μm-thick films. The films were made by careful depositing and drying of a few drops of an aqueous sonicated suspension of smectite on the top of the ATR crystal, avoiding air bubbles or voids that could reduce contact between the thin film and the ATR crystal surface. The ATR plate was fitted with a home-made purging cap which enabled IR monitoring during purge drying or vapor hydration at ambient temperature (25±1ºC). The as-prepared smectite films were subjected to one of the following treatments:

(a) Equilibration under a N_2 flow with adjustable relative humidity (RH = 19−90±2%) of H_2O or D_2O vapor, which was produced by a humidity generator (HG-100 by L&C Science and Technology, Hialeah, Florida, USA). At each stepwise stabilized RH value, two spectra were collected after ~5 and ~10 min to ensure sample equilibration with the vapor.

(b) Alternating D_2O/HDO/H_2O wetting and N_2 purge-drying cycles as in Bukas *et al*. (2013). During each cycle, equilibration for at least 15 min was performed in order to achieve complete substitution.

N_2 of purity 5.0 and D_2O with 99.9%$_{at}$, D/H (Sigma-Aldrich) were used in both cases. A systematic study of hydration/dehydration kinetics (*cf.* Fu *et al.*, 1990) was not performed and the quantitative determination of H_2O/D_2O in the smectite samples is beyond the scope of this paper.

RESULTS AND DISCUSSION

Smectites saturated with H_2O at different RH conditions

The dependence of the ATR-IR spectra of Ca- and Na-SWy-2 exposed to variable RH (19−90% at 25ºC, Figure 1) is typical for montmorillonite and analogous trends have been reported in numerous previous publications (*e.g.* Xu *et al.*, 2000; Madejová *et al.*, 2002; Madejová, 2003 and references therein). Briefly, IR activity is observed in three frequency ranges: ~3700−3000 cm^{-1} (ν O−H_s, O−H_w), 1650−1600 cm^{-1} (δ H_2O), and ~1200−800 cm^{-1} (dominated by various strong Si−O modes). The bending modes of the structural OH groups (δ OH_s) are superimposed on the low-frequency side of the strong Si−O envelope and are diagnostic of the octahedral layer substitutions. In the spectrum of SWy-2 these bending modes are observed at ~915, 881, and 843 cm^{-1} and attributed to Al_2OH, AlFe(III)OH, and AlMgOH pairs, respectively (*e.g.* Madejová *et al.*, 2002; Madejová, 2003; Gates, 2005 and references therein). In contrast to the bending modes, the corresponding O−H_s stretching component bands of the three dioctahedral species are not easily resolved (Zviagina *et al.*, 2004 and references therein). These OH_s bands contribute collectively to the band at 3625 cm^{-1} (Figure 1), which appears to be rather insensitive to both the hydration state and the interlayer cation.

The effect of progressively decreasing RH on the spectrum of montmorillonite is largely manifested by the decrease in intensity and slight shift to higher frequencies of the broad peaks at ~3400 cm^{-1}. The exact position of this peak is cation dependent (3392 cm^{-1} in Ca-SWy-2 and 3405 cm^{-1} in Na-SWy-2, Figure 1). A less pronounced decrease in intensity of the band at ~1630 cm^{-1} and a concomitant shift to lower frequencies upon drying are observed, in agreement with previous literature (Johnston *et al.*, 1992; Madejová *et al.*, 2002; Madejová, 2003; Gates, 2005). Clearly, the features at ~3400 and ~1630 cm^{-1} ought to be attributed to H_2O on the basis of their response to drying and their dependence on the interlayer cation. A weak shoulder at ~3215 cm^{-1} is also ubiquitous in the spectra of smectites (Figure 1). An early assignment of this feature to the overtone of the H_2O bending (~1630 cm^{-1}) by Farmer (1974) has been adopted in the recent literature. Perhaps a more appropriate description would consider the ~3400 and 3215 cm^{-1} bands of H_2O as resulting from the Fermi resonance between the stretching fundamental and the bending overtone of H_2O (Efimov and Naberukhin, 2002; Sovago *et al.*, 2009). Some smectites are reported to exhibit an additional poorly resolved band at 3580−3540 cm^{-1}, also attributed to O−H_w stretching (Bishop *et al.*, 1994; Xu *et al.*, 2000; Madejová *et al.*, 2002) and not to O−H_s (*e.g.* Zviagina *et al.*, 2004). All typical H_2O-related features and trends upon drying were observed for all smectites in this study. Comparing the Ca- and Na-forms of the SCa-3 montmorillonite and the SbCa-1 beidellite (Figure 2) with those of SWy-2 (Figure 1) indicated that each smectite responds to changing %RH by adjusting the intensity of the broad band at ~3400 cm^{-1}, whereas the high-frequency sharp O−H stretching component is relatively unaffected. The position of the ~3400 cm^{-1} band appeared to depend more on the type of interlayer cation and less on the type of 2:1 layer. The ~3400 cm^{-1} band shifted to higher frequencies upon drying and this effect was more pronounced in the Na- than in the Ca-smectites (Figure 3a). This is mostly because, for any given value of %RH, the H_2O content of smectites is strongly dependent on the nature of the interlayer cation.

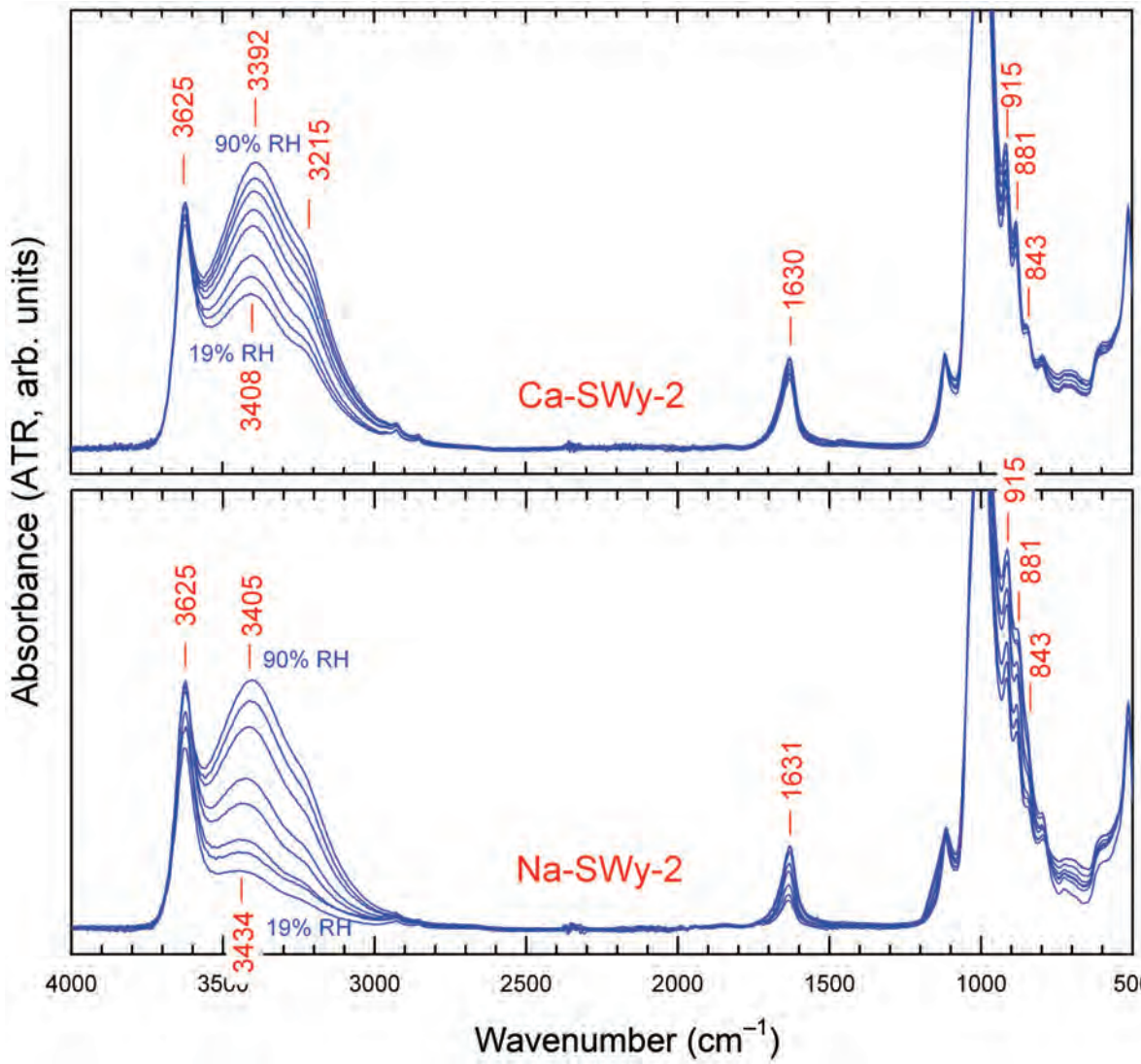

Figure 1. ATR-IR spectra of Ca- (upper) and Na-SWy-2 montmorillonite (lower) as a function of relative humidity (19−90%) at 25ºC.

According to Chiou and Rutherford (1997), Ca-SWy-1 equilibrated at 90% RH has ~250 mg of H_2O/g clay whereas the corresponding content in Na-SWy-1 is ~190 mg H_2O/g. Similarly, at 19% RH the H_2O contents are ~90 mg of H_2O/g in Ca-SWy-1 and 15 mg of H_2O/g in Na-SWy-1 corresponding to 10.4 and 0.9 H_2O molecules per exchangeable cation, respectively. These trends in H_2O content *vs.* %RH were in qualitative agreement not only with the varying intensity of the 3500−3000 cm^{-1} envelope (Figures 1 and 2) but also with its varying position (Figure 3b), in agreement with Xu *et al.* (2000) and Madejová *et al.* (2002). In contrast, changes in the water content appeared not to affect the position, intensity, and shape of the ~3625 cm^{-1} band, which was least sensitive to the interlayer cation type and hydration stage in the range of water content studied (Figures 1 and 2). As shown by Madejová *et al.* (1994) and Zviagina *et al.* (2004), the exact position (3633 cm^{-1} in SbCa-1, 3625 cm^{-1} in SWy-2, and 3616 cm^{-1} in SCa-3 in both the Ca- and Na-series) and the shape of the ~3625 cm^{-1} band in the three smectites are related to their different octahedral-sheet compositions.

Based on the information above, the response of the smectite IR spectra to varying hydration appears to be consistent with the assignments of the ~3625 cm^{-1} and ~3400 cm^{-1} bands to O−H_s (structural) and O−H_w (water), respectively, in agreement with many recent studies (Xu *et al.*, 2000; Madejová and Komadel, 2001; Madejová *et al.*, 2002; Madejová, 2003). Does this simple interpretation withstand a D_2O saturation test? D_2O saturation is expected to move the entire set of H_2O bands to lower frequencies, replacing the δ H_2O at ~1630 cm^{-1}, its overtone at ~3215 cm^{-1}, and the

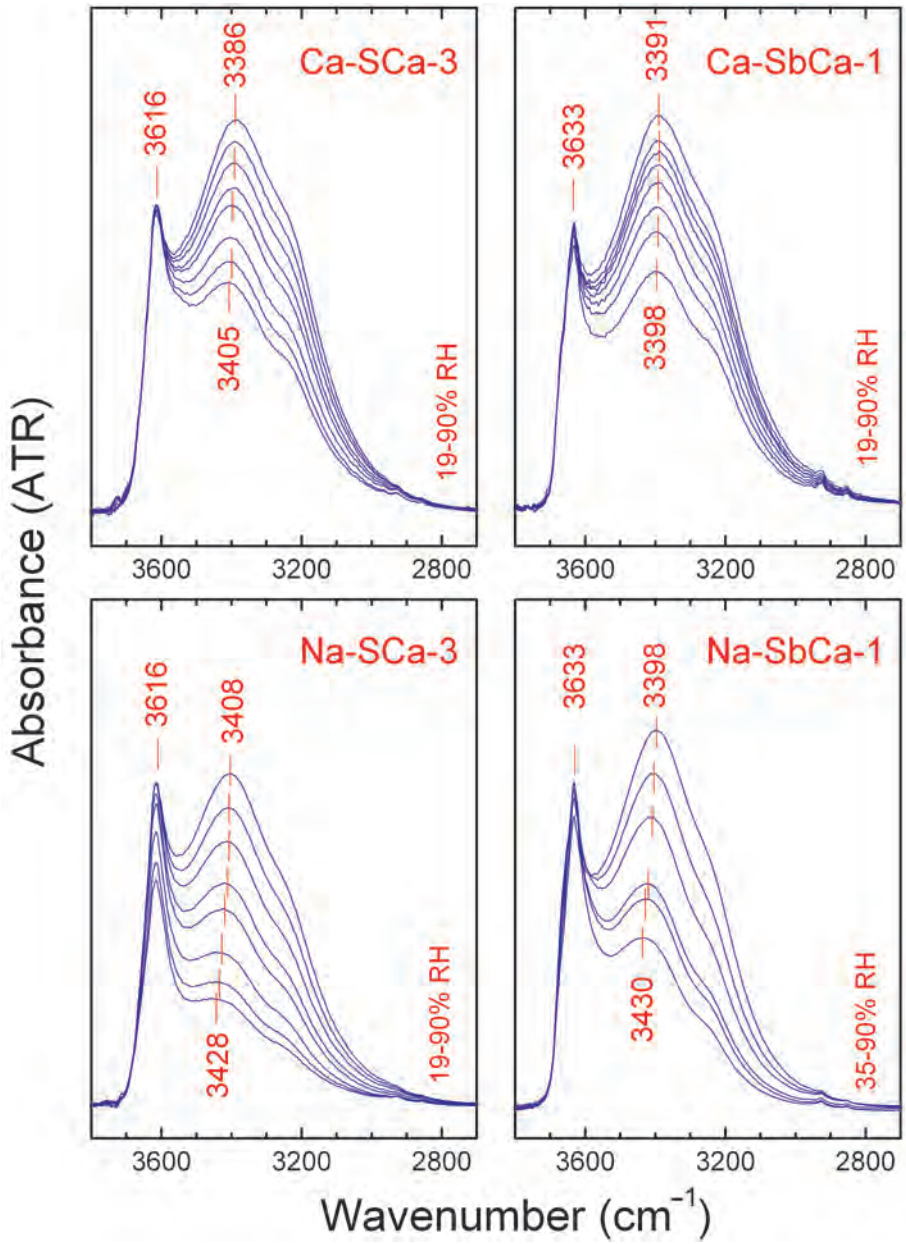

Figure 2. Details of the ATR-IR spectra of Ca- and NaSCa-3 montmorillonite and high-charge beidellite (SbCa-1) as a function of relative humidity at 25ºC.

ν O–H_w at ~3400 cm^{-1} with their corresponding D_2O bands at ~1200, ~2370, and ~2500 cm^{-1}, respectively (ν (H/D) ≈ 1.36). If the three aforementioned H_2O bands are the only ones that originate from water adsorbed on the smectite surface, no new bands other than their D_2O analogs should be observed upon D_2O saturation.

D_2O- vs. H_2O-saturated samples

Cycling D_2O vapors and dry N_2 at ambient conditions over oriented smectite film resulted in an almost complete saturation with D_2O, as indicated by the comparison of the ATR-IR spectra of the H_2O- and D_2O-forms of Na-SWy-2 (Figure 4), collected at ~50% RH (*cf.* Figure 3). The 1200–800 cm^{-1} range of a smectite spectrum undergoes systematic changes in peak positions and intensities upon varying %RH (in agreement with Yan *et al.*, 1996), regardless of whether the sample is saturated with D_2O or H_2O. Appropriate comparison of data collected during different experiments (*e.g.* Figure 4) required, therefore, that the spectra be matched based on the same or very similar hydration states.

Saturation with D_2O resulted in a significant decrease in absorbance at 3800–3000 cm^{-1} (due to O–H_w stretching)

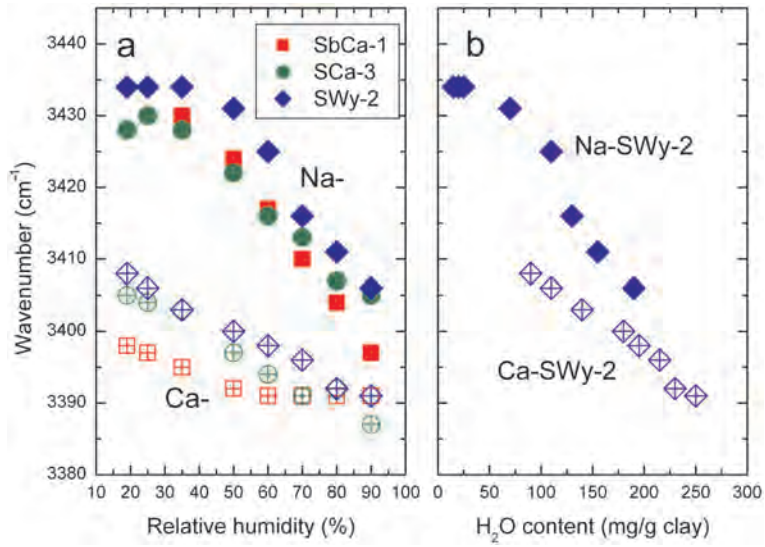

Figure 3. (a) Dependence of the position of the H_2O stretching mode at ~3400 cm^{-1} on relative humidity for the clays shown in Figures 1 and 2. (b) The same frequency data for SWy-2 plotted *vs.* the corresponding H_2O contents of Chiou and Rutherford (1997).

and the appearance of a new complex band envelope of O–D stretching at 2800–2200 cm^{-1}. A sharp, asymmetric O–H band peaking at 3624 cm^{-1} persisted during D_2O saturation at ambient conditions. A spectral difference profile between D_2O- and H_2O-saturated forms of Na-SWy-2 (Figure 4) is close in shape to the O–D profile, but the positions of bands are shifted by ν (H/D) = 1.36. Furthermore, the bending mode of D_2O was observed at ~1205 cm^{-1}, no H_2O bending was observed at ~1630 cm^{-1}, and the very low-intensity band at ~1450 cm^{-1} indicated that there was no significant contribution from HDO molecules. The 2δ D_2O Fermi-resonant overtone was also noticeable at 2374 cm^{-1}, as anticipated.

The as-produced O–D stretching profile of D_2O-saturated Na-SWy-2 exhibited the expected broad features of liquid D_2O peaking at ~2500 cm^{-1} (Bertie *et al.*, 1989), but involved an additional sharp feature observed at 2686 cm^{-1} in the absorbance mode, which was better resolved at 2692 cm^{-1} in the 2nd derivative mode (Figure 4). The corresponding O–H position was 3638 cm^{-1} (H/D = 1.35), as determined from the 2nd derivative of the H_2O–D_2O difference spectrum.

The origin of the sharp 2692 (3638) cm^{-1} O–D (O–H) band needs to be clarified. A close inspection of both absorbance and the 2nd derivative spectra of H_2O- and D_2O-wet Na-SWy-2 (Figure 4) indicated that the intensity of the δ OH bands (at 913, 878, and 841 cm^{-1}, respectively) did not decrease upon D_2O wetting and no features attributable to δ OD_s were observed. Hence, the D_2O saturation under the conditions employed did not produce OD_s detectable by IR. As a consequence, the sharp 2692 (3638) cm^{-1} band ought to be associated with OD_w (OH_w). The presence of this sharp high-frequency D_2O band, which is absent from the spectra of liquid D_2O (Max and Chapados, 2009), is ubiquitous in the spectra of all smectites and in all cationic forms investigated here. Several representative examples (Figure 5) demonstrate that the 3800–2800 cm^{-1} spectral difference between the H_2O- and D_2O-saturated samples matches in all cases the 2800–2100 cm^{-1} O–D stretching envelope of D_2O. In most H_2O-wet samples, the frequency range between 3650 and 3615 cm^{-1} involves unresolved contributions from both O–H_w and O–H_s. Exceptions are saponite and nontronite which exhibit O–H_s modes at higher and lower frequencies, respectively (Mg_3OH: ~3683 cm^{-1}, $Fe(III)_2OH$: ~3560 cm^{-1}). Incidentally, the fact that D_2O-wet saponite and nontronite both exhibit a high-frequency D_2O stretching peak differing by <30 cm^{-1} (Figure 5) whereas their structural OH_s peaks are >120 cm^{-1} apart adds further support to the assignment of the high-frequency O–D stretching to O–D_w and not to O–D_s.

Further evidence supporting the assignment of the sharp 2692 (3638) cm^{-1} band to O–D_w (O–H_w) comes from the near-IR spectra of smectites, which allow for the full separation of OH_w from OH_s by means of the (ν+δ) stretching-bending combination modes, due to large separation between the combination modes of smectite structure (ν O–H_s ~3620 cm^{-1}, δ OH_s ~916 m^{-1} and below that results in (ν+δ) at ~4536 cm^{-1}) and water (ν O–H_w ⩾3610 m^{-1}, δ H_2O at ~1635 m^{-1} which results in (ν+δ) at ~5250 cm^{-1}) (Bishop *et al.*, 1994; Cariati *et al.*, 1981). Montmorillonite clays exhibit a sharp H_2O (ν+δ) combination mode at ~5250 cm^{-1} (Clark *et al.*, 1990; Bishop *et al.*, 1994). As the position of δ (H_2O) is always at ~1630 cm^{-1}, analogous to δ (D_2O) at ~1205 cm^{-1} (Table 2), the (ν+δ) combination band cannot possibly involve the stretching at ~3420 cm^{-1} and requires the presence of a ν (O–H_w) mode with a position greater than 3610 cm^{-1} (Cariati *et al.*, 1981).

Based on the above, the sharp band at 2680–2694 cm^{-1}, which is observed in all D_2O-wet

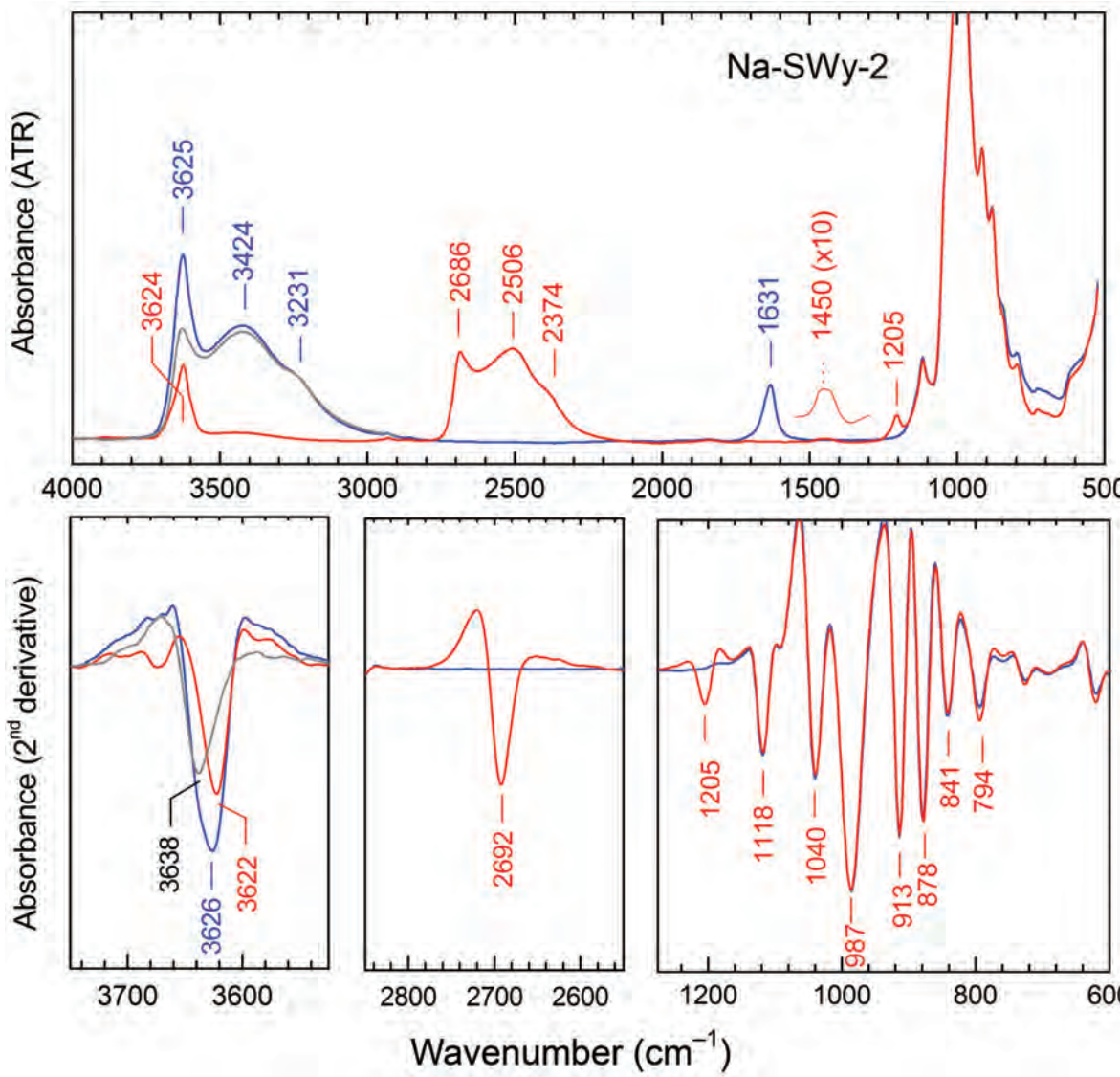

Figure 4. (Upper) Comparison of the ATR-IR spectra of Na-SWy-2 montmorillonite equilibrated by H_2O (blue) and D_2O (red) at ~50% relative humidity, 25ºC. Their difference spectrum in the 4000−2800 cm^{-1} range is included (gray). The very weak absorbance intensity at ~1450 cm^{-1} indicates that only trace HDO is present in the D_2O sample. (Lower) Details of the 2nd derivative ATR-IR and difference spectra over selected wavenumber ranges.

Table 2. Positions (cm^{-1}) of the high-energy O−D stretching component, ν (O−D), and bending δ (D_2O) bands for D_2O-saturated samples at ambient conditions and in different cationic forms. Band positions were determined from the minima of 2nd derivatives with 13-point Savitzky Golay smoothing.

Sample name	ν (O−D)			δ (D_2O)		
	Ca	Na	Cs	Ca	Na	Cs
SWa-1	2692.1(5)	2692.8(5)	2691.4(1)	1202.3(5)	1202.6(5)	1203.8(5)
SWy-2	2691.7(5)	2692.1(5)	2693.2(5)	1201.9(5)	1203.6(5)	1207.1(5)
SbId-1	2689.3(5)	2689.4(5)	2691.6(5)	1203.8(5)	1205.0(5)	1207.6(5)
SbCa-1	2685.5(5)	2684.5(5)	n.a.	1204.9(5)	1207.4(5)	n.a.
SCa-3	2686.2(5)	2685.5(5)	2689.4(5)	1202.4(5)	1204.9(5)	1206.5(5)
SAz-2	2686.0(5)	2686.1(5)	2690.0(5)	1202.4(5)	1204.9(5)	1206.2(5)
SAP	2684(2)	2682(2)	2687(2)	1204.4(5)	1205.5(5)	1205.0(5)

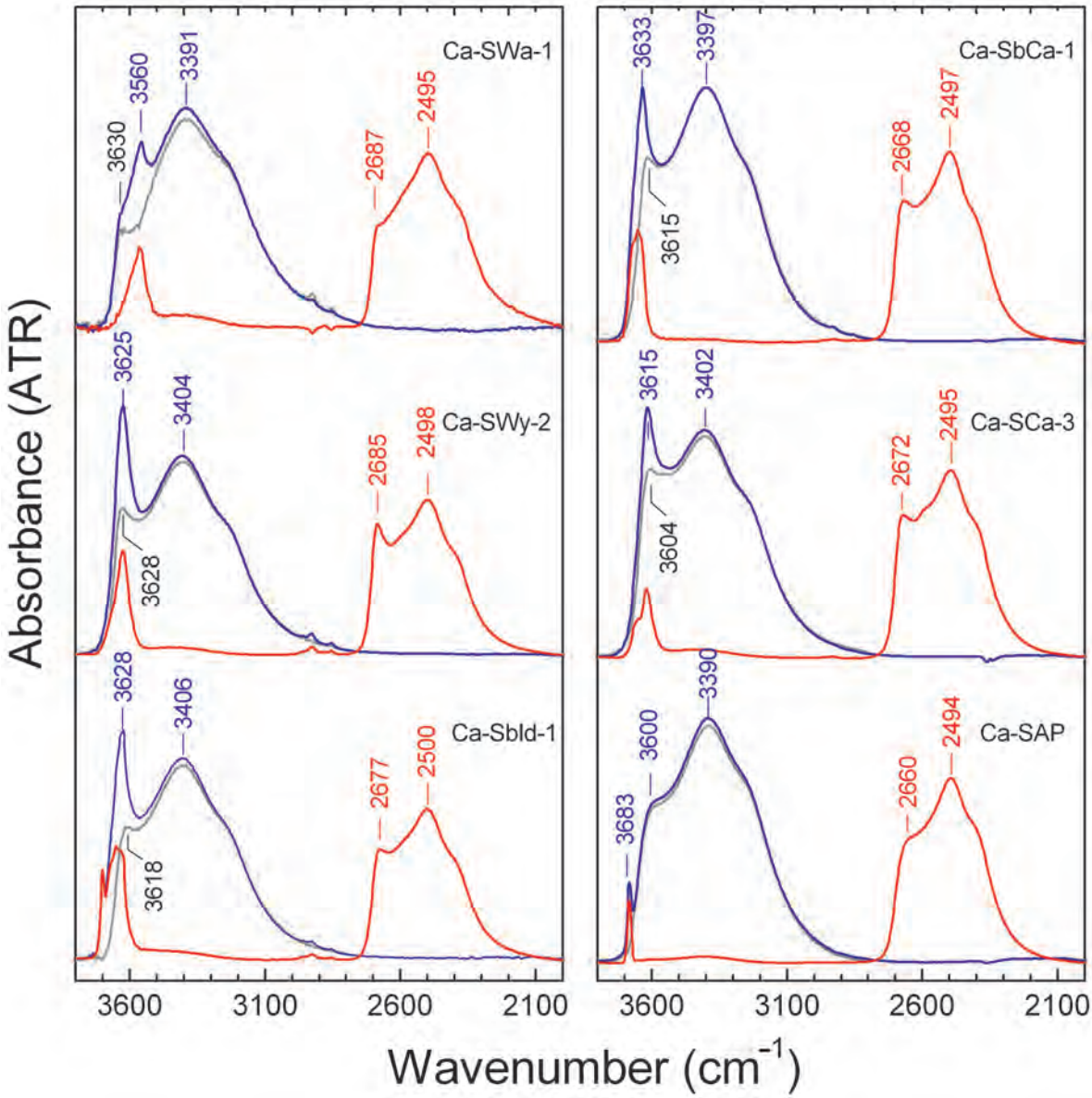

Figure 5. Absorbance spectra of smectites equilibrated with ~50% RH of H_2O (blue) or D_2O-vapor (red) and their difference in the O−H stretching range (gray). The spectra of the SAz-2 montmorillonite (SAz-2, not shown) are nearly identical to those of the SCa-3 sample. All samples are in Ca-form.

smectites, must be produced by a D_2O stretching mode and not by deuterated structural hydroxyls. In H_2O-wet samples, this band has an analog at 3638 cm^{-1} which cannot be resolved easily from the stretching modes of the structural hydroxyl groups (O−H_s) peaking at ~3622 cm^{-1} (Figure 4).

Smectites saturated with D_2O at different RH conditions

In the O−D stretching region, the intensity of a band at ~2500 cm^{-1} increased with increasing %RH, as shown for a representative sample SWy-2 (Figure 6), irrespective of interlayer cation type. This trend is similar to the evolution of the OH_w stretching envelope (*cf.* Figures 1 and 6). The sharp band at ~2686 cm^{-1} is always present in the spectra, irrespective of %RH, with a relatively uniform intensity for the Ca-form, except at the lowest %RH values. The number of D_2O molecules responsible for the sharp band must thus remain relatively constant throughout the experiment, whereas the number of molecules in the non-interface position in the interlayer (cation-bound, bulk water) decreases with decreasing RH, causing a significant intensity decrease below 2600 cm^{-1} (*cf.* Johnston *et al.*, 1992; Xu *et al.*, 2000). The same trend is visible for Na-SWy-2 although changes in the position and intensity of the sharp band are more pronounced and start at higher RH (Figure 6).

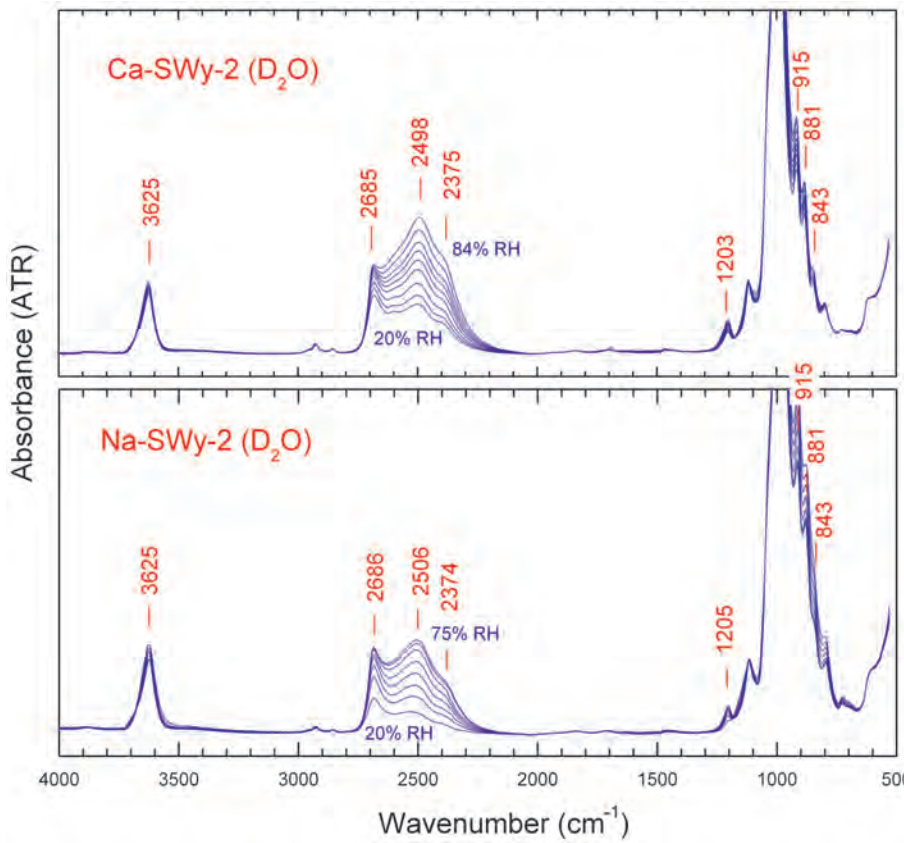

Figure 6. ATR-IR spectra of D_2O-exchanged, Ca- (upper) and Na-SWy-2 montmorillonite (lower) equilibrated at variable D_2O relative humidity at 25ºC.

The lack of structural O–D_s bending bands at frequencies observed by Russell *et al.* (1970) proves that, within the detection limits of ATR-IR, no deuteration of structural OH groups occurred.

Changes of the sharp band position as a function of changing RH were traced with a 2nd derivative approach for samples SWy-2 and SCa-3 in Na- and Ca-forms (Figure 7). The sharp band is at higher frequency for SWy-2 in both cationic forms than for the SCa-3 sample and is relatively constant for RH between 60 and 80%. At lower RH, the frequency of the sharp band decreases. The band position for the SCa-3 sample stays relatively constant across a broad range of RH for both interlayer cations (Figure 7). The largest difference in the sharp band position between the samples is observed for RH between 60 and 80%. In all samples studied the sharp band position is very stable within that range of RH. The RH range between 60 and 80% was, therefore, chosen to

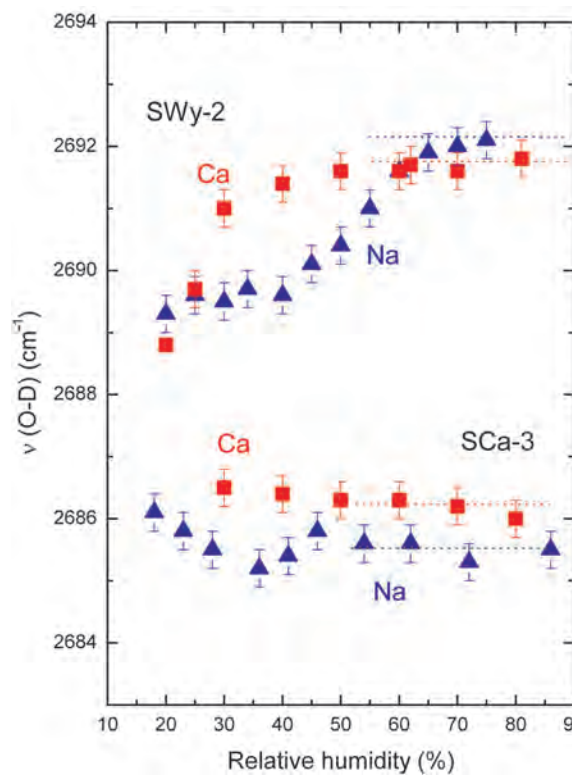

Figure 7. Positions (cm^{-1}) of the high-frequency O–D stretching component, ν (O–D), of D_2O-saturated SWy-2 and SCa-3 montmorillonite in Ca- and Na-forms as a function of D_2O relative humidity at 25ºC. Values are taken from the minima of the 2nd derivatives with 13-point Savitzky Golay smoothing. Dashed lines indicate average values included in Table 1.

record the sharp band positions for the remaining samples, despite greater overlap with a broad O–D stretching band at ~2500 cm^{-1}.

Systematics of the high-frequency D_2O stretching band in smectites

A 2nd derivative with 13-point Savitzky-Golay filter, corresponding to a window of ±12 cm^{-1} around the central point, was employed to find the peak position of the sharp band for each smectite analyzed (Table 2). This smoothing filter was chosen to provide the maximum contrast between the sharp 2700–2670 cm^{-1} O–D stretching band and the broader 2500– and 2400 cm^{-1} component band. The 2nd derivative minima of the O–D bands were consistently found at higher energy than the apparent maxima of the corresponding absorbance spectra (*e.g.* Figure 4), which can be explained by the presence of additional poorly resolved components in the 2700–2500 cm^{-1} range that results in the shifting of the apparent absorbance maxima towards slightly lower frequency.

A linear decrease of frequency was observed upon increasing the total layer charge of the smectite (Table 2 and Figure 8). No effects of octahedral layer type (dioctahedral or trioctahedral) or charge location (tetrahedral or octahedral) on peak position were observed. In addition, little or no difference between the Ca-saturated and Na-saturated smectite series was noted. The fitted lines for Ca- and Na-saturated smectites (Figure 8) were identical within error and could be approximated by a single equation:

$$\nu\ (O–D) = 2703.9 - 35.8Q_{tot},\ (R^2 = 0.94,\ n = 14) \quad (1)$$

The Cs-saturated series showed a much weaker dependence on Q_{tot}:

$$\nu\ (O–D) = 2698 - 17Q_{tot},\ (R^2 = 0.76,\ n = 6) \quad (2)$$

HDO-saturated smectites

The stretching envelope of H_2O and D_2O is complicated by the intramolecular coupling between the two O–H or two O–D bonds. In an attempt to reduce this intramolecular coupling, some earlier studies (*e.g.* Farmer and Russell, 1971; Suquet *et al.*, 1977) reported the spectra of HDO instead of D_2O in smectites. Briefly, this type of isotopic enrichment involves wetting the samples with a mixture of D_2O:H_2O, typically 20:80 by volume (~36% HDO, 60% H_2O, and 4% D_2O), and

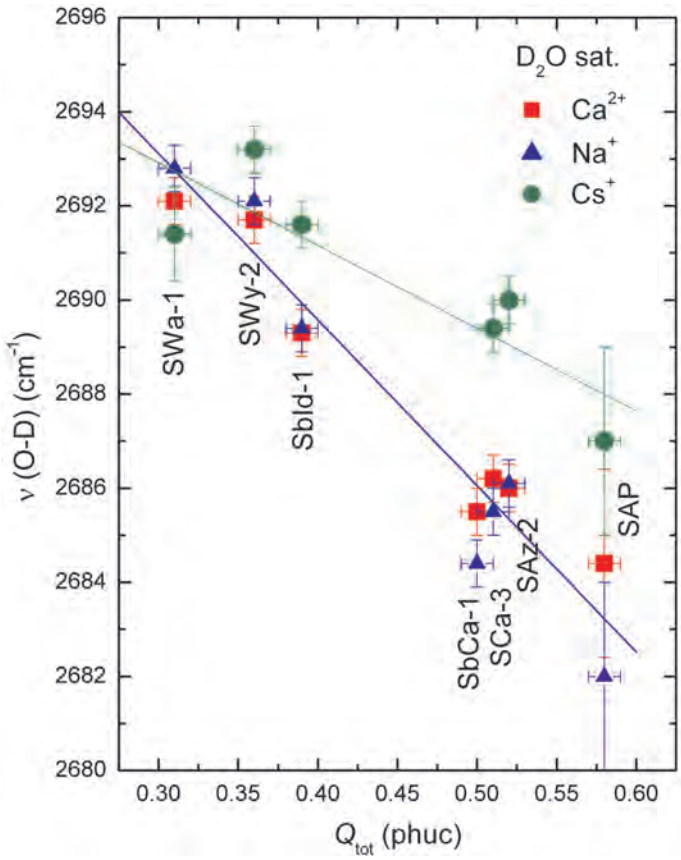

Figure 8. Dependence of the position of the sharp, high-frequency O–D stretching of D_2O-saturated smectites on total charge per half unit cell (Q_{tot}) and compensating cation (Ca^{2+}, Na^+ and Cs^+). The straight lines are least-squares fits.

studying the spectra in the O–D stretching range (Figure 9). The HDO-saturation experiments of all seven smectites in three cation forms were performed. The sharp, high-energy OD band of HDO was observed in all samples, always at wavelengths 20–30 cm^{-1} lower than in D_2O-saturated samples, in qualitative agreement with Farmer and Russell (1971). A similar dependence on smectite charge and interlayer cation was observed as in the case of D_2O-wetting (Figure 10). In contrast, the strongly H-bonded part of the D_2O stretching domain showed an opposite shift (2506 for D_2O and 2523 cm^{-1} for HDO in the case of Na-SWy-2 – Figure 9). In addition, the ~2400 cm^{-1} component was absent from the spectra of the HDO-smectite, which is consistent with its assignment to a Fermi resonance 2δ D_2O component and simplifies the spectrum of HO–D stretching modes. On the other hand, the advantages of studying HDO- instead of D_2O-saturated smectite samples are counterbalanced by the inevitably weaker intensity of the HO–D stretching envelope, which results in a worse signal-to-noise ratio and the larger bandwidths associated with the isotope combinations in a mixed H-bonded tetrahedral $O(H,D)_4$ network (Max and Chapados, 2002).

Origin of the sharp $O–D_w/O–H_w$ band

Within the %RH range studied, the sharp, high-frequency IR band at ~2685 cm^{-1} (D_2O) or ~3630 cm^{-1} (H_2O) was a common feature for all smectites investigated, with a position and intensity showing remarkable insensitivity to interlayer cation type or interlayer water content, but with noticeable dependence on layer charge (Table 2, Figure 5). An opposite behavior was observed for the ~3400 cm^{-1} (H_2O), and ~2500 cm^{-1} (D_2O) OH_w/OD_w stretching envelopes that exhibited a strong dependence on hydration stage and interlayer cation (*cf.* Xu *et al.*, 2000; Madejová *et al.*, 2002), but were relatively unaffected by the layer charge or charge location of the smectites studied (Figure 4).

Notably, the position of the sharp band showed a negligible difference between the Na- and Ca-forms of any of the smectites studied, despite the large difference in ionic potential and hydration enthalpy between these cations. Cs^+ has the lowest hydration enthalpy among naturally occurring single, non-complex cations. Nevertheless, Cs-smectites obey a weak linear relationship between the OD sharp band position and the total layer charge of smectite although the correlation line slope is different from the Na- and Ca-forms.

The high frequency of the sharp stretching mode suggests its origin from O–H (O–D) oscillators which are involved in very weak or no H-bonding, unlike liquid water and most aqueous ionic salt solutions (Max *et al.*, 2007). According to Libowitzky (1999), O–H stretching frequencies in silicate minerals which are in excess of 3600 cm^{-1} correspond to O···O distances >~3.1–3.2 Å. In contrast to this estimated distance, the average O···O distance of liquid H_2O is ~2.8 Å, while the common perception of the H bond corresponds to O···O distances of <~3.1 Å (Khan, 2000). Lastly, the nearly constant intensity of the high-frequency band over broad ranges of water content indicates that the H_2O species responsible for this band is not sensitive to the actual expansion of the interlayer which does depend on water content (*cf.* Ferrage *et al.*, 2010). The origin of the sharp band from the water interface on the siloxane surface seems, therefore, the only valid mechanism, because its occurrence, position, and – on a qualitatively observable level – its intensity do not depend directly on the interlayer cation; neither does the band represent the bulk of the interlayer water.

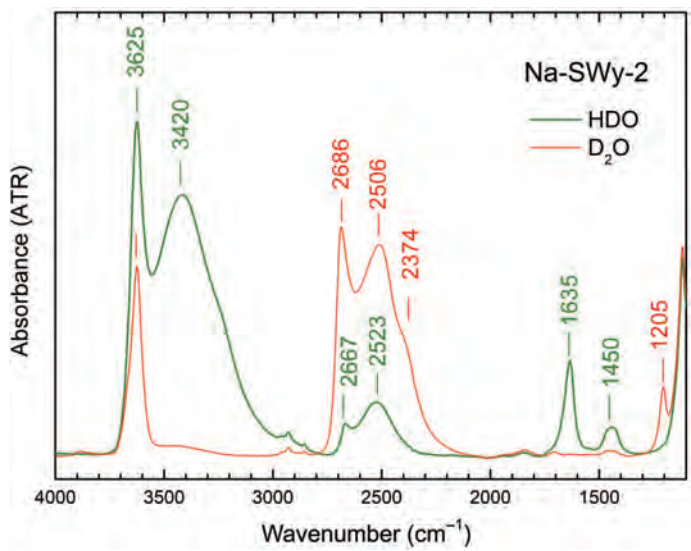

Figure 9. Comparison of the ATR-IR spectra of HDO- and D_2O-saturated Na-SWy-2 montmorillonite.

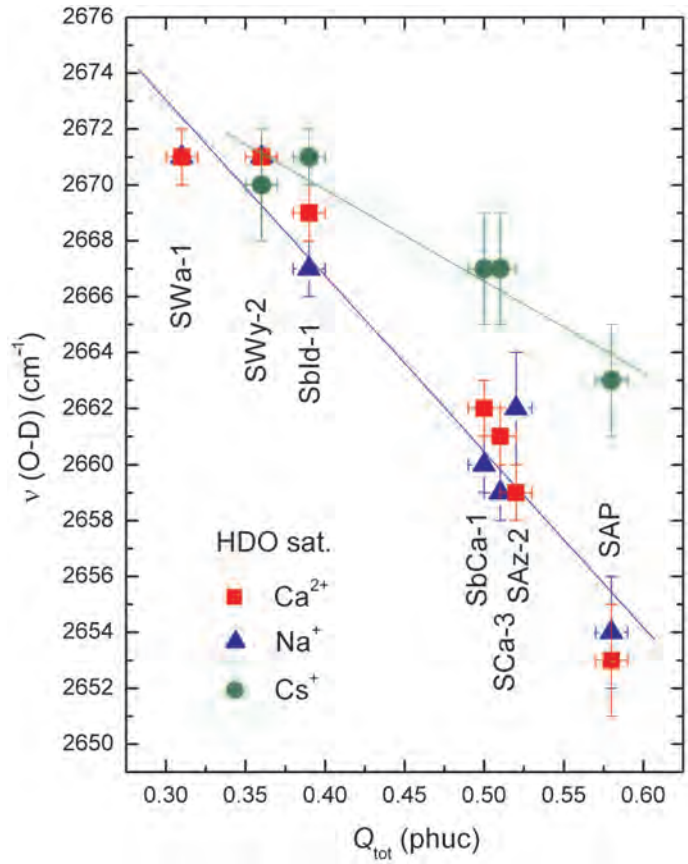

Figure 10. Same as Figure 8, based on HDO-saturated smectites.

O−H stretching bands at frequencies similar to or even greater than those reported here have been observed at the interface of H_2O with hydrophobic solids (*e.g.* silica, Jena and Hore, 2010) or liquids (*e.g.* CCl_4, Scatena *et al.*, 2001), or at the water−vapor interface (Sovago *et al.*, 2009; Tian and Shen, 2009) and are interpreted as modes of so-called 'dangling' OH (Shen and Ostroverkhov, 2006; Auer and Skinner, 2009; Sovago *et al.*, 2009; Tian and Shen, 2009; Zhang *et al.*, 2009; Chakraborty and Chandra, 2012; Davis *et al.*, 2012), *i.e.* vibration of OH groups that are involved in only very weak or non-existent interactions with other atoms. Notably, the siloxane surface of smectite is classified as mostly hydrophobic, based on aromatic-hydrocarbon adsorption experiments (Jaynes and Boyd, 1991).

In contrast, hydrophilic silica with surface SiOH and SiO^- groups exhibits no high-frequency component of the adsorbed water, as was shown using sum frequency vibrational spectroscopy (Shen and Ostroverkhov, 2006). After making the silica surface hydrophobic by coating it with organic molecules, the sharp, high-frequency band appeared (Shen and Ostroverkhov, 2006; Zhang *et al.*, 2009). Increasing the silica-surface hydrophobicity increased the intensity of the band and shifted the position of the band to higher frequencies (Zhang *et al.*, 2009).

The interpretation presented here is in accord with the conclusions of several early experimental studies on water−smectite interactions (*e.g.* Russell and Farmer, 1964; Farmer and Russell, 1971; Suquet *et al.*, 1977; Sposito and Prost, 1982; Sposito *et al.*, 1983) which identified the high-frequency OH_w band and linked it to H_2O molecules at the surface of the interlayer, pointing one of their O−H bonds towards the siloxane surface ('dangling') and the other towards the 'bulk' interlayer. Further support for this interpretation comes from theoretical studies of smectite hydration. Spatial arrangement of H_2O molecules with one or two OH directed toward the siloxane surface was proposed by the theoretical calculations of Prost and Chaussidon (1969) and the molecular dynamics simulations of Sposito *et al.* (1999), Suzuki and Kawamura (2004), Wang *et al.* (2005), and Marry *et al.* (2008).

Based on the considerations above, the high-frequency water OH(OD) stretching band is associated with water molecules at the interface with the siloxane sheet and with at least one OH(OD) group pointing toward the surface, *i.e.* in weak interaction with its siloxane O atoms and with negligible influence by interlayer

cations. Indeed, within the resolution of the experiments performed, the only dependence of this band on the type of smectite was a small decrease in its frequency upon increasing layer charge. The observed shift of the band position was consistent with the development of some attractive interactions between the hydroxyl group of water and the increasingly charged 2:1 layer which would reduce the vibrational frequency of the dangling hydroxyl group. If confirmed on a large set of smectites, the high-frequency $OH(D)_w$ band may become a probe to measure the total layer charge of smectite.

CONCLUSIONS

The present study has provided new evidence in support of an old, sometimes forgotten idea about the structure of H_2O molecules in the interlayer space of smectite minerals. A population of H_2O located in the immediate vicinity of the siloxane surface and interacting very weakly with it has been identified by the ubiquitous presence of a high-frequency, sharp H_2O (D_2O) band at ~3630 cm^{-1} (2685 cm^{-1}). In dioctahedral aluminous smectites, this band nearly coincides with the stretching modes of the structural OH groups which may explain why it has not been identified in some studies as an H_2O vibration. The IR investigation of D_2O-saturated smectites, instead of the commonly studied H_2O analogs, re-emerges, therefore, as a valuable tool for the investigation of bands originating from both water molecules and structural OH groups, and free of the problematic overlap.

In agreement with early IR studies and recent studies of water at interfaces, the sharp, high-frequency H_2O (D_2O) band is assigned to O−H pointing away from the 'bulk' interlayer and toward the siloxane surface. The position of this band is nearly independent of the cation (Na^+, Ca^{2+}) and its intensity remained constant over broad hydration ranges, such as those achieved with 60−80% relative humidity at ambient temperature. A linear dependence of the sharp band position on the total layer charge of a smectite was found. Based on this dependence, it appears that the total layer charge, Q_{tot}, can be estimated from the position of the high-frequency O−D_w stretching band with an uncertainty of the order of ±0.03 e^-/half unit cell in Na- or Ca-smectites. This preliminary correlation is very promising and requires more data to confirm the trend. The relationship should be checked for the possible presence of systematics specific to octahedral structure (trioctahedral *vs*. dioctahedral, *cis*-vacant *vs*. *trans*-vacant) or charge location (octahedral *vs*. tetrahedral). A caveat that needs to be emphasized is that the exact position of the high-frequency OD_w depends on whether it is determined from maxima in absorbance spectra or minima in the 2nd derivative spectra. A 2nd derivative pre-processing of the spectra is recommended to improve the resolution of the sharp peak against the overlapping broad liquid-like band envelope. A calibration transfer may, therefore, be needed if the peak-picking algorithm is different from that employed in this work.

Finally, the identification of the OH_w contribution to the ~3620 cm^{-1} band of dioctahedral aluminous smectites is essential in assigning correctly the sharp ~5230 cm^{-1} near-IR feature (Cariati *et al.*, 1981, 1983) to a (ν+δ) stretching-bending combination of H_2O in smectites. The sharp band combination mode is particularly intense in the near-IR due to the effect of H-bonding on the anharmonicity of the O−H stretch (Sándorfy, 2006). This opens up the possibility of obtaining similar layer-charge diagnostics from the systematics of the (ν+δ) OH_w combination of H_2O in smectites using the near-IR, more conveniently and without the need for D_2O saturation of samples.

ACKNOWLEDGMENTS

The authors thank the editors and reviewers for valuable suggestions that helped to improve the manuscript. They are also grateful to Jarosław Kieć for technical assistance. This project was made possible with financial support from project REGPOT-2011-1 under the European Union 7th Framework Programme, No 285989 (ATLAB) and the IGS-PAS research grant for young scientists "Dehydration of smectites – a FTIR, TG and stable isotopes study". Partial support by project KRHPIS 447963 - Polynano (GSRT, TPCI-NHRF) is also acknowledged. This work was performed to partially fulfill the requirements of a PhD thesis by A. Kuligiewicz.

REFERENCES

Aurer, B.M. and Skinner, J.L. (2009) Water: Hydrogen bonding and vibrational spectroscopy, in the bulk liquid and at the liquid/vapor interface. *Chemical Physics Letters*, **470**, 13−20.

Bertie, J.E., Ahmed, M.K., and Eysel, H.H. (1989) Infrared intensities of liquids. 5. Optical and dielectric constants, integrated intensities, and dipole moment derivatives of H_2O and D_2O at 22ºC. *Journal of Physical Chemistry*, **93**, 2210−2218.

Besson, G. and Drits, V.A. (1997) Refined relationships between chemical composition of dioctahedral fine-grained mica minerals and their infrared spectra within the OH stretching region. Part I: Identification of the OH stretching bands. *Clays and Clay Minerals*, **45**, 158−169.

Bishop, J.L., Pieters, C.M., and Edwards, J.O. (1994) Infrared spectroscopic analyses in the nature of water in montmorillonite. *Clays and Clay Minerals*, **42**, 702−716.

Bukas, V.J., Tsampodimou, M., Gionis, V., and Chryssikos, G.D. (2013) Synchronous ATR infrared and NIR-spectroscopy investigation of sepiolite upon drying. *Vibrational Spectroscopy*, **68**, 51−60.

Bukka, K., Miller, J.D., and Shabtai, J. (1992) FTIR study of deuterated montmorillonites: Structural features relevant to pillared clay stability. *Clays and Clay Minerals*, **40**, 92−102.

Cariati, F., Erre, L., Micera, G., Piu, P., and Gessa C. (1981) Water molecules and hydroxyl groups in montmorillonites as studied by near infrared spectroscopy. *Clays and Clay Minerals*, **29**, 157−159.

Cariati, F., Erre, L., Micera, G., Piu, P., and Gessa C. (1983) Polarization of water molecules in phyllosilicates in relation to exchange cations as studied by near infrared spectro-

scopy. *Clays and Clay Minerals*, **31**, 155–157.
Chakraborty, D. and Chandra, A. (2012) A first principles simulation study of fluctuations of hydrogen bonds and vibrational frequencies of water at liquid–vapor interface. *Chemical Physics*, **392**, 96–104.
Chiou, C.T. and Rutherford, D.W. (1997) Effects of exchanged cation and layer charge on the sorption of water and EGME vapors on montmorillonite clays. *Clays and Clay Minerals*, **45**, 867–880.
Clark, R.N., King, T.V.V., Klejwa, M., Swayze, G.A., and Vergo, N. (1990) High spectral resolution reflectance spectroscopy of minerals. *Journal of Geophysical Research*, **95B**, 12653–12680.
Davis, J.G., Gierszal, K.P., Wang, P., and Ben-Amotz, D. (2012) Water structural transformation at molecular hydrophobic interfaces. *Nature*, **491**, 582–585.
Efimov, Y.Y. and Naberhukhin, Y.I. (2002) On the interrelation between frequencies of stretching and bending vibrations in liquid water. *Spectrochimica Acta A*, **58**, 519–524.
Farmer, V.C. (1974) The layer silicates. Pp 331–363 in: *The Infrared Spectra of Minerals* (V.C. Farmer, editor). Monograph **4**, Mineralogical Society, London.
Farmer, V.C and Russell, J.D. (1971) Interlayer complexes in layer silicates: The structure of water in lamellar ionic solutions. *Transactions of the Faraday Society*, **67**, 2737–2749.
Ferrage, E., Lanson, B., Michot, L.J., and Robert, J.-L. (2010) Hydration properties and interlayer organization of water and ions in synthetic Na-smectite with tetrahedral layer charge. Part 1. Results from X-ray diffraction profile modeling. *The Journal of Physical Chemistry C*, **114**, 4515–4526.
Fialips, C.-I., Huo, D., Yan, L., Wu, J. and Stucki, J.W. (2002) Effect of Fe oxidation state on the IR spectra of Garfield nontronite. *American Mineralogist*, **87**, 630–641.
Fu, M.H., Zhang, Z.Z. and Low, P.F. (1990) Changes in the properties of a montmorillonite-water system during the adsorption and desorption of water: Hysteresis. *Clays and Clay Minerals*, **38**, 482–492.
Gates, W. P. (2005) Infrared spectroscopy and the chemistry of dioctahedral smectites. Pp. 126–168 in: *The Application of Vibrational Spectroscopy to Clay Minerals and Layered Double Hydroxides* (J.T. Kloprogge, editor). CMS Workshop Lectures, Vol. **13**, The Clay Minerals Society, Boulder, Colorado, USA.
Jackson, M.L. (1969) Dispersion of soil minerals. Pp. 29–91 in: *Soil Chemical Analysis – Advanced Course*. 2nd edition. Published by the author, Madison, Wisconsin, USA.
Jaynes, W.F. and Boyd, S.A. (1991) Hydrophobicity of siloxane surfaces in smectites as revealed by aromatic hydrocarbon adsorption from water. *Clays and Clay Minerals*, **39**, 428–436.
Jena, C.J. and Hore, D.K. (2010) Water structure at solid surfaces and its implications for biomolecule adsorption. *Physical Chemistry Chemical Physics*, **12**, 14383–14404.
Johnston, C.T., Sposito, G., and Erickson, C. (1992) Vibrational probe studies of water interactions with montmorillonite. *Clays and Clay Minerals*, **40**, 722–730.
Khan A. (2000) A liquid water model: Density variation from supercooled to superheated states, prediction of H-bonds, and temperature limits. *Journal of Physical Chemistry B*, **104**, 11268–11274.
Libowitzky, E. (1999) Correlation of O-H stretching frequencies and O-H···O bond lengths in minerals. *Monatshefte für Chemie*, **130**, 1047–1059.
Madejová, J. (2003) FTIR techniques in clay mineral studies. *Vibrational Spectroscopy*, **31**, 1–10.
Madejová, J. and Komadel, P. (2001) Baseline studies of the Clay Minerals Society Source Clays: Infrared methods. *Clays and Clay Minerals*, **49**, 410–432.
Madejová, J., Komadel, P., and Čičel, B. (1994) Infrared study of octahedral site populations in smectites. *Clay Minerals*, **29**, 319–326.
Madejová, J., Janek, M., Komadel, P., Herbert, H.-J., and Moog, H.C. (2002) FTIR analyses of water in MX-80 bentonite compacted from high salinary salt solution systems. *Applied Clay Science*, **20**, 255–271.
Marry, V., Rotenberg, B., and Turq, P. (2008) Structure and dynamics of water at a clay surface from molecular dynamics simulation. *Physical Chemistry Chemical Physics*, **10**, 4802–4813.
Max, J.-J. and Chapados, C. (2002) Isotope effects in liquid water by infrared spectroscopy. *Journal of Chemical Physics*, **116**, 4626–4642.
Max, J.-J. and Chapados, C. (2009) Isotope effects in liquid water by infrared spectroscopy. III. H_2O and D_2O spectra from 6000 to 0 cm^{-1}. *Journal of Chemical Physics*, **131**, 184505, 1–13.
Max, J.-J., Gessinger, V., van Driessche, C., Larouche, P., and Chapados, C. (2007) Infrared spectroscopy of aqueous ionic salt solutions at low concentrations. *Journal of Chemical Physics*, **131**, 184507, 1–14.
Pelletier, M., Michot, L.J., Humbert, B., Barrès, O., d' Espinose de la Caillerie, J.-B., and Robert, J.-L. (2003) Influence of layer charge on the hydroxyl stretching of trioctahedral clay minerals: A vibrational study of synthetic Na- and K-saponites. *American Mineralogist*, **88**, 1801–1808.
Petit, S., Robert, J-L., Decarreau, A., Besson, G., Grauby, O., and Martin, F. (1995) Apport des méthodes spectroscopiques à la caractérisation des phyllosilicates 2:1. *Bulletin de Centre des Recherches Exploration-Production ELF-Aquitaine*, **19**, 119–147.
Petit, S., Caillaud, J., Righi, D., Madejová, J., Elsass, F., and Köster, H.M. (2002) Characterization and crystal chemistry of an Fe-rich montmorillonite from Ölberg, Germany. *Clay Minerals*, **37**, 283–297.
Prost, R. and Chaussidon, J. (1969) The infrared spectrum of water adsorbed in hectorite. *Clay Minerals*, **8**, 143–149.
Ras, R.H.A., Umemura, Y., Johnston, C.T., Yamagishi, A., and Schoonheydt, R.A. (2007) Ultrathin hybrid films of clay minerals. *Physical Chemistry Chemical Physics*, **9**, 918–932.
Russell, J.D. and Farmer, V.C. (1964) Infrared spectroscopic study of the dehydration of montmorillonite and saponite. *Clay Minerals Bulletin*, **5**, 443–464.
Russell, J.D. and Fraser, A.R. (1994) Infrared methods. Pp. 11–67 in: *Clay Mineralogy: Spectroscopic and Chemical Determinative Methods* (M.J. Wilson, editor). Chapman and Hall, London.
Russell, J.D., Farmer, V.C., and Velde, B. (1970) Replacement of OH by OD in layer silicates, and identification of the vibrations of these groups in infra-red spectra. *Mineralogical Magazine*, **37**, 869–879.
Sándorfy, C. (2006) Hydrogen bonding: How much anharmonicity? *Journal of Molecular Structure*, **790**, 50–54.
Scatena, L.F., Brown, M.G., and Richmond, G.L. (2001) Water at hydrophobic surfaces: Weak hydrogen bonding and strong orientation effects. *Science*, **292**, 908–912.
Shen, Y.R. and Ostroverkhov, V. (2006) Sum-frequency vibrational spectroscopy on water interfaces: Polar orientation of water molecules at interfaces. *Chemical Reviews*, **106**, 1140–1154.
Sovago, M., Kramer Campen, R.K., Bakker H.J., and Bonn, M. (2009) Hydrogen bonding strength of interfacial water determined with surface sum-frequency generation. *Chemical Physics Letters*, **470**, 7–12.
Sposito, G. and Prost, R. (1982) Structure of water adsorbed on

smectites. *Chemical Reviews*, **82**, 554–573.

Sposito, G., Prost, R., and Gaultier, J.-P. (1983) Infrared spectroscopic study of adsorbed water on reduced-charge Na/Li-montmorillonites. *Clays and Clay Minerals*, **31**, 9–16.

Sposito, G., Skipper, N.T., Sutton, R., Park, S-H., Soper, A.K., and Greathouse, J.A. (1999) Surface geochemistry of clay minerals. *Proceedings of National Academy of Science USA*, **96**, 3358–3364.

Suquet, H., Prost, R., and Pezerat, H. (1977) Etude par la spectroscopie infrarouge de l' eau adsorbée par la saponite-calcium. *Clay Minerals*, **12**, 113–125.

Suzuki, S. and Kawamura, K. (2004) Study of vibrational spectra of interlayer water in sodium beidellite by molecular dynamics simulations. *Journal of Physical Chemistry B*, **108**, 13468–13474.

Tian C.S. and Shen Y.R. (2009) Sum-frequency vibrational spectroscopic studies of water/vapor interfaces. *Chemical Physics Letters*, **470**, 1–6.

Wang J., Kalinichev A.G., Kirkpatrick R.J., and Cygan R.T. (2005) Structure, energetics, and dynamics of water adsorbed on the muscovite (001) surface: A molecular dynamics simulation. *Journal of Physical Chemistry B*, **109**, 15893–15905.

Wolters, F., Lagaly, G., Kahr, G., Nueesch, R., and Emmerich, K. (2009) A comprehensive characterization of dioctahedral smectites. *Clays and Clay Minerals*, **57**, 115–133.

Xu, W., Johnston, C.T., Parker, P., and Agnew, S.F. (2000) Infrared study of water sorption on Na-, Li-, Ca- and Mg-exchanged (SWy-1 and SAz-1) montmorillonite. *Clays and Clay Minerals*, **48**, 120–131.

Yan, L.B., Roth, C.B., and Low, P.F. (1996) Changes in the Si-O vibrations of smectite layers accompanying the sorption of interlayer water. *Clays and Clay Minerals*, **12**, 4421–4429.

Zhang, L., Singh, S., Tian, C., Shen, Y.R., Wu, Y., Shannon, M., and Brinker, C.J. (2009) Nanoporous silica–water interfaces studied by sum-frequency vibrational spectroscopy, *The Journal of Chemical Physics*, **130**, 154702.

Zviagina, B.B., McCarty, D., Środoń, J., and Drits, V.A. (2004) Interpretation of infrared spectra of dioctahedral smectites in the region of OH-stretching vibrations. *Clays and Clay Minerals*, **52**, 399–410.

(*Received 31 July 2014; revised 11 February 2015; Ms. 905; AE: A.G. Kalinichev*)

Clays and Clay Minerals, Vol. 63, No. 1, 30–42, 2015.

PREDICTION OF COMPRESSIBILITY DATA FOR HIGHLY PLASTIC CLAYS USING DIFFUSE DOUBLE-LAYER THEORY

TADIKONDA VENKATA BHARAT[1,*] AND ASURI SRIDHARAN[2]

[1] Department of Civil Engineering, Indian Institute of Technology Guwahati, Guwahati – 781039, Assam, India
[2] Indian National Science Academy, New Delhi, India

Abstract—Montmorillonite-rich clays are important in many engineering applications. The compressibility of such plastic clays at high consolidation pressures is important for predicting routine settlement and for applications in nuclear-waste repositories. Laboratory measurement of compressibility data at high consolidation pressures is not only time consuming but very expensive also. Theoretical predictions can help to determine the compressibility of plastic clays at high consolidation pressures. A linear relationship between e/e_N *vs.* $1/\sqrt{P}$ (e_N is the normalization void ratio at normalization pressure N and P is the consolidation pressure) was derived using diffuse double-layer theory. The compressibility data of several plastic clays in published studies were found to support the derived relationship. A generalized theoretical equation was proposed to predict the compressibility data over a wide range of consolidation pressures using an experimentally measured void ratio at low consolidation pressure. The compressibility data for different plastic clays were predicted accurately up to maximum consolidation pressures that ranged from 0.7 to 30 MPa using an experimentally measured void ratio near the pre-consolidation pressure. The pre-consolidation pressures for different clays considered here ranged from 25 to 133 kPa. The proposed predictive model is supported by experimental data, is simple, and does not require knowledge of clay-surface and pore-fluid parameters.

Key Words—Compressibility Behavior, Diffuse Double-Layer Theory, High Consolidation Pressures, Plastic Clays, Predictive Model.

INTRODUCTION

Compacted plastic clays that contain high percentages of montmorillonite minerals (*e.g.* bentonitic clays) are of much interest as barrier material in waste-disposal facilities for isolation of toxic wastes (Pusch and Yong, 2006; Tripathy and Schanz, 2007; Zheng *et al.*, 2011; Sellin and Leupin, 2014). Compacted plastic clays are also used extensively as backfilling materials for sealing the excavated tunnels (Tripathy and Schanz, 2007). Typical initial void ratios of such highly plastic clays are in the range 10–30 (Marcial *et al.*, 2002). The void ratio is defined as the ratio between the volume of soil voids and the volume of soil solids.

The *in situ* settlement behavior of plastic clays under the anticipated pressures is of great interest for engineering applications. Compressibility data (*i.e.* interrelationship between void ratio (e) and consolidation pressure (P)) from laboratory consolidation tests on representative clay samples are useful for predicting the *in situ* settlement. The determination of compressibility data is, therefore, undertaken routinely in the laboratory and requires several days of careful measurements.

Toxic-waste repositories are usually constructed at depths of several hundred meters below the ground surface and are surrounded by saturated host rock. The performance assessment of such repositories, therefore, requires compressibility/consolidation characteristics at consolidation pressures beyond 600 kPa. Specialized experimental apparatus is required for measuring the compressibility data at such high consolidation pressures due to limitations associated with conventional oedometers (Baille *et al.*, 2010). Measurement of compressibility data at high consolidation pressures is, therefore, not only laborious, but time consuming and expensive. Simple theoretical models are useful for predicting the compressibility data of plastic clays over a wide range of consolidation pressures.

Physicochemical factors such as clay-mineral composition, cation exchange capacity (CEC), specific surface area (SSA), and pore-fluid chemistry control the compressibility behavior of plastic clays (Bolt, 1956; Mesri and Olsen, 1971; Sridharan and Rao, 1973; Sridharan *et al.*, 1986; Mitchell, 1993; Abdullah *et al.*, 1997; Robinson and Allam, 1998; Sridharan and Choudhury, 2002; Sridharan and Choudhury, 2008; Bharat *et al.*, 2013). The applicability of diffuse double layer (DDL) theory to understand compressibility behavior of highly plastic clays and the qualitative prediction of compressibility data using DDL theory on experimental data have been reported by several researchers (Bolt, 1956; Sridharan and Jayadeva, 1982; Tripathy *et al.*, 2004; Tripathy and Schanz, 2007). Relationships between non-dimensional, mid-plane electric potentials and the distances between the particles for different ranges of 'averaged' valences using the DDL

* E-mail address of corresponding author:
tvb@iitg.ernet.in
DOI: 10.1346/CCMN.2015.0630103

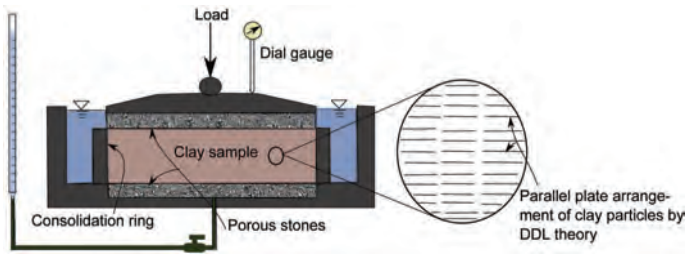

Figure 1. Laboratory oedometer set-up for the measurement of consolidation data.

theory were established by Tripathy *et al.* (2004). The established theoretical relationships were modified by adjusting the equation coefficients to match the experimental compressibility data of commonly used bentonitic clays, *i.e.* MX80, Febex, and Montigel. The established empirical relations were, however, derived from specific experimental data and were valid for limited ranges of averaged ion valences *i.e.* 1.66−1.73 and 1.97. The applicability of these equations, therefore, is not guaranteed for a wide range of clays. This method, further, requires the determination of clay-surface and pore-fluid parameters for prediction. The quantitative prediction of compressibility data of plastic clays for a wide range of such clays remains to be completed, however.

The objective of the present study was to predict quantitatively the compressibility data using theoretical models. A linearization model for compressibility data using DDL theory was developed which was supported by the experimental data. A predictive model was then developed using the proposed linearization procedure for predicting the compressibility data using three normalization void ratios. A generalized theoretical equation relating the normalized void ratio with $\sqrt{P}$ was derived to predict the compressibility data over a wide range of consolidation pressures using a single experimentally measured void ratio at pre-consolidation pressure. The performance of the predictive model was validated by comparison with several measured compressibility data from the literature. The proposed method offered several advantages over the existing methods as it did not require knowledge of clay-surface and pore-fluid parameters, unlike previous methods. The new method will reduce the cost of routine laboratory experimentation and the cost of experimentation on specialized and sophisticated equipment for measuring the compressibility data at high consolidation pressures. The method requires only a single experimentally measured void ratio value, just beyond the pre-consolidation pressure.

MATERIALS AND METHODS

Diffuse double-layer theory

The volume of a laterally confined clay specimen decreases with increase in the external pressure. The compressibility behavior of plastic clays is studied using laboratory consolidation tests (Figure 1). The void ratios of saturated clay specimens are measured under applied consolidation pressure to establish the constitutive relationship between e and P. The compressibility behavior of clays containing large percentages of montmorillonite (*e.g.* bentonitic clays) under externally applied pressures depends on physicochemical interaction between the mineral surfaces and the chemical composition of the surrounding liquid phase, *i.e.* pore-fluid. The compressibility behavior of clays can, therefore, be studied theoretically if the clay-water-electrolyte system is assumed to consist of a parallel plate system (Figure 1). The interaction between clay particles and the surrounding diffuse double layer containing exchangeable ions leads to the existence of repulsive pressures between the particles (Figure 2). The osmotic pressure (ϕ_d) thus developed between the interacting diffuse double layers at equilibrium is the measure of

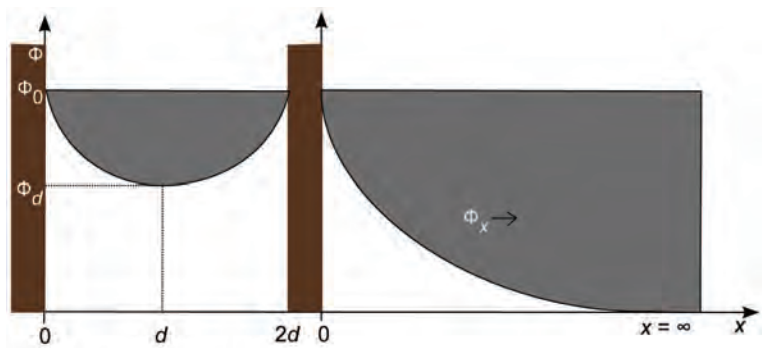

Figure 2. Electrostatic potential distribution around parallel and single clay platelets according to GC theory.

consolidation pressure (Bolt, 1956). The mid-plane distance ($x = d$) between the clay particles at equilibrium is a measure of void ratio and is a measurable parameter in the laboratory. The decrease in particle distance results in increase in the osmotic pressure (or decrease in void ratio) with increase in the consolidation pressure in a macro-scale representation. The DDL theory is, therefore, useful in relating the microscopic parameters (ϕ_d, d) with the macroscopic compressibility parameters (P, e) of clay by assuming a parallel plate configuration of DDL plates (Figure 2). Changes in the thickness of DDLs due to changes in the pore-fluid composition can be related directly to the changes in void ratio at a given consolidation pressure using the theory.

The Gouy–Chapman (GC) model, proposed independently by Gouy (1910) and Chapman (1913), assumes Boltzmann distribution of ions in the double layer (Verwey and Overbeek, 1948). The GC model is the most commonly used DDL theory to understand qualitatively the compressibility behavior of plastic clays due to variations in the clay–water–electrolyte interactions (Sridharan and Jayadeva, 1982; Yong and Mohamed, 1992; Tripathy *et al.*, 2004; Bharat *et al.*, 2013; Sridharan, 2014). The assumptions associated with the GC model (McBride, 1997), however, limit the application for quantitative understanding of the engineering behavior (Sridharan and Jayadeva, 1982). Some of the limitations of GC theory are: (1) The clay-water-electrolyte system is assumed to consist of parallel DDL plates. The fabric of the clay, however, changes due to several factors. The effect of particle orientation (Anandarajah and Lu, 1991) is too complex to incorporate in the analysis. (2) The cations are assumed to be point charges and distributed around the particles (van Olphen, 1963). The size of the cations is not taken into consideration in the theory, therefore. Cation size was shown by Sridharan *et al.* (1986) to influence the compressibility of clays. (3) The theory is not applicable to analysis of the consolidation behavior of clays when the pore-fluid concentration is >0.001 M. The anion concentration dominates in the DDL when the pore-fluid concentration is >0.001 M (Yong *et al.*, 1962). (4) A precise estimate of the surface properties of the clay particles is required for the theory. Precise measurement of clay-surface propertiesis difficult, however (Hang and Brindley, 1970; Chan *et al.*, 1984; Santamarina *et al.*, 2002).

All the aforementioned limitations affect the other models also. The Stern model distinguishes the presence of different cations of the same valence in the Stern layer, but the application of such theories is limited to a system of constant surface potential (van Olphen, 1963; Chan *et al.*, 1984; Tripathy *et al.*, 2014). The Stern model cannot, therefore, be used to study the compressibility behavior of clays, where interacting DDL clay platelets are encountered (Tripathy *et al.*, 2014). The GC theory is, therefore, found to be the only alternative for qualitative understanding of the engineering behavior of clays, where interacting DDL plates are encountered. Theoretical predictions for the compressibility behavior are scarce due to the aforementioned limitations in the theory. A novel approach was introduced here for quantitative prediction of compressibility behavior of plastic clays using a GC model.

Experimental results

The compressibility data of several plastic clays with different clay-surface properties and pore-fluid chemistries were considered in the literature. Initial void ratios for all of the selected clays were in the range of 13 (Oikawa, 1987) to 41 (Low, 1980). Compressibility data of these clays were linearized for developing a predictive model. The experimental data were, further, used to validate the proposed predictive model. The relevant properties of the soils as reported in the literature are summarized in Table 1. The experimental compressibility data of all of the selected plastic clays showed (Figure 3) that the relationship between void ratio and consolidation pressure was very non-linear and was dependent on the clay-water-electrolyte properties. The compressibility data were generally convex beyond a consolidation pressure of 30 kPa. The pre-consolidation pressure for most of the selected plastic clays was, therefore, <50 kPa. The differences in the compressibility data for different clays were, however, significant up to a consolidation pressure of ~1000 kPa.

Table 1. Properties of plastic clays.

Clay type	Properties						Reference
	Specific gravity	Liquid limit (%)	Plastic limit (%)	CEC (meq/100 g)	SSA (m^2/g)	% Clay	
Na-Ca MX80	2.65	520	62	68.0	700	85	Marcial *et al.* (2002)
Na-Kunigel	2.79	474	27	73.2	687	64	Marcial *et al.* (2002)
Upton #1	2.80[#]	1531*	–	90.0	800	100	Low (1980)
Yugoslav	2.80[#]	948.7*	–	89.5	559	100	Low (1980)

* Moisture content corresponding to 2.5 kPa consolidation pressure
[#] Assumed

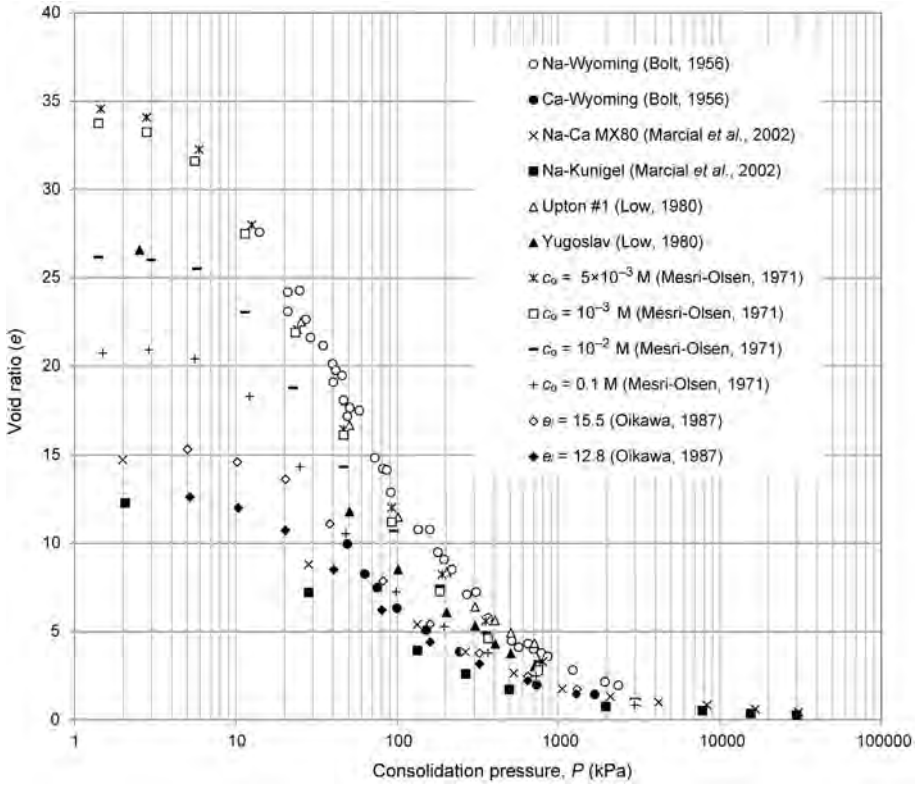

Figure 3. Experimental compressibility data for selected clays.

THEORETICAL COMPRESSIBILITY CURVES

Theoretical compressibility data for plastic clays were obtained using the GC model for developing a predictive model. Theoretical equations describing the inter-relationships between void ratio and consolidation pressure for different clay–water–electrolyte interactions were arranged as shown below (Sridharan and Jayadeva, 1982):

$$P = 2c_0 RT(\cosh y_d - 1) \quad (1)$$

$$\left(\frac{dy}{d\xi}\right)_{x=0} = -\frac{CEC}{SSA}\left(\frac{2513.6}{\sqrt{\varepsilon c_0 T}}\right) \quad (2)$$

$$\left(\frac{dy}{d\xi}\right)_{x=0} = -(2\cosh(y_0) - 2\cosh(y_d))^{1/2} \quad (3)$$

$$\kappa d = -\int_{y_0}^{y_d} (2\cosh(y) - 2\cosh(y_d))^{-1/2} dy \quad (4)$$

$$e = G\rho_w SSA d \quad (5)$$

where:
CEC = cation exchange capacity (meq/100 g)
SSA = specific surface area of the clay (m^2/g)
P = consolidation pressure (kPa)
R = gas constant
T = absolute temperature
y_d = scaled midway potential ($\nu e' \phi_d / RT$)
ξ = scaled distance (κx)
y = scaled electrostatic potential at any distance ($\nu e' \phi / RT$), x, from the surface of a single clay platelet
ε = dielectric constant,
c_0 = molar concentration of the ions in bulk solution (M)
$k_B T$ = thermal energy per ion (joules)
y_0 = scaled potential at the clay surface ($\nu e' \phi_0 / RT$)
G = specific gravity of soil particles
e = void ratio
ρ_w = density of water (kg/m^3)
d = midway distance between the particles
ϕ values are the electrostatic potentials.

The quantity $1/\kappa$ (units of length) is the characteristic length or 'Debye length' which is expressed as $\sqrt{\frac{\varepsilon k_B T}{8\pi e'^2 \nu^2 c_0}}$, where v is the cation valence in the DDL. Equations 1–5 are valid in the case of symmetrical electrolytes. The determination of the void ratio for any given clay–water–electrolyte system using the aforementioned equations involved computation of the elliptical integral (equation 4). The relationship between e and P was, therefore, established by solving equation 4 numerically and solving the simultaneous equations for P for a given void ratio. A model calculation for obtaining the void ratio from an assumed consolidation pressure using equations 1–5 is given in the Appendix below.

Theoretical data showing void ratio *vs*. consolidation pressure relationship with the variation in clay-water-electrolyte properties obtained using the aforementioned procedure were analyzed (Figures 4a−4d). Theoretical data for different electrolyte concentrations revealed (Figure 4a) that the void ratio decreased with increase in the electrolyte concentration at a given consolidation pressure due to reduction in thickness of double-layer with increase in the concentration. The particles thus come close to each other which encourages flocculation. Decrease in the void ratio with increasing electrolyte concentration was negligible beyond consolidation pressures of 400 kPa for concentrations in the range 0.00001−0.001 M. Application of Boltzmann and Poisson's equations (equations 2−3) in DDL theory is invalid beyond an electrolyte concentration of 0.001 M for consolidation behavior (Yong *et al.*, 1962; Bharat, 2004; Tripathy *et al.*, 2004) as the influence of anion domination in the double layers is ignored in the theory (van Olphen, 1963; Frahm and Diekmann, 1979). The theoretical compressibility data for different exchangeable cation valence showed (Figure 4b) decreases in the void ratio with increasing ion valence which encourages the tendency towards flocculation. Theoretical results were consistent qualitatively with the experimental results of Sridharan *et al.* (1986).

The influence of clay-surface parameters, CEC and SSA, on the compression curve was studied (Figure 4c) by considering common ranges of CEC and SSA values from the published data for different clays (Bolt, 1956; Mesri and Olsen, 1971; Low, 1980; Marcial *et al.*, 2002). The increase in the void ratio was directly proportional to the surface area for a given consolidation pressure as the particles can accommodate greater numbers of exchangeable cations on the surface. The increase in SSA, therefore, encourages the formation of thick double layers and favors dispersion of the particles. A very minor influence of CEC was noticed, however, on theoretical compressibility data.

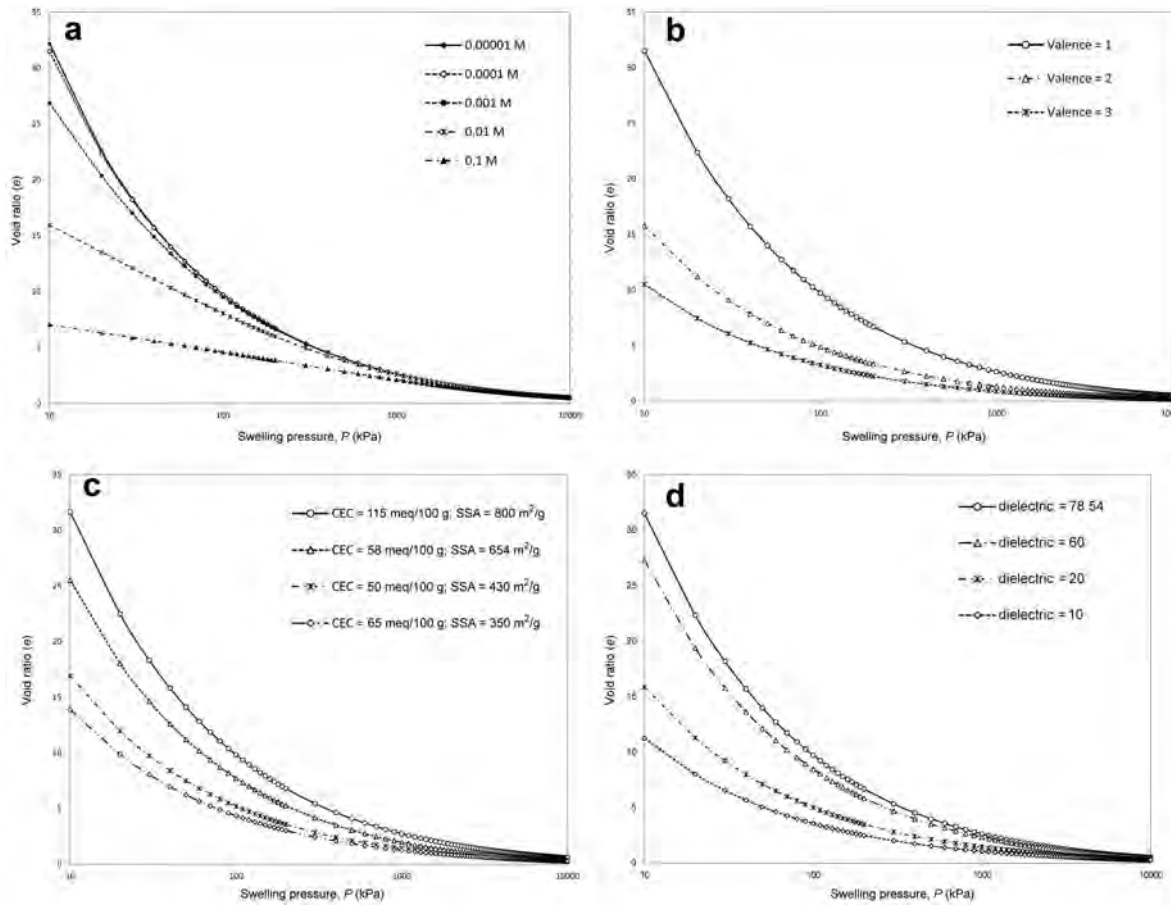

Figure 4. (a) Effect of pore-fluid electrolyte concentrations on void-ratio variation based on GC theory with pressure for assumed values of ε = 78.54; CEC = 100 meq/100 g; SSA = 800 m^2/g; v = 1; T = 298 K. (b) Effect of cation valence on void-ratio variation with pressure based on GC theory for assumed values of c_0 = 0.0001 M; ε = 78.54; CEC = 100 meq/100 g; SSA = 800 m^2/g; T = 298 K. (c) Void-ratio variation with pressure based on GC theory for different clay-surface properties for assumed values of c_0 = 0.0001 M; ε = 78.54; v = 1; T = 298 K. (d) Void-ratio variation with pressure based on GC theory for different dielectric constants of pore fluids for assumed values of c_0 = 0.0001 M; v = 1; CEC = 100 meq/100 g; SSA = 800 m^2/g; T = 298 K.

The influence of the dielectric properties of the pore-fluids on theoretical compressibility data showed (Figure 4d) a decrease in double layer thickness with increase in dielectric constant. The range of dielectric constant values considered in the study represents different pore fluids such as water, ethyl acetate, methyl alcohol, *etc*. The theoretical results of the influence of dielectric constant were qualitatively similar to the experimental results of Sridharan and Rao (1973). The theoretical compressibility data were, therefore, qualitatively accurate and satisfactory.

LINEARIZATION OF THE COMPRESSIBILITY CURVES

The predictive model was developed in two stages. Theoretical compressibility data were normalized in the first stage. The normalized compressibility data were linearized to develop the predictive model in the second stage.

Void ratios of the compressible layer were normalized using different normalization factors, e_N (void ratios corresponding to different consolidation pressures, N). Different normalization factors, *e.g.* e_{50}, e_{100}, and e_{200}, were considered to determine the effective normalization factor. Theoretical compressibility curves are presented (Figures 5a(i)−5d) as normalized void ratio *vs*. consolidation pressure (on a logarithmic scale) using different normalization factors and for different clay-water-electrolyte parameters.

Normalized compressibility data using e_{50} as a normalizing factor for different electrolyte concentrations are presented in Figure 5a(i). All of the data converged to a smooth and unique curve beyond the normalization pressure (50 kPa) when electrolyte concentrations were $\leqslant$0.001 M. The aforementioned trend was not observed for electrolyte concentrations >0.001 M and the scatter is suggested to be due to the applicability of the Boltzmann and van't Hoff equations for electrolyte concentrations >0.001 M (Yong *et al.*, 1962; Tripathy *et al.*, 2004) where the potential distribution follows an exponential behavior (Bharat 2004; Bharat *et al.*, 2013). Plastic clays, moreover, do not display high liquid-limit void ratios and high compressibilities at such concentrations (Castellanos *et al.*, 2008) due to the suppression of DDLs. The theoretical data considered were for $c_0 \leqslant 0.001$ M, therefore. The scatter displayed before the normalization pressure is not expected to affect the prediction, however. Normalized compressibility data using e_{100} showed (Figure 5a(ii)) that the observations were similar to Figure 5a(i) except that the data converged beyond 100 kPa, the normalization pressure in this case. The data for electrolyte concentrations >0.001 M were ignored for the same reasons as mentioned above. Similar results were also observed for e_{200} (not shown here). Normalized compressibility data as e/e_{50} *vs*. P, e/e_{100} *vs*. P, and e/e_{200} *vs*. P for different clay-surface and pore-fluid parameters are presented (Figure 5b−d). The data with all the normalization factors were consistent and were observed to follow a unique relationship.

The normalized compressibility data for different clay-surface and pore-fluid parameters were presented together using three different normalization factors (Figure 6). From the fitted results, all the normalization factors, *e.g.* e_{50}, e_{100}, and e_{200}, were clearly very effective in normalizing the theoretical compressibility data. A simple power relationship was found to exist between e/e_N and consolidation pressure with an exponent of −0.5 and was valid for any clay-water-electrolyte parameters. The results were re-plotted as normalized void ratio *vs*. $1/\sqrt{P}$ (Figure 7) using different clay-surface and pore-fluid parameters as presented above (Figure 4). Linear relationships were observed with high correlation coefficients (R^2), *i.e.* 0.987, 0.988, and 0.981, using the normalization factors of e_{50}, e_{100}, and e_{200}, respectively. Only the compressibility data beyond consolidation pressure of 25 kPa ($1/\sqrt{P} < 0.2$) were considered here as the void ratios under low consolidation pressures are usually influenced by the pre-consolidation effects. The predicted correlation was, therefore, extremely good. The normalized theoretical equations can be written as:

$$e/e_{50} = K_{50}P^{-0.5} \quad (6)$$

$$e/e_{100} = K_{100}P^{-0.5} \quad (7)$$

and

$$e/e_{200} = K_{200}P^{-0.5} \quad (8)$$

where K_{50}, K_{100}, and K_{200}, expressed in $\sqrt{\text{kPa}}$ were proportionality constants equal to 6.7, 9.6, and 13.9, respectively. Equations 6−8 serve as predictive equations because the entire theoretical compressibility curve can be predicted using experimentally measured void ratios corresponding to any consolidation pressure, *e.g.* 50, 100, or 200 kPa. Furthermore, the predictive equations do not require knowledge of the clay-water-electrolyte parameters. The measured normalization void ratio (either e_{50}, e_{100}, or e_{200}) and corresponding proportionality constant (K_{50}, K_{100}, or K_{200}) contained the information about compressibility behavior of clay-water-electrolyte system implicitly. Only values of e_N and K_N were required, therefore, to predict the entire compressibility data. Comparison between equations 6, 7, and 8 revealed that the theoretical relationship using e_{50} appeared to be the most appropriate as the experiments might be conducted only up to lower consolidation pressures when the pre-consolidation pressure of the clay is <50 kPa (*i.e.* normalization pressure). The pre-consolidation pressures of highly plastic clays are, often, very small (<50 kPa).

Experimental data were analyzed to investigate the existence of similar relationships and to compare them with theoretical predictions. Empirical equations were

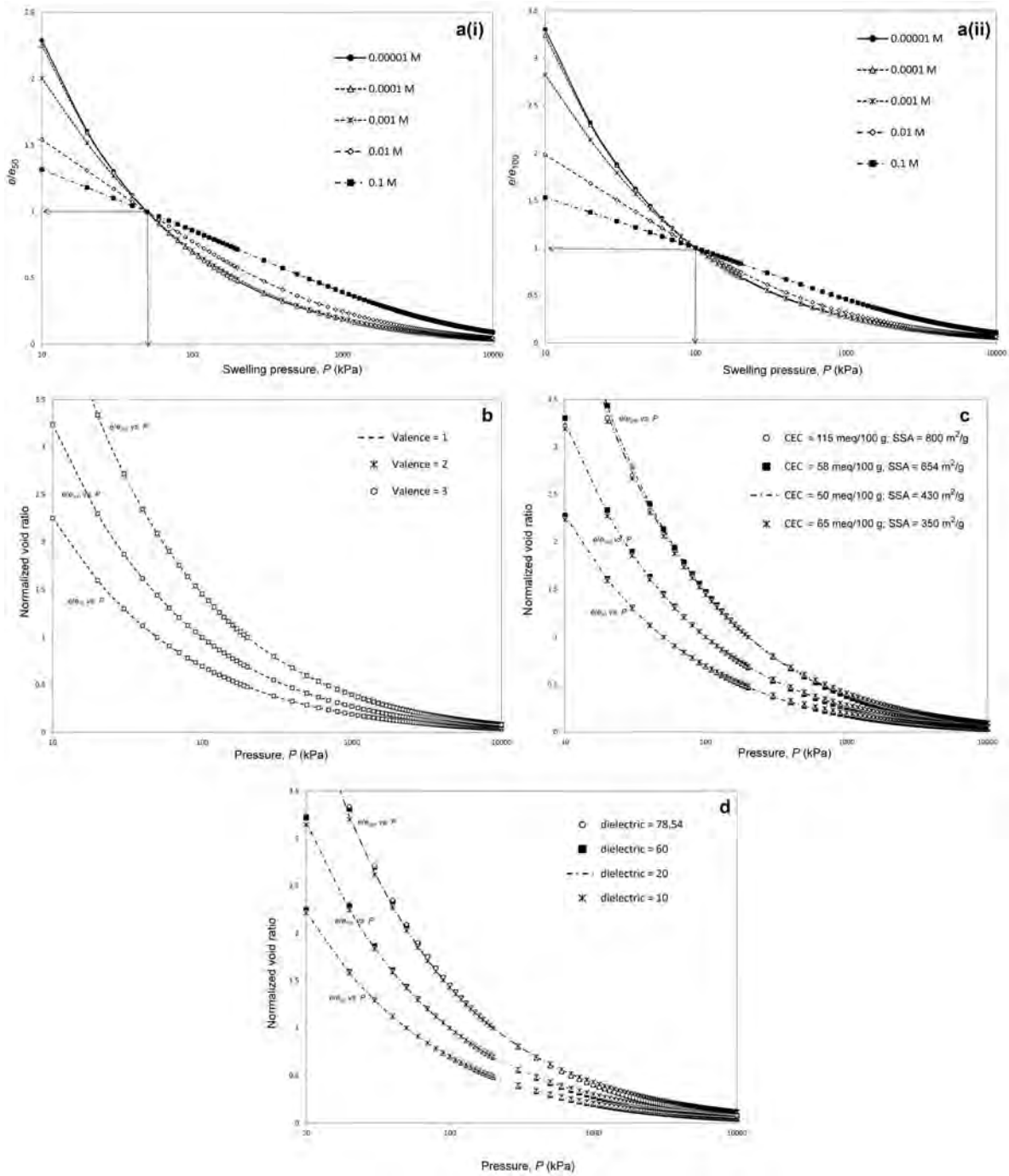

Figure 5. (ai) Normalized compression curves using e_{50} as the normalizing factor for different electrolyte concentrations for the assumed values of $v = 1$; $\varepsilon = 78.54$; CEC = 100 meq/100 g; SSA = 800 m^2/g; $T = 298$ K. (aii) Normalized compression curves using e_{100} as the normalizing factor for different electrolyte concentrations for the assumed values of $v = 1$ and for the same assumed values of ε, c_0, CEC, SSA, and T as above. (b) Normalized compression curves for different cation valence and for the same assumed values of ε, c_0, CEC, SSA, and T as above. (c) Normalized compression curves for different clay properties and for other assumed values of v, ε, c_0, CEC, SSA, and T as above. (d) Normalized compression curves for different dielectric pore fluids and for the same assumed values of v, ε, c_0, CEC, SSA, and T as above.

developed by following the aforementioned normalization and linearization procedure using the experimental data. Experimental compressibility data (Figure 3) as e/e_{50} *vs.* P are shown in Figure 8. The normalized data followed a unique relationship, in similar fashion to the theoretical data. The experimental data (Figure 3) were, therefore,

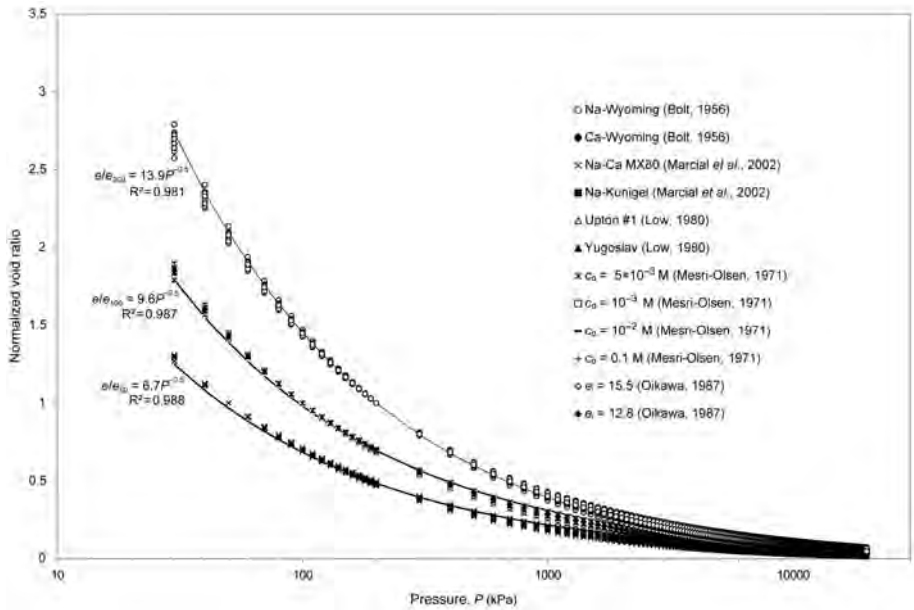

Figure 6. Normalized compression curves for all of the theoretical data presented in Figure 3.

re-plotted as normalized void ratio *vs.* $1/\sqrt{P}$ (Figure 9) using different normalization factors. The linear equations along with the regression coefficients are also presented in Figure 9. The theoretical equations and empirical relationships are compared in Table 2. The fitted empirical relationship was consistent with the predicted theoretical equations. The theoretical models based on GC theory were, therefore, accurate and reliable for predicting the compressibility data. As the pre-consolidation pressure is history dependent, a generalized predictive equation was developed in the following section to predict the compressibility data using any experimentally measured void ratio.

GENERALIZED PREDICTIVE EQUATION

The form of the predictive equation can be established from equations 6−8 as:

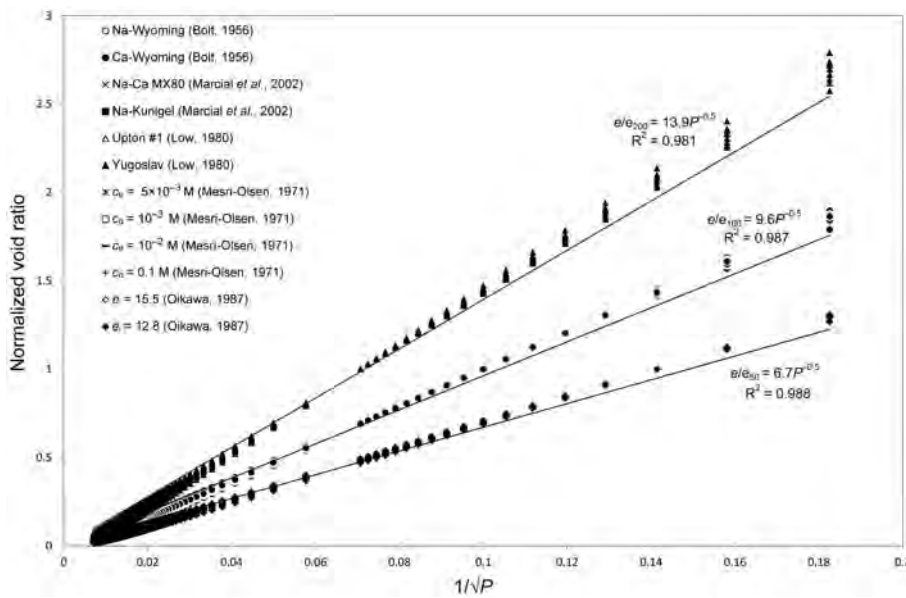

Figure 7. Normalized void ratio *vs.* $1/\sqrt{P}$ for all of the theoretical data presented in Figure 3.

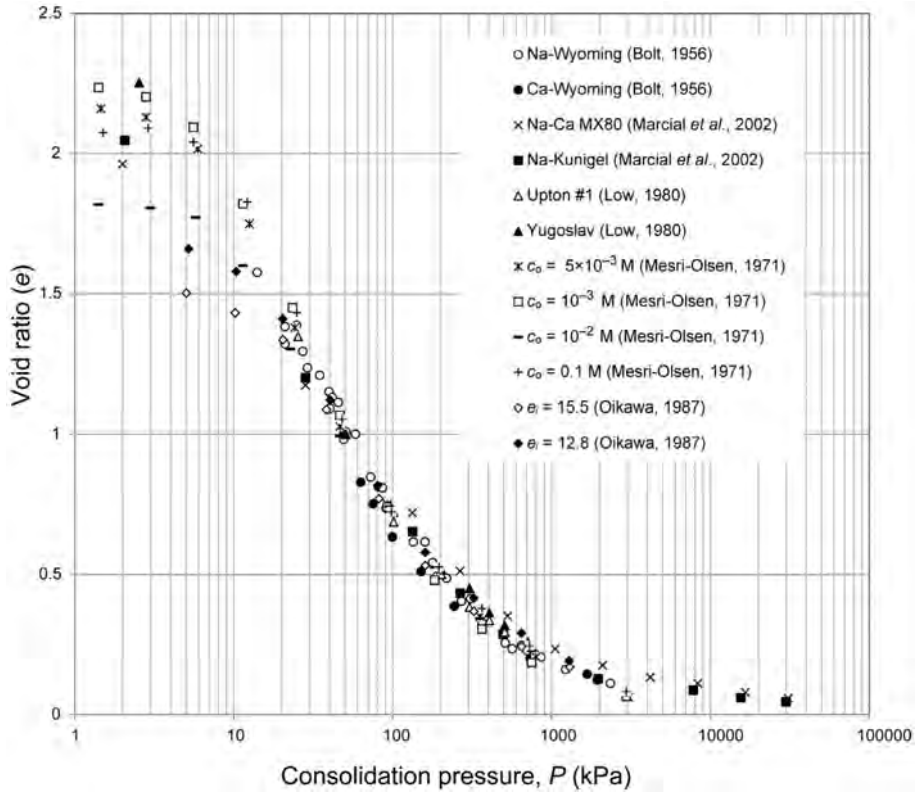

Figure 8. Normalized experimental compressibility data (presented in Figure 3) using e_{50}.

$$e\sqrt{P} = e_{Pi}K_i \quad (9)$$

where $e_{Pi=1,2,3...}$ are the normalizing factors that are void ratios under given consolidation pressures and $P_{i=1,2,3...}$

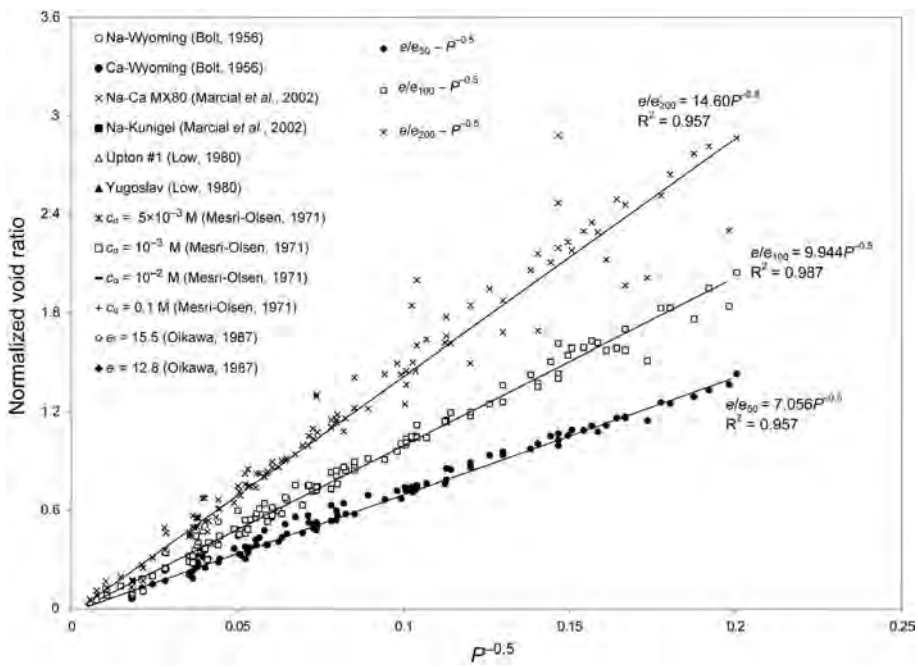

Figure 9. Linearized curves of experimental compressibility data given in Figure 3.

Table 2. Proportionality coefficients ($\sqrt{}$kPa) of the predictive equations.

Normalizing factor	Empirical (Figure 8)	Theoretical (equations 6–8)	Generalized formula (equation 9)
e_{10}	–	–	3.2
e_{25}	–	–	5.0
e_{50}	7.1	6.7	7.1
e_{100}	9.9	9.6	10.0
e_{200}	14.6	13.9	14.1

and $K_{i=1,2,3...}$ are the proportionality constants. Equation 9 must satisfy all of the data points, *i.e.* ($e_{Pi=1,2,3...}$, $P_{i=1,2,3...}$) on the $e-P$ curve. The proportionality constants should, therefore, be

$$K_{i=1,2,3...} = \sqrt{P_{i=1,2,3...}} \quad (10)$$

The generalized equation can be written as:

$$e = \frac{e_{P_i}\sqrt{P_i}}{\sqrt{P}} \quad (11)$$

which represents a complete compressibility curve. The complete compressibility curve can, therefore, be predicted using an experimentally measured void ratio under any given consolidation pressure. Substitution of 50 kPa and 100 kPa for P in equation 10 results in

$$e = \frac{7.1e_{50}}{\sqrt{P}} \quad (12)$$

and

$$e = \frac{10e_{100}}{\sqrt{P}} \quad (13)$$

which are the same equations derived above in equations 6 and 7, respectively. The proportionality coefficients of the predictive equations based on empirical and theoretical analyses are listed in Table 2. Comparison of all the available equations revealed that the equations derived here by empirical and theoretical analysis were particular solutions of the generalized equation given in equation 11.

EXPERIMENTAL VALIDATION

Theoretical compressibility data for various clays were predicted from the measured void ratio under a low consolidation pressure. The prediction required normalization pressure and the corresponding measured void ratio. The normalization pressures for different clays were obtained using the observed variations in the nature of the compressibility curve from concave to convex. Whether the chosen normalization pressure was beyond the pre-consolidation pressure was easily verified by obtaining predicted compressibility data from equation 11 using a few experimental data points near the pre-consolidation pressure. The predicted compressibility curves using different experimental data would match exactly with each other if the selected normalization data were beyond the pre-consolidation pressure. The normalization pressures varied from 25 to 133 kPa for different clays selected in this study. Void ratios corresponding to the normalization pressures were read from the data and the proportionality constants were computed using equation 10 for different clays. Theoretical data were then predicted using equation 11 to a maximum consolidation pressure ranging between 0.7 and 30 MPa for different plastic clays

The normalization data used for the prediction are shown as open circles (○) in all of the validation plots. The predicted data are compared with the experimental data (Figure 10a–c). The compressibility data for two Na-montmorillonite clays (Low, 1980) and Akita soft clays (Oikawa, 1987) were predicted theoretically and presented (Figure 10a,b). The predicted compressibility data were based on the measured void ratios at consolidation pressures of 101 kPa and 51 kPa for the Upton #1 (Low, 1980) and Yugoslav (Low, 1980) clays, respectively. The measured void-ratio data at consolidation pressures of 38 and 40 kPa were used to obtain theoretical data for the Akita clay. The predictions were extremely good for all of the clays considered. The generalized model proposed will therefore be very useful for predicting the compressibility data over a wide range of consolidation pressures for plastic clays using data from tests carried out up to pre-consolidation pressures.

Similar validation experiments were conducted on Na-Ca MX80 and Na-Kunigel bentonites (Marcial *et al.*, 2002) using the measured compressibility data at consolidation pressures of 133 kPa and 28 kPa, respectively (Figure 10c). The theoretical prediction was consistent with the measured data. The theoretical predictions were extremely good considering the several factors involved in laboratory measurements at high consolidation pressures. The proposed model is very simple considering that the prediction requires only a single measured void ratio beyond pre-consolidation pressure.

A statistical regression analysis of theoretical predictions on the experimental data was considered. Values of the coefficient of determination, R^2, of the theoretical fit to the experimental data from validation experiments (Figure 10a–10d) are presented (Table 3). The computed R^2 values are in the range 0.993–0.999 for different experiments. The validation experiments on different clays showed that the predicted compressibility

Table 3. Coefficient of determination values for the theoretical fit on the experimental data.

Source	Clay type	Figure number	R^2
Low (1980)	Upton #1	10a	0.995
	Yugoslav		0.994
Oikawa (1987)	Plastic clay, e_i = 15.5	10b	0.998
	Plastic clay, e_i = 12.8		0.999
Marcial *et al*. (2002)	Na-Ca MX80	10c	0.999
	Na-Kunigel		0.998

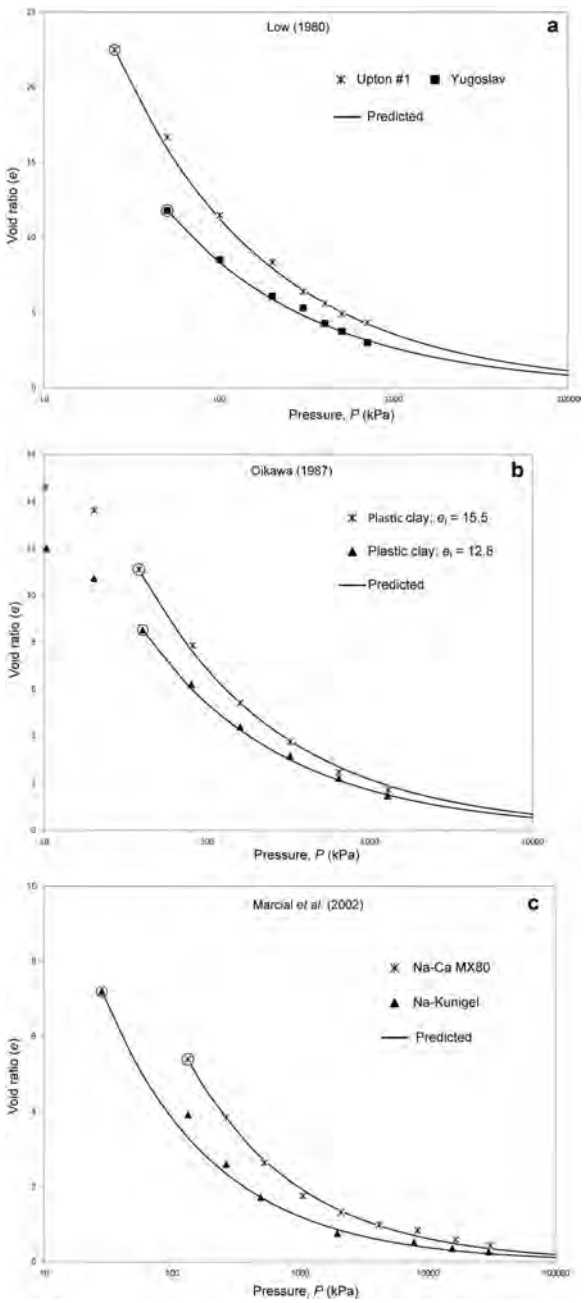

Figure 10. (a) Predicted theoretical compression curves using equation 11 along with the experimental data for Na-saturated montmorillonites. (b) Predicted theoretical compression curves for the experimental data from the Akita clays. (c) Predicted theoretical compression curves using equation 11 along with the experimental data for Na-Ca MX80 and Na-Kunigel.

data up to a maximum pressure range (0.7 to 30 MPa) for different plastic clays were in very good agreement with the experimental data.

CONCLUSIONS

Theoretical and experimental compressibility data were linearized using the normalization factor. The normalization factor contained information about the clay-surface and pore-fluid characteristics. A unique relationship was, therefore, investigated using the normalization procedure to represent the compressibility data which was independent of clay-water-electrolyte characteristics. The proposed equation was valid for all the plastic clays tested in the study when the normalization factor was greater than the pre-consolidation pressure. Through validation experiments on several compacted plastic clays, the equations have been proven able to predict the compressibility data over a wide range of consolidation pressures with the help of measured void ratios at pre-consolidation pressure. The proposed method did not require knowledge of the clay-surface or pore-fluid characteristics, or the computation of midway potentials to relate with clay-plate distances, unlike previous predictive models. The proposed method is useful for predicting *in situ* settlement behavior of plastic clays and for special applications in nuclear-waste repositories. Application of the proposed method, therefore, will reduce the cost of routine laboratory experimentation and the need to use specialized equipment for measuring compressibility data at high consolidation pressures.

ACKNOWLEDGMENTS

The authors are grateful for the support by the Department of Science and Technology (DST), Government of India through INSPIRE FACULTY AWARD [IFA12-ENG-41] to carry out the present study.

REFERENCES

Abdullah, W.S., Al-Zou'bi, M.S., and Alshibli, K.L. (1997) On the physicochemical aspects of compacted clay compressibility. *Canadian Geotechnical Journal*, **34**, 551–559.

Anandarajah, A. and Lu, N. (1991) Numerical study of the electrical double-layer repulsion between non-parallel clay particles of finite length. *International Journal for Numerical and Analytical Methods in Geomechanics*, **15**, 683–703.

Baille, W., Tripathy, S., and Schanz, T. (2010) Swelling pressures and one-dimensional compressibility behaviour of bentonite at large pressures. *Applied Clay Science*, **48**, 324–333.

Bharat, T.V. (2004) Simplified methods of evaluation of diffuse double layer parameters employed in geotechnical engineering. MSc (Eng) thesis, Indian Institute of Science, Bangalore, India, 102 pp.

Bharat, T.V., Sivapullaiah, P.V., and Allam, M.M. (2013) Novel procedure for the estimation of swelling pressures of compacted bentonites based on diffuse double layer theory. *Environmental Earth Sciences*, **70**, 303–314.

Bolt, G.H. (1956) Physico-chemical analysis of compressibility of pure clays. *Geotechnique*, **46**, 291–311.

Castellanos, E., Villar, M.V., Romero, E., Lioret, A., and Gens, A. (2008) Chemical impact on the hydro-mechanical behaviour of high-density FEBEX bentonite. *Physics and Chemistry of the Earth, Parts A/B/C*, **33**, S516–S526.

Chan, D.Y.C., Pashley, R.M., and Quirk, J.P. (1984) Surface potentials derived from co-ion exclusion. *Clays and Clay Minerals*, **32**, 131–138.

Chapman, L.A. (1913) Contribution to the theory of electrocapillarity. *Philosophical Magazine*, Series 6, **25**,475–481.

Frahm, J. and Diekmann, S. (1979) Numerical calculation of diffuse double layer properties for spherical colloidal particles by means of a modified non-linearized Poisson-Boltzmann equation. *Journal of Colloid and Interface Science*, **70**, 440–447.

Gouy, G. (1910) Sur la constitution de la charge électrique à la surface d'un électrolyte. *Journal de Physique*, *Théorique et Appliquée*, **4**, 457–468 (in French).

Hang, P.T. and Brindley, G.W. (1970) Methylene blue absorption by clay minerals. Determination of surface areas and cation exchange capacities. *Clays and Clay Minerals*, **18**, 203–212.

Low, P.F. (1980) The swelling of clay, II Montmorillonites. *Journal of the Soil Science Society of America*, **4**, 667–676.

Marcial, D., Delage, P., and Cui, Y.J. (2002) On the high stress compression of bentonites. *Canadian Geotechnical Journal*, **39**, 812–820.

McBride, M.B. (1997) A critique of diffuse double layer models applied to colloid and surface chemistry. *Clays and Clay Minerals*, **45**, 598–608.

Mesri, G. and Olsen, R.E. (1971) Consolidation characteristics of montmorillonite. *Géotechnique*, **21**, 341–352.

Mitchell, J.K. (1993) *Fundamentals of Soil Behavior*, 2nd edition. John Wiley and Sons, New York.

Oikawa, H. (1987) Compression curve of soft soils. *Soils and Foundations Journal*, **27**, 99–104.

Pusch, R. and Yong, R. (2006) *Microstructure of Smectite Clays and Engineering Performance*. Taylor and Francis, New York.

Robinson, G.R. and Allam, M.M. (1998) Effect of clay mineralogy on coefficient of consolidation. *Clays and Clay Minerals*, **46**, 596–600.

Santamarina, J.C., Klein K.A., Wang, Y.H., and Prencke, E. (2002) Specific surface: determination and relevance. *Canadian Geotechnical Journal*, **39**, 233–241.

Sellin, P. and Leupin, O.X. (2014) The use of clay as an engineered barrier in radioactive-waste management – a review. *Clays and Clay Minerals*, **61**, 477–498.

Sridharan, A. (2014) Soil clay mineralogy and physico-chemical mechanisms governing the fine-grained soil behaviour. *Indian Geotechnical Journal*, **44**, 371–399.

Sridharan, A. and Choudhury, D. (2002) Swelling pressure of sodium montmorillonites. *Géotechnique*, **52**, 459–462.

Sridharan, A. and Choudhury, D. (2008) Computation of hydraulic conductivity of montmorillonitic clays by diffuse double layer theory. *International Journal of Geotechnical Engineering*, **2**, 1–10.

Sridharan, A. and Jayadeva, M.S. (1982) Double layer theory and compressibility of clays. *Géotechnique*, **32**, 133–144.

Sridharan, A. and Rao, G.V. (1973) Mechanisms controlling volume change of saturated clays and the role of the effective stress concept. *Géotechnique*, **23**, 359–382.

Sridharan, A. and Satyamurty, P.V. (1996) Potential-distance relationships of clay-water systems considering the Stern theory. *Clays and Clay Minerals*, **44**, 479–484.

Sridharan, A., Rao, S.M., and Murthy, N.S. (1986) Compressibility behavior of homoionized bentonites. *Géotechnique*, **36**, 551–564.

Tripathy, S. and Schanz, T. (2007) Compressibility behaviour of clays at large pressures. *Canadian Geotechnical Journal*, **44**, 355–362.

Tripathy, S., Sridharan, A., and Schanz, T. (2004) Swelling pressures of compacted bentonites from diffuse double layer theory. *Canadian Geotechnical Journal*, **41**,437–450.

Tripathy, S., Bag, R., and Thomas, H.R. (2014) Effect of Stern-layer on the compressibility behaviour of bentonites. *Acta Geotechnica*, **9**, 1–13.

van Olphen, H. (1963) *An Introduction to Clay Colloid Chemistry*. Interscience, New York.

Verwey, E.J.W. and Overbeek, J.T.G. (1948) *Theory of the Stability of Lyophobic Colloids*. Elsevier, Amsterdam.

Yong, R., Taylor, L.O., and Warkentin, B.P. (1962) Swelling pressures of sodium montmorillonite at depressed temperatures. *Clays and Clay Minerals*, **11**, 268–281.

Yong, R.N. and Mohamed, A.M.O. (1992) A study of particle interaction energies in wetting of unsaturated expansive clays. *Canadian Geotechnical Journal*, **29**, 1060–1070.

Zheng, L., Samper, J., and Montenegro, L. (2011) A coupled THC model of the FEBEX in situ test with bentonite swelling and chemical and thermal osmosis. *Journal of Contaminant Hydrology*, **126**, 45–60.

(*Received 15 May 2014; revised 11 February 2015; Ms. 878; AE: William F. Jaynes*)

APPENDIX

Theoretical e vs. P relationship

The clay surface properties were assumed to be CEC = 100 meq/100 g and SSA = 800 m^2/g; pore-fluid parameters: $\nu = 1$, $c_0 = 10^{-4}$ M (*i.e.* the molar concentration which is equal to 10^{-4} N for monovalent electrolytes), $T = 298$ K, and $\varepsilon = 78.54$. The specific gravity of the clay was assumed to be 2.76. The procedure for computing the void ratio for a given consolidation pressure of 100 kPa was given in the following steps:

1. Scaled mid-plane potential (equation 1)

$$y_d = \text{arccosh}(1 + P/2c_0RT) = 6$$

2. Scaled surface potential, y_0, was computed by equating the value of $(dy/d\xi)_{x=0}$ in equations 1–2. Using equation 2,

$$\left(\frac{dy}{d\xi}\right)_{x=0} = -\frac{CEC}{SSA}\left(\frac{2513.6}{\sqrt{\varepsilon c_0 T}}\right) = -205.38.$$

The surface potential from equation 3 was

$$y_0 = \text{arccosh}(0.5\{[(dy/d\xi)_{x=0}]^2 + 2\cosh(y_d)\}) = 10.66$$

3. Scaled half-space distance was computed by the following integration

$$\kappa d = -\int_{y_0}^{y_d+\delta} (2\cosh(y) - 2\cosh(y_d))^{-1/2}$$

where δ is an infinitesimally small number (*i.e.* 10^{-5}) for numerical stability of the elliptic integral. The scaled distance

$$\kappa d = -\int_{10.66}^{6+\delta} (2\cosh(y) - 2\cosh(6))^{-1/2} dy = 0.146$$

4. The pore-fluid parameter (inverse of the 'Debye' length) was

$$\kappa = \sqrt{\frac{8\pi e'^2 \nu^2 c_0}{\varepsilon k_B T}} = 0.33 \times 10^6 \text{cm}^{-1} = 0.0033 \text{ Å}^{-1}$$

where c_0 = (normality $\times 10^{-3} \times$ Avogadro's number) ions/cm^3 (Van Olphen, 1963), $e' = 4.8 \times 10^{-10}$ esu, and $k_B T = 0.4 \times 10^{-13}$ ergs

5. The half-space distance was, therefore, $d = \kappa d/\kappa$ = 44.42 Å

6. Void ratio, therefore, was $e = d \times \rho_w \times G \times SSA = 9.81$

Clays and Clay Minerals, Vol. 63, No. 1, 43–50, 2015.

A CRITICAL APPRAISAL OF DEBYE LENGTH IN CLAY-ELECTROLYTE SYSTEMS

TADIKONDA VENKATA BHARAT[1,*] AND ASURI SRIDHARAN[2,†]

[1] Department of Civil Engineering, Indian Institute of Technology Guwahati, Guwahati – 781039, Assam, India
[2] Indian National Science Academy, New Delhi, India

Abstract—The equivalent diffuse double layer (DDL) thickness in clay-electrolyte systems is a very useful parameter for analyzing the engineering behavior of clays under different environmental conditions. The equivalent DDL thickness is generally assumed to be equal to the characteristic (Debye) length. The present work examined critically the applicability of characteristic length to define equivalent DDL thickness under various clay-surface and pore-fluid conditions. A critical analysis is presented of the changes in the equivalent DDL thickness and characteristic length under the influence of different clay-surface and electrolyte properties. The equivalent DDL thickness was found to be smaller than the characteristic length for a wide range of surface and pore-fluid parameters normally encountered in engineering practice. An accurate and simple power relationship was developed to predict the equivalent DDL thickness from the characteristic length, which is applicable to a wide range of clay-electrolyte systems.

Key Words—Clay-electrolyte System, Debye Length, Diffuse Double Layer.

INTRODUCTION

Plastic clays are of interest as buffer and backfill materials in toxic-waste and high-level nuclear-waste disposal facilities all over the world (JNCDI, 1999; Zheng *et al.*, 2011; Sellin and Leupin, 2014). Several natural and commercially available plastic clays (*e.g.* MX80, Febex, Montigel, and Kunigel V1) have been used widely in such applications. The application of DDL theory in the analysis of swelling pressures of compacted plastic clays is widely recognized (Tripathy *et al.*, 2004; Schanz and Tripathy, 2009; Baille *et al.*, 2010; Bharat *et al.*, 2013). The suitability of a given plastic clay for many engineering applications can be assessed easily and quickly using laboratory-based index tests, *e.g.* liquid limit and free swell ratio (Prakash and Sridharan, 2004). The relations between index and engineering properties are confirmed in the literature by analyzing the variations in the equivalent DDL thickness due to the changes in pore-fluid characteristics for given clay-electrolyte systems. The mechanisms by which equivalent DDL thickness influences the liquid limit (Sridharan *et al.*, 1986; Lambe and Whitman, 1979), sediment volume (Chen and Anadarajah, 1998; Sridharan and Prakash, 1999a), hydraulic conductivity (Fernandez and Quigley, 1985; Sridharan and Choudhury, 2002), and undrained shear strength (Sridharan and Prakash, 1999b) have been well documented. The relations between clay-surface properties and equivalent DDL thickness are also well known (Muhunthan, 1994). Such correlations can be useful in predicting indirectly the clay-surface properties from knowledge of index properties by analyzing the equivalent DDL thickness which is commonly estimated (Mitchell and Soga, 2005) as:

$$1/\kappa = \sqrt{\frac{\varepsilon KT}{8\pi e'^2 \nu^2 n}} \qquad (1)$$

where e' is the elementary electric charge (esu), ν is the valence of the ions, ε is the dielectric constant, K is thermal energy per ion in joules, T is the absolute temperature, and n is the molar concentration of the ions in bulk solution (mole/L). The quantity $1/\kappa$ (Å) is the characteristic length or 'Debye length' (Verwey and Overbeek, 1948). Equation 1 is used widely in many science and engineering applications as the equivalent DDL thickness (McBride, 1997; Poortinga *et al.*, 2002; Kitazumi *et al.*, 2013). There is no justification presented in the literature, however, to show that $1/\kappa$ is equal to the equivalent DDL thickness in non-interacting clay-electrolyte systems.

A critical appraisal of the characteristic length is provided here. The relevance of the equivalent DDL thickness was confirmed for different clay-surface and pore-fluid parameters. The condition at which the centroid distance deviates from the equivalent DDL thickness was investigated. The applicability of equivalent DDL thickness to determination of the theoretical water content of clays was analyzed qualitatively.

THEORY

The equivalent DDL thickness is considered as the distance of the centroid, d_c, of the electric potential distribution of clay-electrolyte systems, from the particle

* E-mail address of corresponding author:
tvb@iitg.ernet.in
† Formerly Professor of Civil Engineering, Indian Institute of Science, Bangalore
DOI: 10.1346/CCMN.2015.0630104

surface (Verwey and Overbeek, 1948) (Figure 1). The distribution of electric potential around a non-interacting and flat clay particle can be approximated using the following Poisson-Boltzmann equation (Mitchell and Soga, 2005):

$$\frac{d^2\phi}{dx^2} = \frac{8\pi n \upsilon e'}{\varepsilon} \sinh\left(\frac{\upsilon e' \phi}{KT}\right) \quad (2)$$

where x is the distance from the surface of the clay particle (Å) and ϕ is the electric potential (mV). The dimensionless form of equation 2 can be expressed as:

$$\frac{d^2y}{d\xi^2} = \sinh y \quad (3)$$

where $y = \upsilon e'\phi/KT$, $\xi = \kappa x$, and κ is the inverse of the characteristic length as defined in equation 1.

The following analytical solution to equation 3 for obtaining scaled, non-linear potential distribution can be obtained by considering the boundary conditions: $\xi = \infty$, $y = 0$, and $dy/d\zeta = 0$ for the first integration; $\zeta = 0$ and $y = z$ for the second integration (Verwey and Overbeek, 1948):

$$y = 2\ln\frac{\exp(\kappa x) + \tanh(z/4)}{\exp(\kappa x) - \tanh(z/4)} \quad (4)$$

where z is the scaled surface potential which is equal to $\upsilon e'\phi_0/KT$. The surface potential can be estimated using the following equation (van Olphen, 1977; Bharat *et al.*, 2013):

$$\phi_0 = 0.1725\frac{T}{\upsilon}\sinh^{-1}\left(\frac{1256.81P}{\sqrt{n\varepsilon T}}\right) \quad (5)$$

where ε is the dielectric constant, υ is the valence, and P is the ratio of cation exchange capacity (CEC) (meq/100 g) to specific surface area (SSA) in m^2/g. According to the original discussion by Verwey and Overbeek (1948), the Debye length was defined in the context of $z << 1$ which is identical to $\upsilon\phi_0 << 25$ mV. The electric potential decreases exponentially and reaches a $1/e$ fraction of its value at the clay surface for small values of z ($z << 1$). The centre of gravity of the space charge also coincides with the plane $x = 1$ in the case $z << 1$. The 'equivalent' DDL thickness is, therefore, considered to be equal to the characteristic length of Debye ($= 1/\kappa$) in this particular case. This Debye length, a constant appearing in the dimensionless form of potential distribution in equation 3, is now used widely (Achari *et al.*, 1999; Poortinga *et al.*, 2002; Kitazumi *et al.*, 2013) as an equivalent DDL thickness for various clay-electrolyte systems, without attempting to understand its validity (*i.e.* $\upsilon\phi_0 << 25$ mV). The important and hitherto unanswered question is, therefore, whether the aforementioned definition is valid for equivalent DDL thickness for different clay-electrolyte parameters as the electric potential in the clay-electrolyte system is heavily dependent on the properties of the pore fluid for a given clay. The present study investigates the applicability of the Debye-length definition by comparing the centroid distance of the electric potential distribution around the particles with the characteristic length for different surface and pore-fluid parameters.

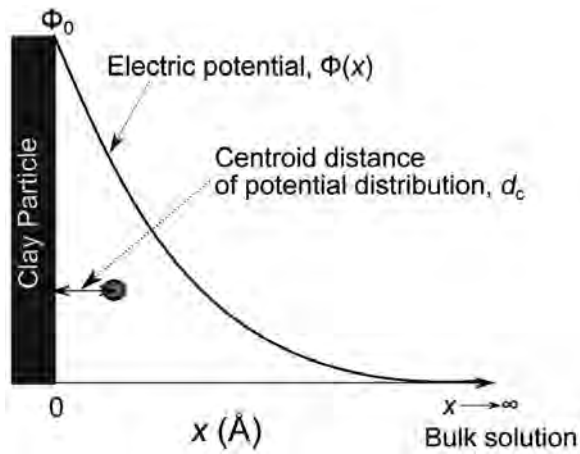

Figure 1. Conceptual diagram depicting the charge distribution around a clay particle.

CENTROID DISTANCE CALCULATION

The centroid distance of a given clay-electrolyte system can be computed by considering either the variation of ion concentration or electric potential. The distribution of average local concentration of both counter-ions and co-ions at equilibrium must be considered when the concentration distribution is used (van Olphen, 1977). The original definition of Debye length by Verwey and Overbeek (1948) as an equivalent of $1/\kappa$ is given in the context of electric potential distribution only. The concentration is, therefore, expressed as a function of average electric potential according to the Boltzmann's theorem for centroid-distance computation. The electrostatic potential distribution around a clay particle was obtained by substituting the computed scaled surface potential, z, and the characteristic length, $1/\kappa$, into equation 4 for known properties of the clay surface and pore fluids. The centroid distance is computed using the following integral equation:

$$d_c = \frac{\int_0^\infty xy(x)dx}{\int_0^\infty y(x)dx} \quad (6)$$

where the centroid distance is measured in ångstroms. The definite integral in equation 6 was solved numerically using the built-in '*quadv*' function in MATLAB© (2012) which uses the recursive adaptive Simpson quadrature method. A very large value was assigned

for the upper boundary in the definite integral which varied between 5000 and 100,000 Å for each set of pore-fluid parameters to analyze the convergence of the numerical solution.

RESULTS AND DISCUSSION

The results of equivalent DDL thickness were analyzed by plotting the variation of the characteristic length, $1/\kappa$, and the centroid distance, d_c, separately and also as a ratio of $1/\kappa d_c$ for different pore-fluid and clay-surface properties (Figures 2–6). Details of the pore-fluid and clay-surface properties used in the theoretical calculations are listed in Table 1. The variations in both the characteristic length and the centroid distance are presented for different electrolyte concentrations varying between 10^{-7} M and 10 M (Figure 2a). The surface potentials for concentrations between 10^{-6} M and

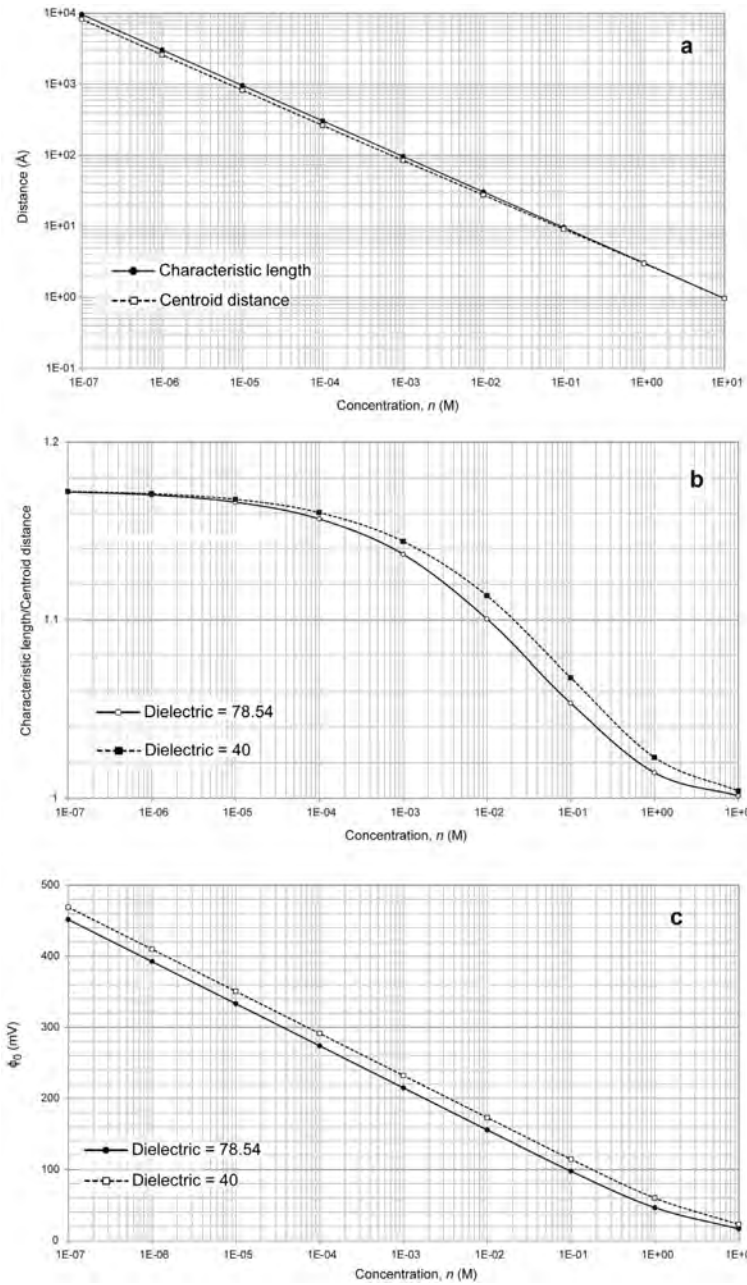

Figure 2. The influence of electrolyte concentration on (a) the characteristic length and centroid distance from the clay surface, (b) the ratio of characteristic length to the centroid distance for different dielectric media, and (c) surface potential for different dielectric media.

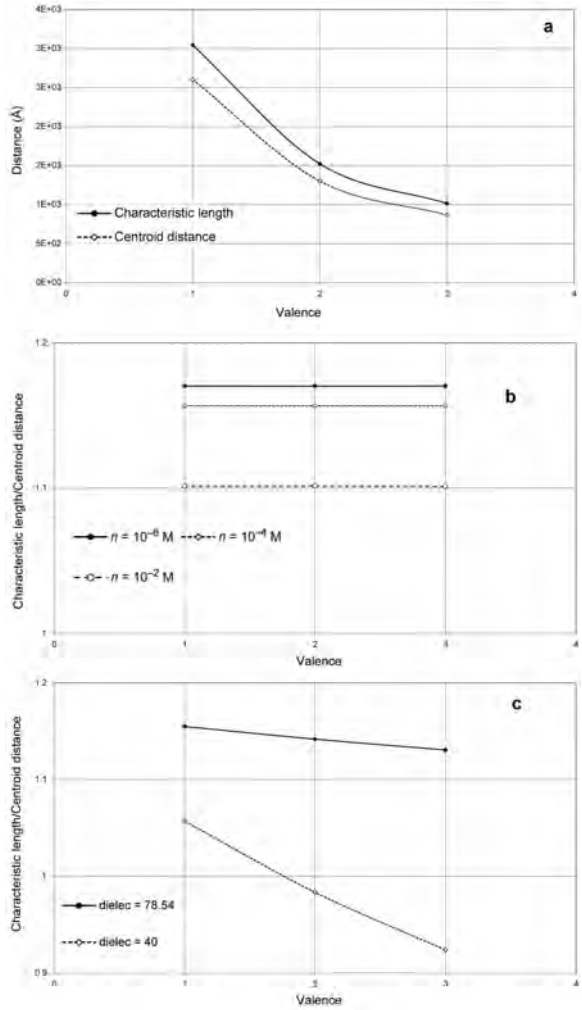

Figure 3. The influence of valence on (a) the characteristic length and centroid distance from the clay surface, (b) the ratio of characteristic length to the centroid distance for different electrolyte concentrations, and (c) the ratio of characteristic length to the centroid distance for different dielectric media.

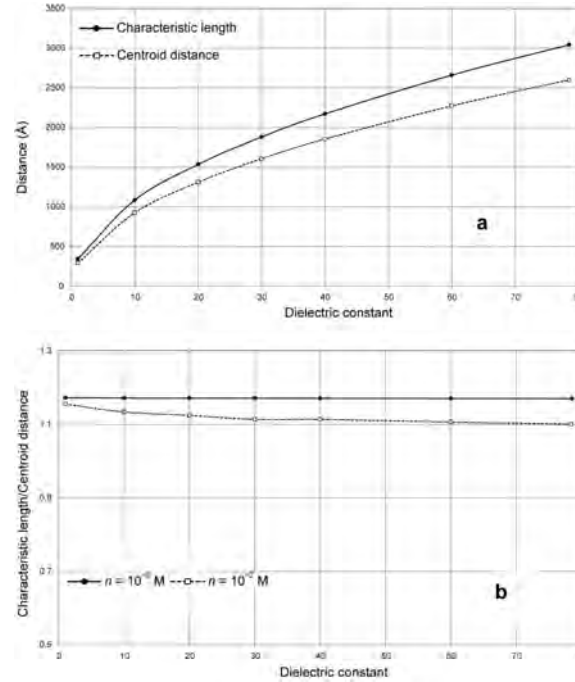

Figure 4. The influence of dielectric constant on (a) the characteristic length and centroid distance from the clay surface and (b) the ratio of characteristic length to the centroid distance for different electrolyte concentrations.

10^{-7} M were observed to be very large, *i.e.* $\phi_0 \geqslant$ 360 mV. The commonly encountered surface potentials of clay minerals in engineering applications may be <360 mV (van Olphen, 1977), but in many science disciplines the surface potentials of charged metal surfaces can be as high as 400 mV (Scruton and Blott, 1973). A wide range of electrolyte concentrations was, therefore, selected in the present study in order to analyze the conditions under which the characteristic length, $1/\kappa$, becomes equal to the equivalent DDL thickness, d_c. Both characteristic length and centroid

Table 1. Details of the electrolyte and clay-surface properties in the sensitivity analysis for DDL thickness calculations.

Figure #	Variables	Details of the clay surface and electrolyte parameters
2a	N	CEC = 100 meq/100 g, SSA = 800 m^2/g, v = 1, ε = 78.54, and T = 298 K
2b	n, ε	CEC = 100 meq/100 g, SSA = 800 m^2/g, v = 1, and T = 298 K
2c	n, ε	CEC = 100 meq/100 g, SSA = 800 m^2/g, v = 1, and T = 298 K
3a	V	CEC = 100 meq/100 g, SSA = 800 m^2/g, $n = 10^{-6}$ M, ε = 78.54, and T = 298 K
3b	n, ν	CEC = 100 meq/100g, SSA = 800 m^2/g, ε = 78.54, and T = 298 K
3c	ε, ν	CEC = 100 meq/100 g, SSA = 800 m^2/g, $n = 10^{-6}$ M, and T = 298 K
4a	ε	CEC = 100 meq/100g, SSA = 800 m^2/g, v = 1, ε = 78.54, and T = 298 K
4b	ε, n	CEC = 100 meq/100 g, SSA = 800 m^2/g, v = 1, and T = 298 K
5a	CEC/SSA	v = 1, ε = 78.54, $n = 10^{-6}$ M, and T = 298 K
5b	n, CEC/SSA	ε = 78.54, ν = 1, and T = 298 K
5c	n, CEC/SSA	ε = 78.54, ν = 1, and T = 298 K
6a	T	CEC = 100 meq/100 g, SSA = 800 m^2/g, v = 1, ε = 78.54, $n = 10^{-6}$ M, and T = 298 K
6b	T, n	CEC = 100 meq/100 g, SSA = 800 m^2/g, v = 1, ε = 78.54, $n = 10^{-6}$ M, and T = 298 K

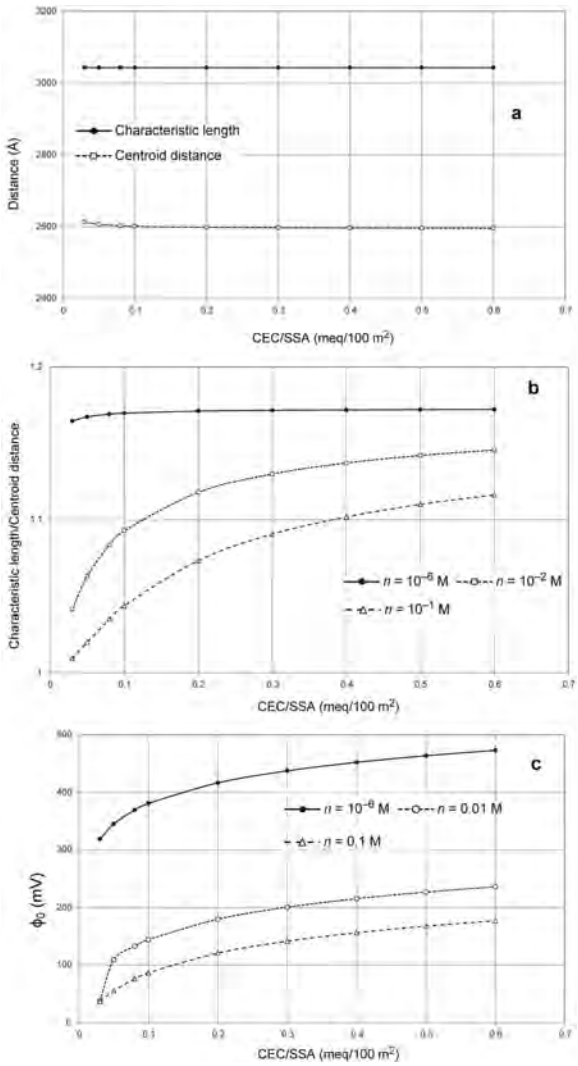

Figure 5. The influence of clay-surface properties on (a) the characteristic length and centroid distance from the clay surface, (b) the ratio of characteristic length to the centroid distance for different electrolyte concentrations, and (c) surface potential for different dielectric media.

distance decreased with the increase in the electrolyte concentration (Figure 2a).

The variation of $1/\kappa d_c$ with respect to the electrolyte concentration in the presence of two different dielectric media (Figure 2b) showed that the ratio $1/\kappa d_c$ changed non-linearly from 1.18 to 1 when the concentration increased from 10^{-7} to 10 M. This was because the surface potential decreased from 452 mV ($z \approx 18$) to 16 mV ($z < 1$) with the increase in the electrolyte concentration (Figure 2c). This observation was consistent with the definition of equivalent DDL thickness by van Olphen (1977). The classical definition of equivalent DDL thickness is, therefore, valid for electrolyte concentrations beyond 1 M where the surface potential dropped below 25 mV (Figure 2c).

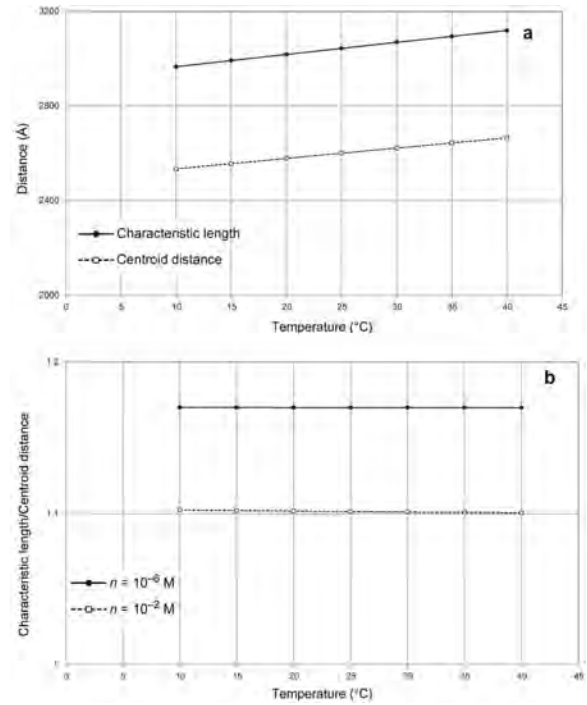

Figure 6. The influence of temperature on (a) the characteristic length and centroid distance from the clay surface and (b) the ratio of characteristic length to the centroid distance for different electrolyte concentrations.

The variation of the characteristic length and the centroid distance due to changes in the electrolyte valence was also analyzed (Figure 3a). A deviation of ~17% was observed between the characteristic length and the centroid distance in the presence of monovalent cations. The deviation decreased slightly in the presence of divalent and trivalent cations, even though both $1/\kappa$ and d_c decreased with increase in the cation valence. The influence of electrolyte concentration on the variation of $1/\kappa d_c$ was identified by analyzing the relationship of $1/\kappa d_c$ against the cation valence in the presence of three different electrolyte concentrations (Figure 3b). The ratio was consistent with the valence, but approached unity with increasing concentration. The influence of dielectric medium on the variation of $1/\kappa d_c$ was identified by analyzing the relationship of $1/\kappa d_c$ *vs*. the cation valence in the presence of two different dielectric media (Figure 3c). The ratio ($1/\kappa d_c$) was found to decrease with valence. The decreasing trend was more pronounced for smaller dielectric constants, *e.g.* the ratio approached unity when the surface potential dropped below 25 mV, which corresponds to the presence of a very large cationic valence and small dielectric constant.

The variations of the characteristic length and of the centroid distance were analyzed using different dielectric media (Figure 4a). The deviation of the characteristic length from the centroid distance was ~17% when water was used as the pore-fluid medium. The deviation

decreased slightly with decrease in the dielectric constant and approached zero at very small values of the dielectric constant. The influence of electrolyte concentration on the relationship between the ratio $1/\kappa d_c$ and the dielectric constant was confirmed (Figure 4b). The ratio $1/\kappa d_c$ remained nearly constant for different dielectric media. The ratio did become almost equal (~1.16) in the presence of a very low dielectric pore medium such as $\varepsilon = 1$. The ratio did not converge to unity (i.e. $\phi_0 > 25$ mV) for the entire range of dielectric constants (1−78.54) encountered in engineering applications.

The variations in the characteristic length and the centroid distance were plotted *vs*. the cation exchange capacity and surface area of the clay (CEC/SSA) (Figure 5a). The characteristic length was observed to be insensitive to CEC/SSA because the equation describing the characteristic length does not contain the surface properties of the clay. The clay-surface properties do influence the centroid distance, however. A significant deviation (~17%) of the characteristic length from the centroid distance was observed, therefore. The variation of the ratio $1/\kappa d_c$ with CEC/SSA in the presence of three different electrolyte concentrations (Figure 5b) showed that the ratio $1/\kappa d_c$ remained constant in the presence of low electrolyte concentrations, but the ratio approached unity for a small value of CEC/SSA, *i.e.* 0.03 meq/100 m^2 in the presence of high electrolyte concentrations. The effect of CEC/SSA on the ratio between centroid distance and characteristic length was found to be significant only at very high concentrations. The centroid distance decreased by 10% with increase in the ratio of CEC/SSA (for a change of CEC/SSA ratio from 0.03 to 0.6 meq/100 m^2) when n = 0.01 M. The distance decreased by just 0.7% with increase in CEC/SSA when $n = 10^{-6}$ M, however. This can be analyzed easily using equations 4−6. At very small ratios of CEC/SSA (*i.e.* <0.03) and under high electrolyte concentrations, the surface potential dropped below 25 mV and the centroid distance was equal to the characteristic length (Figure 5c).

The variation of the characteristic length and the centroid distance with temperature (Figure 6a) showed a deviation of 17% between characteristic length and centroid distance. The deviation remained nearly constant with increase in the temperature, even though both $1/\kappa$ and d_c increased with increase in the ambient temperature. The influence of electrolyte concentration on the variations of characteristic length and the centroid distance was confirmed by plotting the $1/\kappa d_c$ *vs*. the temperature in the presence of two different electrolyte concentrations (Figure 6b). The ratio $1/\kappa d_c$ remained constant for different temperatures, but decreased with increase in the electrolyte concentration.

The dependency of centroid distance on the characteristic length was very complex as many pore-fluid and clay-surface parameters influence the two thicknesses. The $1/\kappa$ value was observed to be consistently

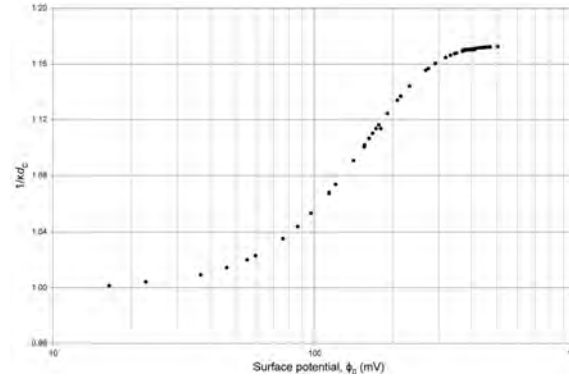

Figure 7. The variation of characteristic length to centroid distance ratio with surface potential.

greater than d_c, ~17% for different pore-fluid and clay-surface parameters. The values of characteristic length and equivalent DDL thickness converged only under uncharacteristic surface and pore-fluid conditions at which the surface potential dropped below 25 mV (Figure 7). The relationship followed an S curve and the maximum value of $1/\kappa d_c$ was ~1.18. The value became equal to unity with extreme pore-fluid and surface properties. The application of characteristic length as an equivalent DDL thickness is questionable, therefore.

A generalized relationship was confirmed between $1/\kappa$ and d_c for predicting the equivalent DDL thickness from the characteristic length by plotting the data of $1/\kappa$ and d_c obtained for the same pore-fluid and clay-surface parameters (Figure 8). The results followed a power relationship which can be expressed as:

$$d_c = 0.95(1/\kappa)^{0.986} \quad (7)$$

where both $1/\kappa$ and d_c were measured in ångstroms. The data fit was good with $R^2 = 0.999$. The accuracy of the proposed equation was verified by plotting the computed centroid distance (equation 6) and predicted distance (equation 7), which provided an accurate equivalent DDL thickness for all of the data (not shown here). The

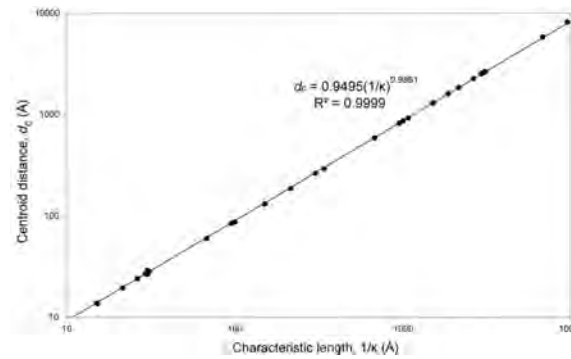

Figure 8. Power fit to the theoretical data between centroid distance and characteristic length for different pore-fluid characteristics.

proposed equation is applicable to a wide range of clay-surface and pore-fluid parameters that are commonly encountered in engineering and science applications.

The equivalent DDL thickness was observed to be the controlling parameter for analyzing the engineering behavior of clays. The influence of equivalent DDL thickness computation on the theoretical water content of the clay minerals was verified using the following equation (Lambe and Whitman, 1979):

$$w = t \times SSA \times \rho_w \quad (8)$$

where w is the gravimetric water content, t the equivalent DDL thickness, SSA is the specific surface area, and ρ_w the density of water. The equation represents the water content of a clay sample under stress-free conditions, *i.e.* an approximately 'liquid-limit' water content. The osmotic pressures due to the interacting diffuse double layers are negligibly small in the stress-free state. The theoretical water contents obtained by two different thicknesses (equations 1 and 6) were compared (Figure 9). An electrolyte concentration of 0.001 M, $\nu = 1$, and a specific surface area of 800 m^2/g were used for the theoretical calculation of water content of the clay minerals. The water-content values observed here were comparable to the water contents reported by Low (1980) for sodium bentonite clays at a consolidation pressure of 2.5 kPa. The computed water content from the two different thicknesses differed by ~13% for the reported clay surface and electrolyte properties. The characteristic length over-predicted the clay water contents and the deviation from the actual values increased even beyond 20% with the decrease in the electrolyte concentration. A detailed error analysis of variation in water contents with clay surface and electrolyte parameters, however, was outside the scope of this study. The water content of the clay is inter-related to the surface properties and many other engineering properties. The relevance of the proposed equation to the equivalent DDL thickness computation in understanding the engineering behavior of clays and for applications in other, allied disciplines is yet to be explored. The convention of the characteristic length being equivalent to DDL thickness is, nevertheless, invalid.

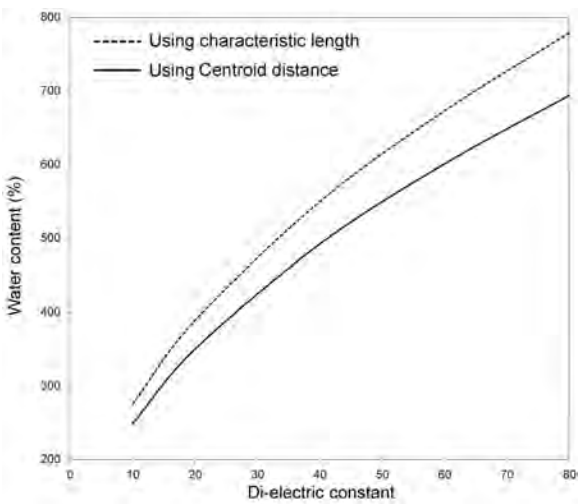

Figure 9. Comparison of the predicted clay-water contents in the presence of different dielectric media using characteristic length and centroid distance.

CONCLUSIONS

The equivalent DDL thickness was observed to be the centroid distance, d_c, of the electric potential distribution around the clay particle in a clay-electrolyte system. On the other hand, $1/\kappa$ was simply an 'equation constant' which appeared in double-layer theoretical equations. The suggestion in the literature that $1/\kappa = d_c$ was valid only at very high electrolyte concentrations (1 M) and for very small CEC/SSA ratios (<0.03 meq/100 m^2). Such extreme surface and pore-fluid conditions are encountered rarely in engineering and scientific applications. Use of characteristic length to represent the equivalent DDL thickness, therefore, is incorrect except within a very narrow zone of parameter space. The equivalent DDL thickness was smaller than the characteristic length (by as much as 17%) for a wide range of pore-fluid and surface properties. A new power relationship is proposed here to predict the equivalent DDL thickness from the characteristic length. This equation was not only valid over a wide range of pore-fluid and surface parameters, but was also capable of predicting the equivalent DDL thickness to a very high degree of accuracy. The proposed equation is useful for analyzing the influence of DDL thickness computation on many engineering parameters.

ACKNOWLEDGMENTS

The authors are grateful for the support by Department of Science and Technology (DST), the Government of India through INSPIRE FACULTY AWARD [IFA12-ENG-41] to carry out the present study.

REFERENCES

Achari, G., Joshi, R., Bentley, L., and Chatterji, S. (1999) Prediction of the hydraulic conductivity of clays using the electric double layer theory. *Canadian Geotechnical Journal*, **36**, 783–792.

Baille, W., Tripathy, S., and Schanz, T. (2010) Swelling pressures and one-dimensional compressibility behaviour of bentonite at large pressures. *Applied Clay Science*, **48**, 324–333.

Bharat, T.V., Sivapullaiah, P.V., and Allam, M.M. (2013) Novel procedure for the estimation of swelling pressures of compacted bentonites based on diffuse double layer theory. *Environmental Earth Sciences*, **70**, 303–314.

Chen, J. and Anadarajah, A. (1998) Influence of pore fluid composition on volume of sediments in kaolinite suspensions. *Clays and Clay Minerals*, **46**, 145–152.

Fernandez, F. and Quigley, R.M. (1985) Hydraulic conductivity of natural clays permeated with simple liquid hydrocarbons. *Canadian Geotechnical Journal*, **22**, 205–214.

Japan Nuclear Cycle Development Institute (JNCDI) (1999) H12: *Project to Establish the Scientific and Technical Basis for HLW Disposal in Japan: Supporting Report 2* (Respiratory Design and Engineering Technology), Japan Nuclear Cycle Development Institute, Tokyo.

Kitazumi, Y., Shirai, O., Yamamoto, M., and Kano, K. (2013) Numerical simulation of diffuse double layer around microporous electrodes based on the Poisson-Boltzmann equation. *Electrochimica Acta*, **112**, 171–175.

Lambe, W.T. and Whitman, R.V. (1979) *Soil Mechanics*. Wiley, New York.

Low, P.F. (1980) The swelling of clay. II. Montmorillonites. *Soil Science Society of America Journal*, **44**, 667–676.

MATLAB 8.0 and Statistics Toolbox 8.1 (2012) The MathWorks, Inc., Natick, Massachusetts, USA.

McBride, M.B. (1997) A critique of diffuse double layer models applied to colloid and surface chemistry. *Clays and Clay Minerals*, **45**, 598–608.

Mitchell, J.K. and Soga, K. (2005) *Fundamentals of Soil Behavior*. Wiley, New York.

Muhunthan, B. (1994) Liquid limit and surface area of clays. *Geotechnique*, **41**, 135–138.

Poortinga, A.B., Bos, R., Norde, W., and Busscher, H.J. (2002) Electric double layer interaction in bacterial adhesion to surfaces. *Surface Science Reports*, **47**, 1–32.

Prakash, K. and Sridharan, A. (2004) Free swell ratio and clay mineralogy of fine-grained soils. *Geotechnical Testing Journal*, **27**, 220–225.

Schanz, T. and Tripathy, S. (2009) Swelling pressure of a divalent rich bentonite: Diffuse double-layer theory revisited. *Water Resources Research*, **45**, 1–9.

Scruton, B. and Blott, B.H. (1973) A high resolution probe for scanning electrostatic potential profiles across surfaces. *Journal of Physics E: Scientific Instruments*, **6**, 472–474.

Sellin, P. and Leupin, O.X. (2014) The use of clay as an engineered barrier in radioactive-waste management – a review. *Clays and Clay Minerals*, **61**, 477–498.

Sridharan, A. and Prakash, K. (1999a) Influence of clay mineralogy and pore medium chemistry on clay sediment formation. *Canadian Geotechnical Journal*, **36**, 961–966.

Sridharan, A. and Prakash, K. (1999b) Mechanisms controlling the undrained shear strength behaviour of clays. *Canadian Geotechnical Journal*, **36**, 1030–1038.

Sridharan, A. and Choudhury, D. (2002) Swelling pressure of sodium montmorillonites. *Geotechnique*, **52**, 459–462.

Sridharan, A., Rao, S.M., and Murthy, N.S. (1986) Liquid limit of montmorillonite soils. *Geotechnical Testing Journal*, **19**, 156–164.

Tripathy, S., Sridharan, A., and Schanz, T. (2004) Swelling pressures of compacted bentonites from diffuse double layer theory. *Canadian Geotechnical Journal*, **41**, 437–450.

van Olphen, H. (1977) *An Introduction to Clay Colloid Chemistry*. Interscience, New York.

Verwey, E.J.W. and Overbeek, J.T.G. (1948) *Theory of the Stability of Lyophobic Colloids*. Elsevier, Amsterdam.

Zheng, L., Samper, J., and Montenegro, L. (2011) A coupled THC model of the FEBEX in situ test with bentonite swelling and chemical and thermal osmosis. *Journal of Contaminant Hydrology*, **126**, 45–60.

(*Received 14 April 2014; revised 27 February 2015; Ms. 864; AE: W.F. Jaynes*)

Clays and Clay Minerals, Vol. 63, No. 1, 51–68, 2015.

INTERACTION OF CORRODING IRON WITH BENTONITE IN THE ABM1 EXPERIMENT AT ÄSPÖ, SWEDEN: A MICROSCOPIC APPROACH

PAUL WERSIN*, ANDREAS JENNI, AND URS K. MÄDER

Institute of Geological Sciences, University of Bern, Baltzerstrasse 1+3, 3012 Bern, Switzerland

Abstract—Bentonite and iron metals are common materials proposed for use in deep-seated geological repositories for radioactive waste. The inevitable corrosion of iron leads to interaction processes with the clay which may affect the sealing properties of the bentonite backfill. The objective of the present study was to improve our understanding of this process by studying the interface between iron and compacted bentonite in a geological repository-type setting. Samples of MX-80 bentonite samples which had been exposed to an iron source and elevated temperatures (up to 115ºC) for 2.5 y in an *in situ* experiment (termed ABM1) at the Äspö Hard Rock Laboratory, Sweden, were investigated by microscopic means, including scanning electron microscopy, μ-Raman spectroscopy, spatially resolved X-ray diffraction, and X-ray fluorescence.

The corrosion process led to the formation of a ~100 μm thick corrosion layer containing siderite, magnetite, some goethite, and lepidocrocite mixed with the montmorillonitic clay. Most of the corroded Fe occurred within a 10 mm-thick clay layer adjacent to the corrosion layer. An average corrosion depth of the steel of 22−35 μm and an average Fe^{2+} diffusivity of $1-2\times10^{-13}$ m^2/s were estimated based on the properties of the Fe-enriched clay layer. In that layer, the corrosion-derived Fe occurred predominantly in the clay matrix. The nature of this Fe could not be identified. No indications of clay transformation or newly formed clay phases were found. A slight enrichment of Mg close to the Fe−clay contact was observed. The formation of anhydrite and gypsum, and the dissolution of some SiO_2 resulting from the temperature gradient in the *in situ* test, were also identified.

Key Words—Bentonite, Iron, *In Situ* Experiment, Interface.

INTRODUCTION

Bentonites are used for a variety of engineering and household applications (Carrado and Komadel, 2009; Christidis and Huff, 2009; Eisenhour and Brown, 2009; Gates *et al*., 2009; Güven, 2009; Williams *et al*., 2009). For example, compacted bentonite is envisaged as a backfill material in many geological-repository concepts for radioactive waste because of its favorable properties such as swelling capacity, plasticity, nanoporous structure, and retention capacity for radionuclides (*e.g.* NAGRA, 2002; SKB, 2011; Posiva, 2013). These properties may be compromised in geological-repository environments by interaction of the bentonite with reactive components such as cementitious or metallic materials. For example, in the Swiss high-level nuclear waste disposal concept, waste-containing steel canisters and compacted bentonite will be placed in horizontal deposition tunnels. Upon closure of the repository, the bentonite will be saturated by the ingress of natural porewater from the surrounding host rock. Concomitantly, the bentonite clay will experience elevated temperatures (up to ~130ºC) originating from the radioactive decay of the waste. During saturation, canister corrosion will be initiated, first under aerobic conditions, which will rapidly turn anaerobic by reaction of oxygen with the steel canister and with Fe-bearing minerals (*e.g.* pyrite) in the bentonite (Wersin *et al.*, 2004). From thermo-hydraulic calculations the saturation process is estimated to last for a period of decades up to a few hundreds of years (NAGRA, 2002). The anaerobic corrosion process, however, will last much longer (>10^5 y) and release dissolved mobile iron species which will react with the clay (Bradbury *et al.*, 2014). Details of the interaction of iron species released by corrosion and the clay are still not well understood. Several related processes affecting the barrier function of the bentonite backfill have been recognized, including: (1) local cementation of the bentonite by precipitation of Fe(II)/(III) oxides and hydroxides (Carlson *et al.*, 2007); (2) destabilization of the dioctahedral smectite structure (Lantenois *et al.*, 2005); (3) transformation of the montmorillonite to a non-swelling iron phyllosilicate, such as berthierine (Mosser-Ruck *et al.*, 2010); (4) dissolution of the montmorillonite during pH increase due to the iron-corrosion process (Marty *et al.*, 2010; Wersin and Birgersson, 2014); or even (5) direct interaction of H_2 with structural Fe in the smectite (Didier *et al.*, 2012).

A number of recent studies have looked at the effects of corroding iron on alteration in bentonite and in other clay materials; reviews of this topic include those by Wersin *et al.* (2007) and Bradbury *et al.* (2014). Most studies have examined idealized laboratory systems,

* E-mail address of corresponding author:
paul.wersin@geo.unibe.ch
DOI: 10.1346/CCMN.2015.0630105

tuned to enhance the effect of Fe−clay interaction. Smectite transformation to 1:1 phyllosilicates such as berthierine, cronstedtite, and odinite together with iron (oxyhydr)oxides has been observed in batch experiments at conditions of high liquid/solid ratios, high Fe/clay ratios, and low to moderate temperatures (20−90ºC) (Lantenois *et al.*, 2005; Perronnet *et al.*, 2008; Osacky *et al.*, 2010; Kumpulainen *et al.*, 2010; De Combarieu *et al.*, 2011; Lanson *et al.*, 2012; Jodin-Caumon *et al.*, 2010, 2012). At higher temperatures (100−300ºC), Fe-rich smectite (dioctahdral and trioctahedral) and/or chlorite minerals were identified (Guillaume *et al.*, 2003, 2004; Wilson *et al.*, 2006; Charpentier *et al.*, 2006; Mosser-Ruck *et al.*, 2010; Jodin-Caumon *et al.*, 2010, 2012), sometimes associated with newly formed zeolites (Wilson *et al.*, 2006; Charpentier *et al.*, 2006). Comparatively few studies have examined more realistic repository settings, *i.e.* low liquid/solid and Fe/clay ratios. Generally speaking, much less smectite alteration has been noted under such conditions, but magnetite (Papillon *et al.*, 2001; Carlson *et al.*, 2007; Martin *et al.*, 2008; Gaudin *et al.*, 2009), iron oxyhydroxides (Carlson *et al.*, 2007; Gaudin *et al.*, 2009), and siderite (Papillon *et al.*; 2001; Schlegel *et al.*, 2010) were observed as corrosion products. The experimental study of Martin *et al.* (2008) tested the corrosion behavior of iron in contact with compacted MX-80 bentonite and with a clayrock (Callovo-Oxfordian formation, Bure, France). In both cases, corrosion layers of magnetite and siderite were found, whereas only in the case of the clayrock was an intermediate Fe-, O-, Na-, and Si-containing layer (tentatively interpreted as consisting of phyllosilicates) observed. Later, the same research group (Schlegel *et al.*, 2010; 2014) identified the formation of a layer of Fe-rich 7 Å phyllosilicates in addition to chukanovite ($Fe_2CO_3(OH)_2$), magnetite, and siderite for Callovo-Oxfordian clayrock block samples exposed to an anaerobically corroding iron source.

In spite of the numerous investigations, understanding of the process of Fe−clay interaction remains rather sketchy, especially with respect to long-term behavior. Thus, uncertainties in predicting the stability of the bentonite backfill in contact with reactive metal iron components persist. In particular, this uncertainty is related to the mineralogical and hydraulic properties of the contact area between the iron and the clay (Johnson *et al.*, 2008).

The present study focuses on the contact area between a corroding iron source and compacted MX-80 bentonite that had been emplaced as highly compacted pellets in the ABM1 (Alternative Buffer Materials) *in situ* experiment at the Äspö Hard Rock Laboratory (Sweden) which was designed to simulate repository-like conditions. The objective is to obtain quantitative and qualitative process understanding of corrosion and Fe−bentonite interaction in a realistic repository setting with variable redox conditions and temperatures of ~100ºC. A secondary objective was to develop and optimize analytical methods to characterize the Fe−clay contact area which should be applied later to the samples from further ongoing, long-term *in situ* tests.

Two recent studies have analyzed different bentonite samples and the contact with the metal heater in the ABM1 test. Kaufhold *et al.* (2013) studied different precompacted bentonite block materials with standard techniques including X-ray diffraction (XRD), X-ray fluorescence (XRF), and Fourier-transform infrared (FTIR) spectroscopy, and focused on potential alterations in the bentonite materials. Some changes close to the contact with the steel were observed, including the accumulation of anhydrite and organic carbon and the dissolution of cristobalite in some samples, a general increase in iron, and the presence of siderite in one sample. In the second study, by Svensson and Hansen (2013), several bentonite materials, precompacted as blocks, from the ABM1 test and another *in situ* test were studied with XRD and X-ray absorption near edge structure spectroscopy (XANES) in terms of potential alterations and Fe(II)/Fe(III) distributions in the clay. The authors found that the Fe(II)/Fe(III) ratio had increased towards the steel heater, but otherwise only small changes had occurred, such as minor dissolution of cristabolite, an increase in the Mg content and a small shift in the 060 peak, indicative of trioctahedral smectite. The work presented here complements these studies, by looking at a specific type of granular compacted bentonite developed for backfilling in the Swiss repository concept (NAGRA, 2009). In contrast to the two other 'bulk-type' studies, the intact Fe interface was analyzed at a high spatial resolution with a microscopic approach including scanning electron microscopy-element dispersive spectroscopy (SEM/EDX) and spatially resolved μ-Raman spectroscopy. This enabled the authors to obtain quantitative information on the iron transfer from the corroding source to the clay.

EXPERIMENTAL AND ANALYTICAL METHODS

Characterization of the granular compacted bentonite material emplaced

The raw MX-80 bentonite with a mesh size of 16−200 (74−1000 μm) was purchased from the American Colloid Company (Sibelco Nordic Minerals, Cheshire, UK). The starting MX-80 and other bentonite materials in ABM1 were analyzed thoroughly with respect to their petrophysical, chemical, and mineralogical characteristics (Svensson *et al.*, 2011; NAGRA, 2011). The raw MX-80 was found to contain 80.5 ± 3.6 wt.% smectite, 6.0 ± 0.3 wt.% quartz, 0.6 ± 0.1 wt.% pyrite, 8.7 ± 0.6 wt.% feldspar, 2.6 ± 0.7 wt.% illite/muscovite, and 1.6 ± 0.7 wt.% calcite, as determined from quantitative XRD (Rietveld) analysis (NAGRA,

2011). In addition to those minerals, cristobalite and dolomite were identified from powder XRD data using a synchrotron X-ray source (Svensson *et al*., 2011). The cation exchange capacity (CEC) was determined by the Cu(II)-triethylenetetramine method (Meier and Kahr, 1999) to be 80.2 ± 4.0 meq/100 g (Svensson *et al.*, 2011). The chemical composition determined by XRF (Svensson *et al.*, 2011) is presented in the Results section below. The MX-80 bentonites from the same supplier were analyzed previously by Karnland *et al.* (2006) and yielded similar results. Using a Leco multiphase carbon analyzer, those authors also found the organic carbon content to be ~0.2–0.3 wt.%. The granular bentonite material, which was emplaced in the ABM1 borehole (see below), consisted of highly compacted MX-80 pellets with a very low moisture content (<5 wt.%) and a bimodal size distribution (Wollenberg and Schröder, 2006). The sealing properties and homogenization behavior during saturation under different temperature conditions had been studied previously using laboratory-scale samples (Karnland *et al.*, 2008).

The ABM1 test package, excavation, and on-site sampling

The ABM test is an internationally supported *in situ* experiment conducted by SKB (the Swedish Nuclear Fuel and Waste Management Co) in the Äspö Hard Rock Laboratory, Sweden. The main objective of ABM is to test the stability of different bentonites and other clay materials under adverse conditions, representative of the near-field of high-level radioactive waste repositories (Svensson *et al.*, 2011). Within the ABM test, three test

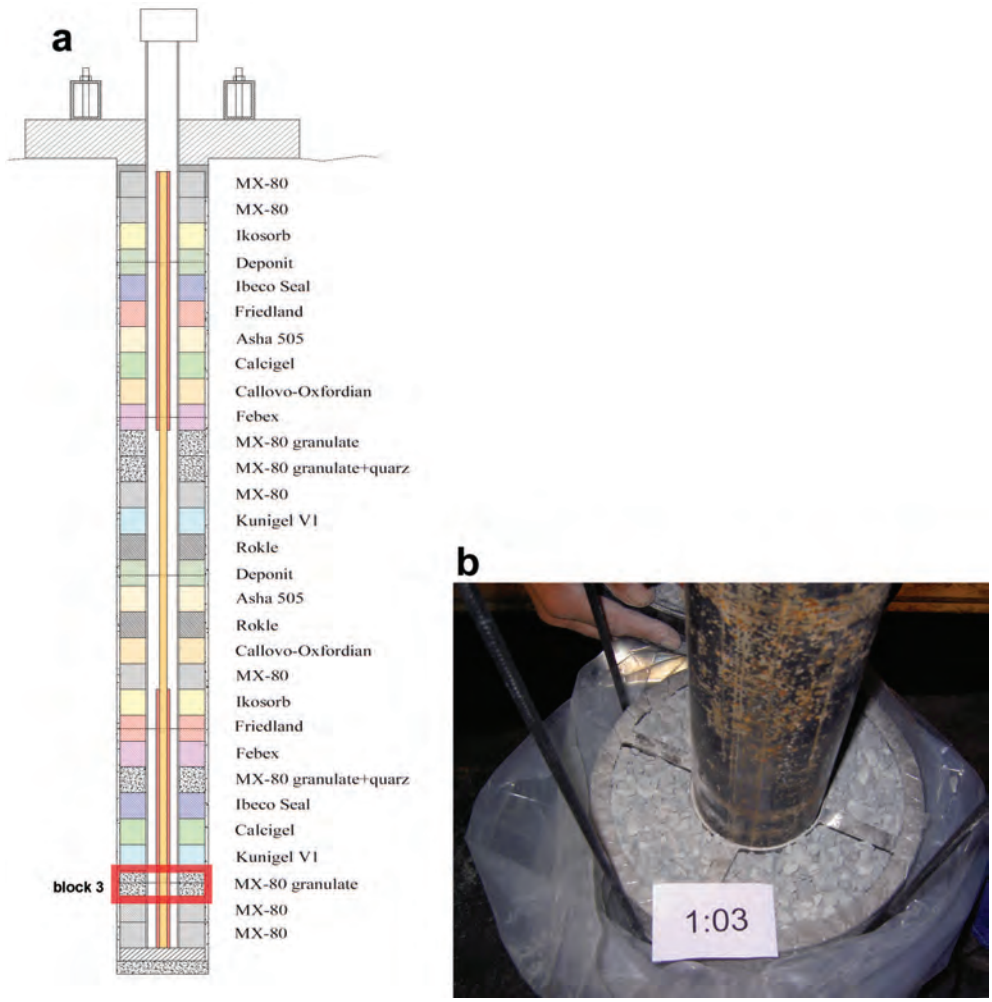

Figure 1. (a) Test layout of ABM1 showing the different clay materials stacked as blocks, each with a height of 100 mm in the borehole (diameter 300 mm). The total height of the stack is 3 m. In the center of the borehole is a steel tube which contains an electrical heating system. The position of block 3 marked in red. (b) Image of the pellet cage (block 3) during installation. The inner part of the cage is a metal ring (outer diameter = 108 mm); the outer cage is made of horizontal steel rings (outer diameter = 124 mm) and a steel fiber cloth. Steel bars on the top and the bottom of the cage reinforce its strength. The granular bentonite texture is clearly visible.

packages (ABM1, ABM2, and ABM3), consisting of various bentonite and other clay materials stacked upon each other as blocks, were placed in three boreholes and heated through a central steel tube (Figure 1a). The granular material of interest in this work was inserted in a prefabricated iron-based cage (Figure 1b) and emplaced as block 3. This circular cage was made of an inner cylindrical steel ring, steel frames, and fiber cloth wrapped around the cages (Figure 1b). The installation procedure was detailed by Eng *et al.* (2007). Descriptions of the experiment and its dismantling were presented by Svensson *et al.* (2011). Briefly, heating and wetting with artificial Äspö groundwater of the ABM1 test commenced on December 7, 2006. The bentonite materials were heated slowly and maximum temperatures were reached after ~1 y. Because of technical problems with the wetting system some variation in maximum temperatures occurred. The maximum heat output was generated for ~400 days as indicated by the temperature-monitoring data (Eng *et al*., 2007). Block 3 was exposed to maximum temperatures of ~115ºC closest to the central tube and to ~75ºC close to the rock contact. The moisture content was not monitored during the test, but was analyzed after overcoring (see the Results section); consequently, the saturation history is unknown.

The experiment was overcored after 881 days on May 5, 2009, 18 days after shutdown of the heating system. Subsequently, it was lifted up in one piece and sawn into segments which were placed in plasticized aluminum bags, evacuated, and welded. Then the bags were placed in air-tight barrels and transported to the laboratory at Clay Technology (Lund, Sweden) for detailed sampling. Sub-sampling was performed with a band saw (for bentonite and some steel bars of cages) and a mechanical hack saw (for the central steel tube and the bars of steel cages). Exposure to ambient air was minimized by covering surfaces with plastic foil and working swiftly. Cut-off sub-samples were immediately sealed in plasticized aluminum foil. Sharp edges of the steel cage (where present) were taped to protect the aluminum foil. Samples including iron components from the cage (inner cylinder, lateral bars, vertical bar) in block 3 were taken. Visual inspection of the granular bentonite material indicated no macroscopically discernible granular texture after the experiment.

The samples were transported to the University of Bern (Switzerland) and stored cool (~4ºC).

Petrophysical measurements

A sample of block 3 was cut with a band saw perpendicular to the borehole axis to prepare three subsamples: top, mid-height, and bottom of the block, each having a height of ~30 mm. From these, slices along radial profiles were cut for wet-density and water-content determinations along radial profiles for block 3. Higher-resolution 6-point radial profiles (radial length 15 mm) were determined at mid-height, and lower-resolution 3-point radial profiles (radial length 30 mm) were determined in parallel near the top and base (Table 1).

The water content (WC) was determined by heating the clay samples to 105ºC in a drying oven to constant weight (~48 h). The water content was calculated relative to the dry mass obtained at 105ºC. The error is estimated to be within 2%.

The wet density (ρ_{wet}) was measured in duplicate using the paraffin oil-displacement method. The error is estimated to be <±5%. The dry density (ρ_{dry}) was calculated from the WC and the ρ_{wet}. The porosity was calculated from the dry density and a grain density of 2.754 g/cm^3 (Table 1).

Table 1. Petrophysical data of block 3 after the *in situ* test.

	Radial distance from cage ring (cm)	Water content dry (wt.%)	Wet density (g/cm^3)	Dry density (g/cm^3)	Porosity* (vol.%)	Degree of saturation
Half-height	0–1.5	33.85	1.93	1.44	47.5	1.03
	1.5–3	35.49	1.90	1.40	49.2	1.01
	3–4.5	35.94	1.89	1.39	49.5	1.01
	4.5–6	36.23	1.88	1.38	49.8	1.00
	6–7.5	37.50	1.88	1.37	50.3	1.02
	7.5–9.2	38.43	1.87	1.35	51.0	1.02
Near the top	0–3	35.33	1.91	1.41	48.9	1.02
	3–6	37.32	1.87	1.36	50.4	1.01
	6–9	40.27	1.84	1.31	52.4	1.01
Near the base	0–3	33.48	1.93	1.45	47.4	1.02
	3–6	34.56	1.90	1.41	48.8	1.00
	6–9	37.44	1.89	1.37	50.1	1.03

* calc. assuming a grain density of 2.754 g/cm^3 (NAGRA, 2011).

Analysis of Fe–clay contact zone

Sample preparation. Using a band saw, the packaged sample was cut in half perpendicular to the cylindrical steel ring axis of the cage (Figure 2a). Inspection of the freshly exposed surfaces confirmed that the original granular texture had disappeared during the saturation and heating process. A subsample for microscopic analysis was extracted (Figure 2b), packed in plastic foil under slight vacuum, and inserted into liquid nitrogen for ~30 min. During this procedure a crack developed between the bentonite and the metal. Subsequently, the sample was freeze dried using a Leybold-Heraeus GT 2 instrument (Leybold-Heraeus, Hanau, Germany) at a vacuum of 0.1 Torr for 4 h. The sample, bentonite and metal, was removed from the apparatus and embedded immediately in epoxy resin under vacuum. About 1 week later, a polished section across the steel–clay interface was prepared without water contact. The surface was processed using grinding paper, oil-based diamond suspensions, and petroleum. The resulting polished section was subsequently stored in a desiccator until further microscopic analysis.

A further subsample was prepared for XRF and XRD analysis (see section below). For this purpose, ~2–3 mm-thick slices of the moist material were cut with a plastic cutting tool parallel to the metal contact. After each slicing step, aliquots were prepared quickly for XRD analysis (see section below) and the remaining sample block was repackaged under vacuum in plastic foil to minimize drying and oxidation. For XRF, aliquots were also prepared after each slicing step.

XRD analyses. The small amount of powder made it impossible to carry out a standard clay preparation (Atterberg separation, glycol treatment, drying, *etc*.). Instead, an aliquot of the moist clay material obtained from slicing of the clay sample (see above) was mounted quickly on a sample holder (front-loaded), the surface flattened with a glass slide, and inserted in a PANalytical X'Pert PRO X-ray diffractometer (PANalytical, Almelo, Netherlands). The samples were examined using CuKα radiation with a wavelength of 1.54 Å at 40 mA and 40 kV, and were scanned from 4 to 80º2θ using a step size of 0.0167º2θ and 10 s per step.

XRF analyses. Another aliquot of the moist clay material was dried to 105ºC in a drying oven for ~2 days. The dried samples were subsequently ground using a small tungsten carbide mill. Glass pellets were made by fusing a 1:10 mixture of sample powder and Li-tetraborate at 1100ºC. The XRF analyses of major elements were performed on a Philips PW 2400 spectrometer (Philips, Eindhoven, Netherlands) at the Department of Geosciences of the University of Fribourg, (Switzerland) and corrected with the internal Philips software *X40* on the basis of a set of international rock standards. Loss on ignition (LOI) was determined by mass difference before and after fusing.

SEM/EDX analyses. The uncoated sample surface was examined in a SEM (Zeiss EVO-50 XVP, Carl Zeiss Microscopy GmbH, Jena, Germany) equipped with an EDAX Sapphire light element detector in low-vacuum mode (10 Pa) with a beam acceleration of 20 kV, a sample current of 500 pA, and a working distance of 8.6 mm. The beam current was adjusted to yield a dead time of 20–30% for EDX analysis (energy dispersive spectroscopy). The EDX element maps with a resolution of 512 × 400 pixels were acquired using a dwell time of 200 µs/pixel, and frames were averaged for 8–12 h. Higher

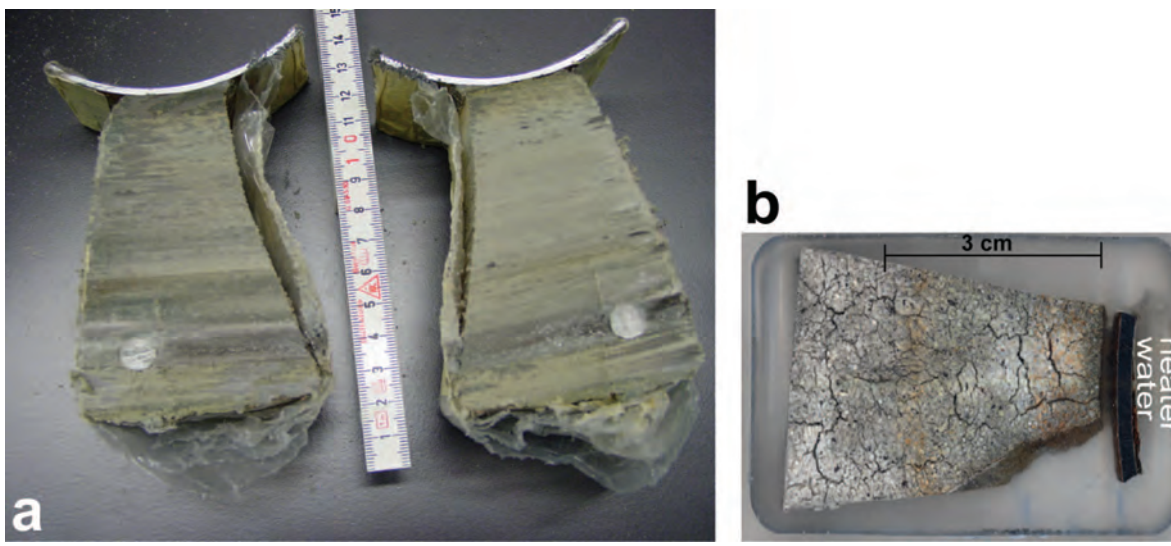

Figure 2. (a) Preparation of the clay sample with the steel contact. (b) Sample after freeze drying, resin impregnation, and polishing, as used for SEM and µ-Raman analysis.

resolution (1024 × 800 pixels), but shorter dwell time, was used to acquire backscattered electron (BE) images, which depict the average proton number at the beam location. The brightness and contrast of the maps were adjusted to reveal visible differences in gray values of important phases, often resulting in over- or undersaturation of phases of no interest. The EDX measurements were acquired for 60 s live time on spots or small homogenous areas, and analyzed semi-quantitatively without standardization using the EDAX Genesis software (Carl Zeiss Microscopy GmbH, Jena, Germany) with ZAF matrix correction. The data resulting in chemical profiles across the entire sample were acquired on a grid of 5 × 26 measurements, each scanning 1.52 mm × 1.19 mm for 3.13 min. The data for each of the five areas parallel to the steel interface were averaged; their range indicates the error of the method, assuming homogenous chemistry parallel to the interface. All detected elements heavier than fluorine were normalized to 100 wt.%, in contrast to methods with standards resulting in absolute compositions (*e.g.* electron microprobe). Errors in single EDX measurements were <2 wt.% in low-vacuum mode. In some measurements, oxygen was also quantified; much larger errors are expected in these cases.

μ-*Raman spectroscopy.* Raman spectroscopy was performed using a Jobin Yvon LabRAMHR800 (Horiba Jobin Yvon, Paris-Saclay, France) instrument, consisting of an Olympus BX41 confocal microscope (Olympus Corporation, Tokyo, Japan) coupled to an 800 mm focal-length spectrograph. An unattenuated He-Ne laser (20 mW, polarized 500:1) with an excitation wavelength of 632.817 nm (red) was focused on the sample surface and the Raman signal was collected in reflection mode. The sampled volume was a few μm^3 using a 100× objective. Acquisition times were 2 × 10 s and 2 × 120 s for iron phases and clay matrices, respectively. The spectra were recorded with the *Labspec* V4.14 software (Horiba Jobin Yvon, Paris-Saclay, France). Fluorescence caused an enormous background in spectra from the clay matrix, possibly as an artefact of the natural organic matter present in bentonite.

RESULTS

Petrophysical data for the clay

Data measured as a function of the radial distance from the steel ring located in the center of the cage include water contents and wet densities (Table 1). Profiles were located in the middle of block 3, as well as close to the interfaces with neighboring blocks above and below. Porosities, which were calculated from water contents and wet densities (see the Methods section), were found to be ~50 vol.%, but showed a slight decrease toward to the heater (at a distance of 0−1.5 cm) to ~48 vol.%. All samples were found to be fully saturated. The results indicate effective homogenization of the pellets during saturation and swelling.

XRD and XRF data

XRF. The chemical composition determined from XRF analyses at different distances from the Fe source were analyzed (Table 2). The Fe content increases toward the metal contact, from a distance of ~10 mm. This is in

Table 2. XRF analyses of samples at different distances from the Fe metal.

	Unit	C1/2	C3	C4	C5	C6	C7	C8	ref.
Max. dist. from iron	mm	4.5	6.0	10.0	18.5	25.5	31.5	36.5	MX-80*
SiO_2	wt.%	59.85	61.81	62.53	62.28	61.42	63.76	61.16	59.58
TiO_2	wt.%	0.16	0.16	0.16	0.16	0.16	0.17	0.16	0.2
Al_2O_3	wt.%	19.02	19.65	19.69	19.74	19.49	20.12	19.33	18.90
Fe_2O_3	wt.%	6.21	4.71	4.41	4.36	4.39	4.41	4.28	3.91
MnO	wt.%	0.02	0.01	n.d.	0.01	0.01	0.01	0.02	0.02
MgO	wt.%	2.42	2.38	2.36	2.35	2.37	2.40	2.37	2.56
CaO	wt.%	1.47	1.23	1.37	1.42	1.26	1.20	1.23	1.39
Na_2O	wt.%	2.23	2.36	2.22	2.29	2.20	2.18	2.15	1.95
K_2O	wt.%	0.55	0.59	0.57	0.58	0.54	0.54	0.55	0.6
P_2O_5	wt.%	0.06	0.06	0.06	0.06	0.06	0.06	0.06	0.09
LOI	wt.%	5.63	5.44	5.57	5.64	5.68	5.72	5.89	10.5
SUM	wt.%	97.61	98.40	98.93	98.90	97.57	100.57	97.20	99.70
Si/Al	at%/at%	2.67	2.67	2.69	2.68	2.67	2.69	2.68	2.67
Fe/Si	at%/at%	0.08	0.06	0.05	0.05	0.05	0.05	0.05	0.05
Fe/Al	at%/at%	0.21	0.15	0.14	0.14	0.14	0.14	0.14	0.13
Mg/Al	at%/at%	0.16	0.15	0.15	0.15	0.15	0.15	0.16	0.17
Ca/Na	at%/at%	0.37	0.29	0.34	0.34	0.32	0.30	0.32	0.39

* Reference MX-80 material from the American Colloid Company (Svensson *et al.*, 2011)

agreement with finer-resolution EDX data presented below, which also indicate an increase in Fe in the first 10 mm. The other elements show no trend with distance. Note that the slightly lower Si and Al concentrations close to the metal contact are explained entirely by the larger Fe content in these samples. The samples C4–C6, unaffected by the Fe enrichment, display similar elemental composition to the reference MX-80 analyzed by Svensson *et al.* (2011) (Table 2). The slight difference in Fe content is due to the different loss on ignition (LOI) values. This is indicated by the very similar elemental Fe/Si and Fe/Al ratios.

The Ca/Na elemental ratios derived for seven XRF samples are in the range 0.29–0.37, slightly lower than the value of 0.39 determined for the reference MX-80 (Svensson *et al.*, 2011). This suggests a slight enrichment of Na^+ on the clay exchanger which might have occurred by equilibration with the Na-rich Kunigel bentonite block adjacent to the sampled MX-80 (Figure 1). Equilibration of exchangeable cations between the different bentonite materials in the ABM1 test has been shown by Dohrmann *et al.* (2013). On the other hand, the Ca/Na ratios derived for XRF samples are generally smaller than those derived from EDX analyses (see section below). The reason for this difference is not clear; it may be a result of imprecise EDX data for the Na present in low concentrations, leading to Ca/Na ratios which are too high.

XRD. The material scraped off the steel surface facing the clay was analyzed by XRD. All reflections in the pattern can be explained by the presence of gypsum, smectite, quartz, and numerous iron phases (Figure 3). The presence of anhydrite is indicated by a small peak at the position of the major anhydrite reflection. Strong reflections of lepidocrocite, siderite, goethite, and magnetite reveal the presence of both Fe^{2+} and Fe^{3+}. The XRD results are in agreement with μ-Raman data collected from the water-side of the metal (see section below), in which all these iron phases were also identified, in addition to hematite. The presence of anhydrite and gypsum was also confirmed by the μ-Raman spectra (see section below).

The XRD patterns from the steel surface–clay were analyzed (Figure 4). Without specific clay preparation, investigation of the 001 reflection of smectite is inappropriate. In the present measurements, the peak position and form depend mainly on the hydration of the clay, which could not be controlled during sampling and measurement. The reflection at 62º is indicative of dioctahedral clays (060). The peak at 60º is assigned to quartz, but overlaps the position of a possible trioctahedral 060 reflection (*e.g.* saponite or biotite). Most of the other phases interpreted from these patterns (quartz, cristobalite, gypsum, feldspars, mica) are known to be present in the MX-80 reference (Svensson *et al.*, 2011, NAGRA, 2011). Small reflections indicate the presence of goethite in C5 and of anhydrite in C9.

None of the reflections indexed shows a clear gradient across the profile. Other variations in peak heights are not systematic and can be explained by large grain sizes compared to sample volume and crystallographic preferred orientations of large grains. The cristobalite peak, however, is smaller in C1–C3 than in C4–C9, and gypsum is absent from C8 and C9.

Mineral chemistry of the corrosion layers

The metal–water side. The metal surface opposite the metal–clay interface (Figure 2b) was in contact with water circulating between central heater and the metal ring of the cage. The reason for studying this interface was to obtain insight into the corrosion process and compare the data with those obtained from the metal–clay side. Moreover, the identification of iron corrosion products by μ-Raman is more straightforward than on the opposite metal–clay side because the latter spectra were found to be affected by strong fluorescence. Raman spectra of the clay-free corrosion layer facilitated the subsequent Raman analysis of the contact area between the metal and the clay.

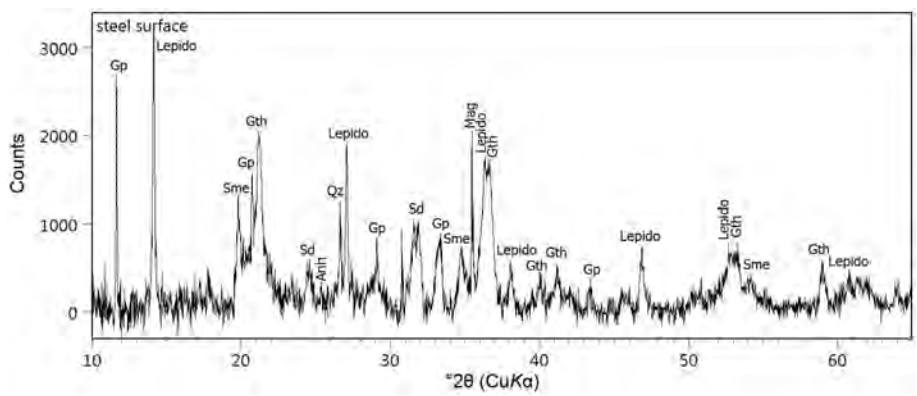

Figure 3. XRD pattern of the material scraped off the steel surface (Gp: gypsum, Lepido: lepidocrocite, Sme: smectite, Gth: goethite, Sd: siderite, Anh: anhydrite, Qz: quartz, Mag: magnetite; abbreviations after Whitney and Evans, 2010).

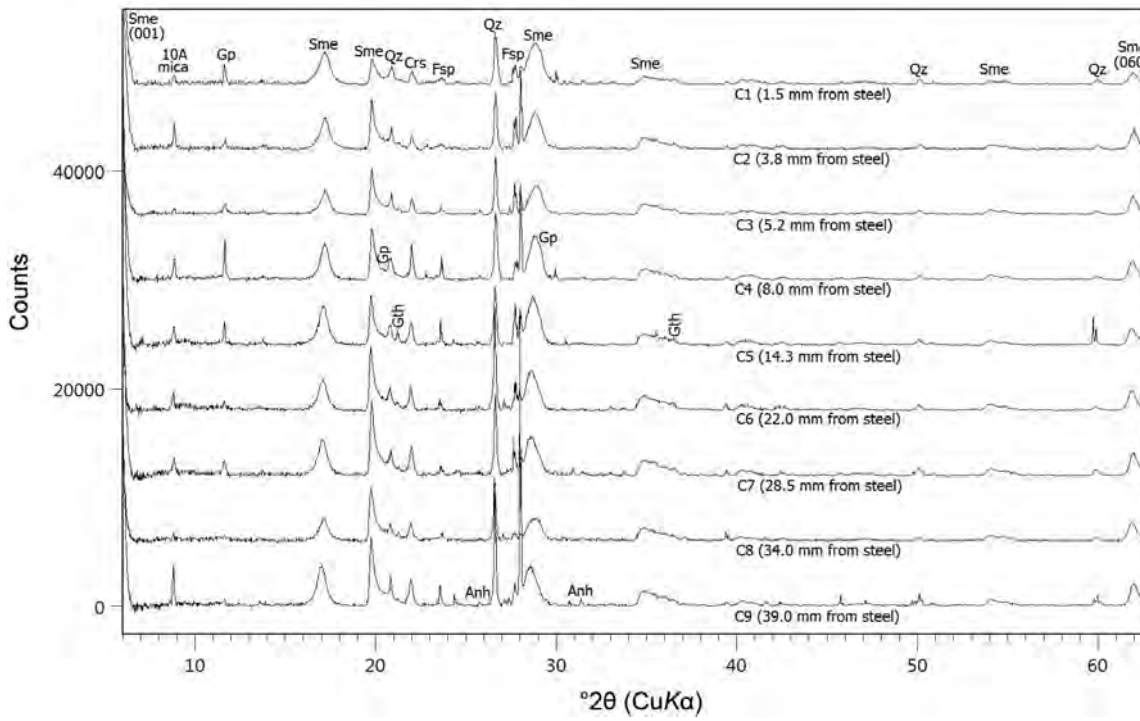

Figure 4. XRD patterns of the profile from the steel into the bentonite. The distances of the midpoints of sampled layers from the steel surface are indicated; counts are given for the lowest pattern C9. Consecutive patterns are shifted up by 6000 counts (Sme: smectite, Gp: gypsum, Qz: quartz, Crs: cristobalite, Fsp: feldspar, Anh: anhydrite, Gth: goethite).

The backscattered electron image of the metal–water contact area exhibits an irregularly shaped surface layer ~40–50 μm thick, with gradually increasing porosity (Figure 5). The patchy texture next to the bright metal surface is caused by different shades of variably sized grains. Adjacent to the interface, there is an aggregation of lighter-gray material of variable thickness (<5–20 μm) (Figure 5, lower right). Further away,

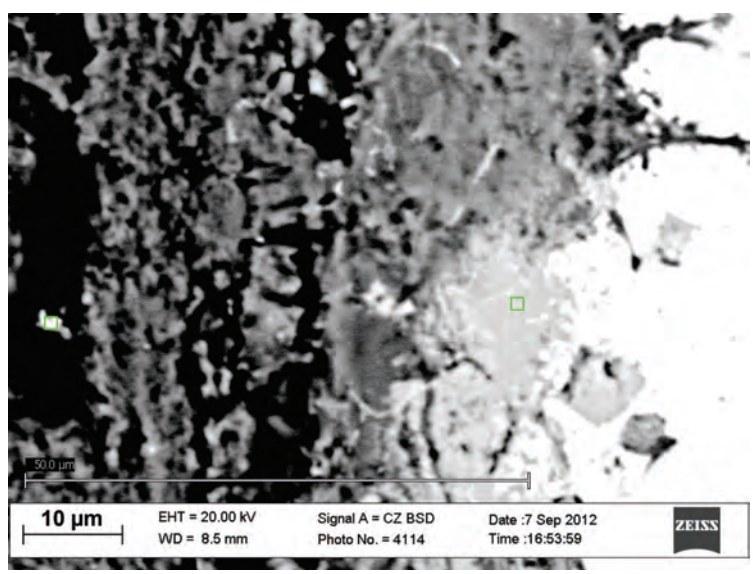

Figure 5. BSE-SEM image of a section across the metal and its corrosion layer facing the waterside; the metal surface is visible as a white area on right side – it has irregular contact with the corrosion layer to the left. The green square close to the metal represents the measurement area of the Raman spectrum corresponding to Figure 6a, green square further away from metal represents the measurement area of the Raman spectrum corresponding to Figure 6b.

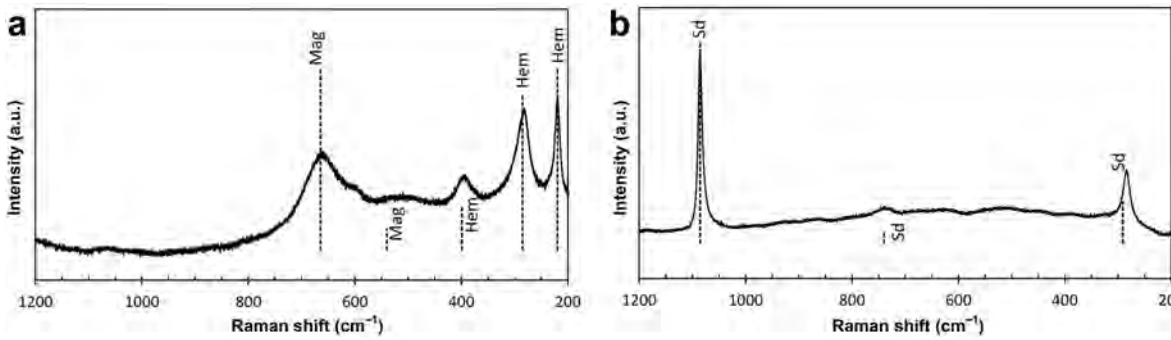

Figure 6. Selected Raman spectra of corrosion products obtained at the metal–water side of the corrosion layer: (a) spectrum taken 5 μm from the metal contact; (b) spectrum taken 50 μm from the metal contact. The dashed lines show reference-band positions and relative heights – Mag: magnetite, Hem: hematite, Sd: siderite (abbreviations after Whitney and Evans, 2010).

darker and more porous material dominates which is interspersed with brighter aggregates.

The different gray values of these materials reflect their different chemical composition (mean atomic number), which is dominated by Fe and O as indicated by semi-quantitative EDX analysis. The brighter material (Figure 5) was found to have a distinctly higher atomic Fe/O ratio than the darker one (data not shown). Trace amounts of Si and S were also detected. This indicates different Fe corrosion products, which was confirmed by μ-Raman spectroscopy. The light gray material close to the Fe surface (Figure 5) was found to consist of magnetite and, to a minor extent, hematite (Figure 6a, marked with a green square in Figure 5). Further away from the iron source, siderite was identified as the main Fe phase (Figure 6b). Some goethite and lepidocrocite (spectra not shown) were also observed. Siderite could also be identified by complementary SEM/EDX analysis. Well crystallized siderite grains were formed towards the outer contact of the corrosion layer (see bright grains at the right of Figure 5 marked with a green square).

The metal–clay side. The metal surface layer facing the clay has a different texture and denser habit (Figure 7): aggregates of bright and dark particles (diameter ~5–30 μm) form an irregular mesh. Chemically, the material was found to be composed of the elements Fe, Si, Al, Ca, Mg, and Na (besides O and C) with variable S contents as indicated by EDX spot analyses. The Fe contents revealed important variations with distance from the metal surface (Figure 8a), which are visible in backscattered electron images as variations in the brightness of the particles, with greater amounts of Fe associated with brighter particles. The Fe and Si profiles (shown as elemental ratios) from spot analyses indicate

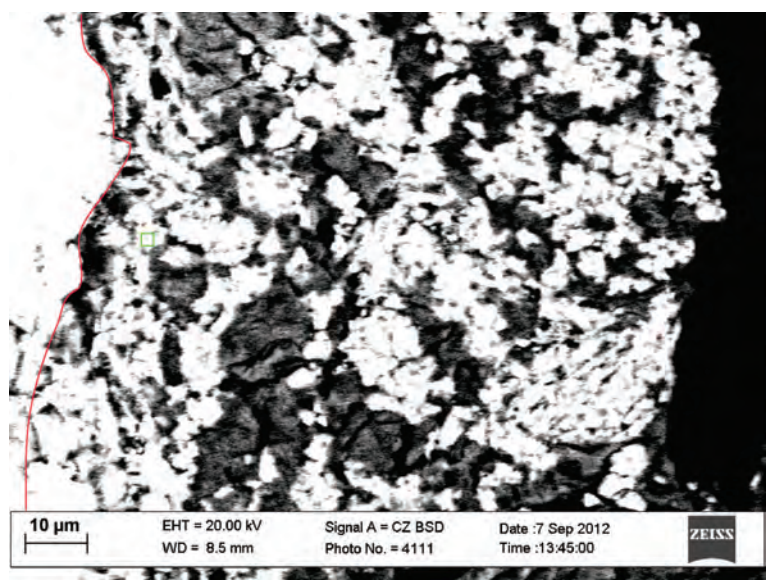

Figure 7. BSE-SEM image of a section across the metal and corrosion layer facing the clay. The red line delineates the contact between the metal and the corrosion layer. The black area on the right corresponds to a resin-filled gap between the metal and the clay formed during freeze drying. The green square represents the measurement area of the Raman spectrum shown in Figure 9.

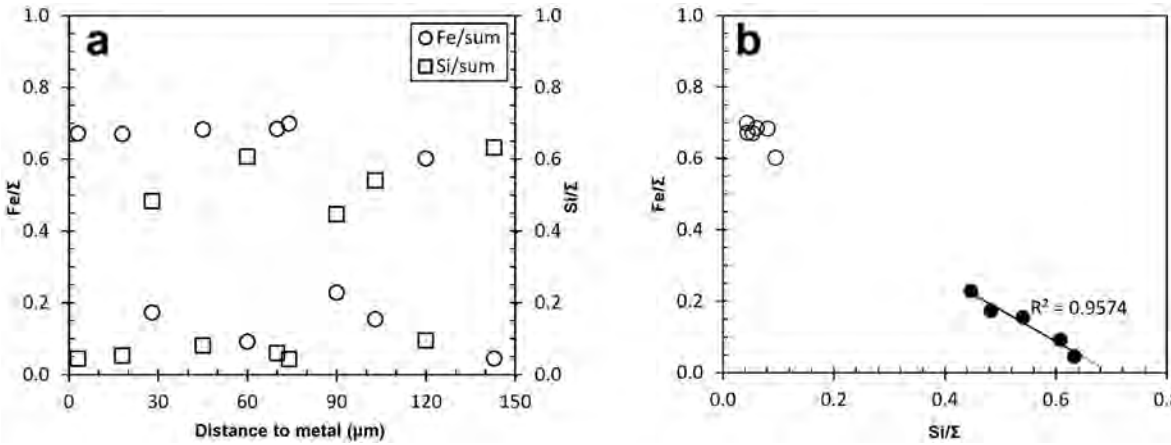

Figure 8. (a) Fe and Si *vs*. distance to metal in the corrosion layer (shown as atomic ratios Fe/(Si+Al+Mg+Na+K+Fe+S+Cl) (or Fe/Σ) and Si/(Si+Al+Mg+Na+K+Fe+S+Cl) (or Si/Σ). (b) Fe/Σ *vs*. Si/Σ. Open symbols: spots with high Fe/Si, closed symbols: spots with low Fe/Si.

two distinct groups of grains or grain aggregates: one with high Fe and low Si (bright grains) and one with low Fe and high Si (dark grains). The Fe and Si contents for the latter group are anti-correlated (Figure 8b) and this trend extends further into the Fe-enriched clay (data not shown).

Analysis by µ-Raman spectroscopy turned out to be more challenging on the clay side because of strong fluorescence radiation and fuzzier spectra. Nevertheless, siderite and, to a lesser extent, magnetite could be identified in the light gray particles (green square marked in Figure 7 corresponds to the Raman spectrum in Figure 9). The large fluorescence acquired from the dark gray particles indicates the presence of a clay matrix.

Mineral chemistry in the clay beyond the corrosion layer

Elemental mapping and phase identification. Imaging by SEM revealed the dense homogeneous texture of the clay and confirmed the macroscopic observation that the original granular texture had been destroyed during the course of the *in situ* experiment. Note that the cracks observed (Figures 2b, 10) were formed during drying of the SEM sample. The elemental composition of the clay close to the metal contact but beyond the corrosion layer was analyzed by BSE-SEM imaging and qualitative elemental EDX maps (Figure 10). The black rim on the right hand side of each image represents the gap (induced by sample preparation) between the metal (including the corrosion layer) and the clay. The mapping thus covers the first 4 mm from the contact. Close to the contact, the concomitant enrichment of Ca and S points to the presence of anhydrite or gypsum. µ-Raman analysis of the same area indicates anhydrite as predominant and gypsum as a secondary phase (data not shown). For Si and Al, no trend with distance from the iron source was observed within the first 4 mm (Figure 10) and also beyond this distance as detailed below. The bright spots (~10−50 µm in size) noted on the Si map are probably SiO_2 particles. For Mg also, no trend is visible in the mapping, but a slight trend was noted from the quantitative area measurements (see below).

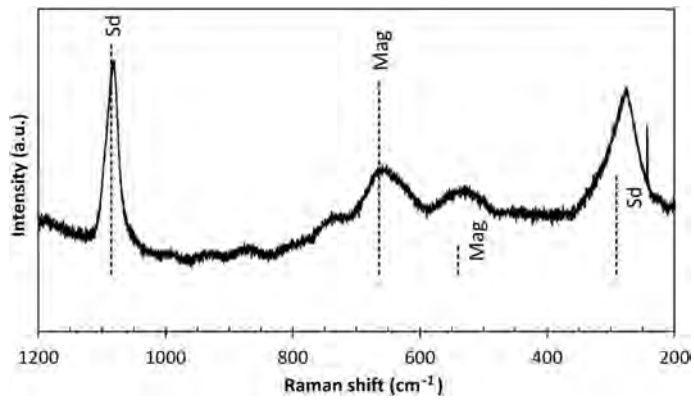

Figure 9. Selected µ-Raman spectrum in the 100 µm layer contacting the Fe surface. The dashed lines refer to the main reference-band positions and relative heights of siderite (Sd) and magnetite (Mag).

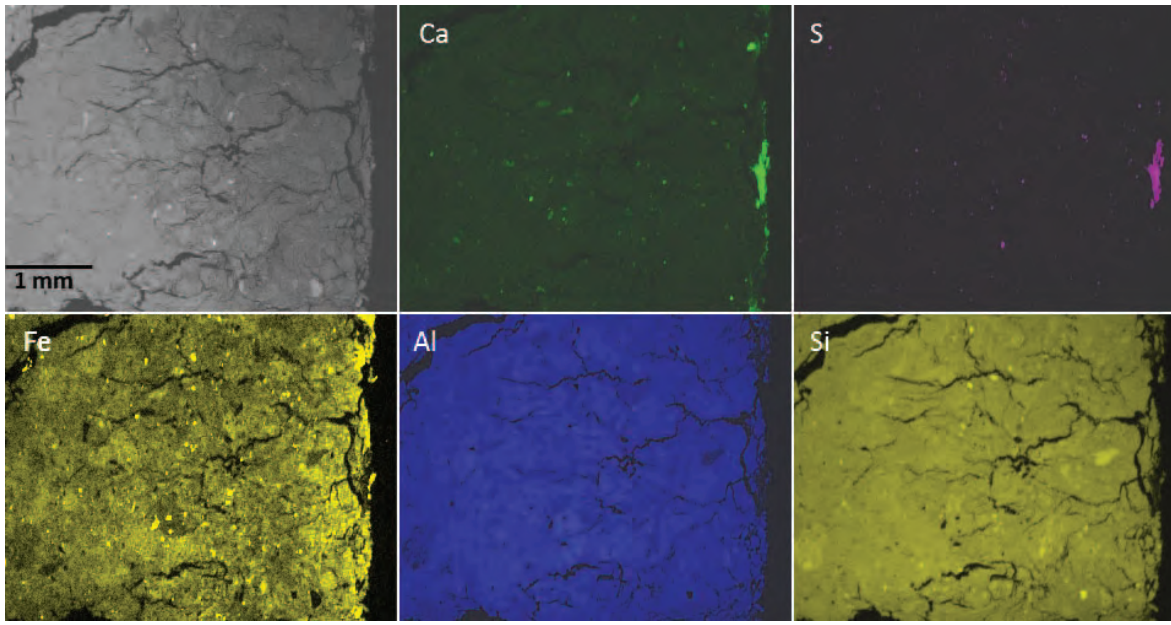

Figure 10. BSE-SEM image (top left) and EDX element maps of the clay sample close to the metal contact. Light colors represent high, dark colors low elemental concentrations. The contact gap/clay is on right hand side (see text). For Fe, higher concentrations are visible in the first 1 mm, next to the gap/clay contact.

Iron is also enriched in the clay matrix within the first 1 mm (right hand side of Figure 10). Due to the surface preparation and microscopic method chosen, this matrix appears to be structurally and chemically homogeneous and cannot be resolved further, *e.g.* it is possible that neo-formed iron phases cannot be localized. Adjacent to the gap, Fe-rich particles are observed (Figure 10). Most of the particles were found to be siderite as indicated by Ca levels which had concomitant increases, and are therefore considered to be part of the corrosion layer described above. Fe-rich particles further away from that gap are interpreted as pre-existing; according to quantitative image analysis they occupy only 0.4% of the area. Some of these particles were found to be enriched in sulfur, suggesting pyrite. A few bright particles in the Fe map are enriched in K, Si, and Al (but not in S), which might represent illite, present as an accessory mineral in the original MX-80 material (see the Methods section). Others, which are more abundant at the gap/clay contact, show no enrichment in K, but contain some Si, Al, Ca, and Mg (data not shown). Because of their small size it was not possible to identify the mineralogy of these particles.

Quantitative EDX profiles. The relationships between the elements were further studied by quantitative area measurements (see the Methods section). These were conducted on a fairly large area of 39.5 mm × 5.9 mm facing the metal contact. The total area was divided into five rows and 26 columns, thus corresponding to 130 cells. Each cell corresponds to one EDX area measurement. Averaged EDX analyses of five individual measurements (referred to as 'area measurements' below) were calculated for each column. Another run involved manually selected EDX spot measurements of the clay matrix avoiding any visible grains (referred to as 'spot measurements'). The spot measurements were performed within a region of 40 mm × 0.45 mm. The Fe profile, expressed as Fe/Al ratio, depicts a distinct decrease as a function of distance from the Fe metal surface within the first ~10 mm (Figure 11a). Zooming close to the Fe contact (Figure 11b, note logarithmic scale) and including the spot analyses in the corrosion layer, the strong enrichment is observed to be limited to ~150 μm from the Fe contact. In this zone, a steep Fe drop is indicated, which is followed further out by a much flatter Fe decrease. Furthermore, the profile also suggests slightly greater Fe/Al levels in the area 10–22 mm from the Fe contact but this increase relative to the clay further away is almost within the range (calculated from five measurements of different areas at identical distances from the metal). The fairly small range of the area samples (Figure 11a) indicates a small lateral variation in Fe (and also in the other elements), indicating homogeneous chemical composition in the clay matrix. The data thus suggest that the random error is small, although the systematic error in EDX data may be large (up to 2 wt.% absolute, see the Methods section). The Fe/Al ratios of the clay matrix beyond 21 mm obtained by EDX are 0.11–0.12, slightly smaller than the Fe/Al ratio (0.14) obtained by XRF bulk analysis of the same clay material (Table 2, see section

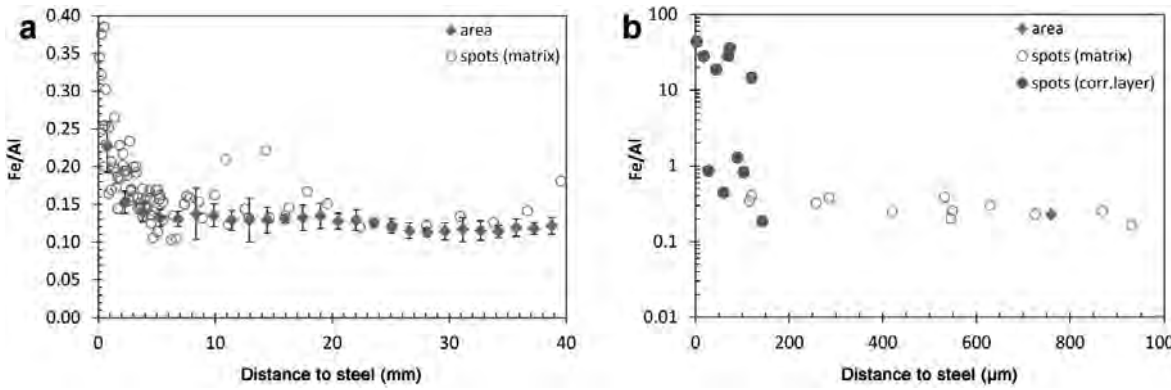

Figure 11. Fe/Al atomic ratio (EDX) as function of distance to the Fe source: (a) area and spot measurements; bars represent the range of five measurements with identical distance to steel; (b) area and spot measurements (in clay matrix as well as corrosion layer) within the first mm.

below). This difference is explained by the systematic error in the EDX measurements.

Image analysis was performed on the Fe maps in order to evaluate whether the Fe enrichment is primarily due to separate Fe particles or not. Relative Fe intensities (gray values) of a total area map of 5.9 mm × 39.5 mm (excluding the corrosion layer) were compared to that in which Fe-rich particles were subtracted by image analysis. The resulting intensities as a function of distance (Figure 12) reveal no significant difference between the total area and the matrix only. This indicates that the Fe enrichment occurs primarily in the clay matrix and is not caused by an enrichment of Fe-rich particles, which make up only 0.4% of the surface (see above). The large scattering in Fe intensities is caused by the very thin stripe analyzed, as well as by an unstable electron beam during the long mapping acquisition.

The main elements of the clay, namely Si and Al, do not exhibit any trend with decreasing distance to the metal surface. The Si/Al ratios of the area measurements as function of distance from the metal contact were found to remain remarkably constant (2.52−2.54) (Figure 13a). The range of the area measurements is small (within the symbols in Figure 13a), suggesting a low random error. The Si/Al ratio obtained from XRF bulk analysis (Table 2) is somewhat higher (2.67−2.69), again suggesting a systematic error in the EDX measurements. The spot analyses from the corrosion layer display more variable Si/Al ratios, but neither a decrease nor an increase relative to the "background" value was observed (Figure 11b).

The Mg profile, expressed as a Mg/Al ratio, calculated from the area measurements, was generally found to display a narrow range of values (~0.15), which corresponds to that obtained from XRF bulk analyses (Table 2). Close to the contact, however, there is a slight increase (Figure 14a). The ratios for the matrix data plot slightly above the area data. The single-spot values in the corrosion layer display two groups (Figure 14b): the first one with only a slight increase in Mg/Al ratio and high Si (*cf.* section on corrosion layer); the second one

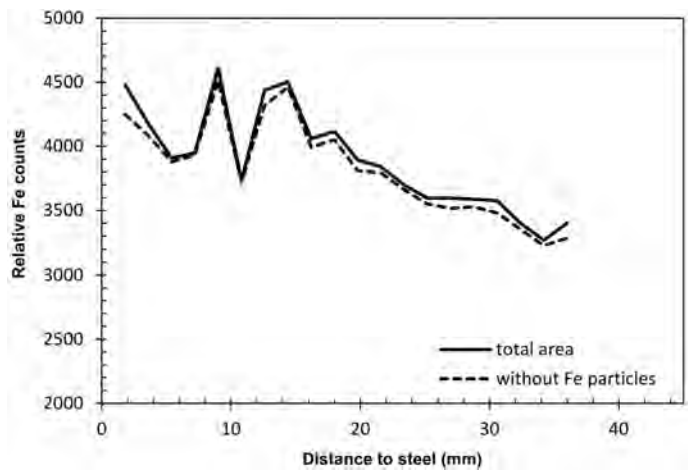

Figure 12. Relative Fe counts obtained by image analysis as a function of distance from the Fe source shown for total area and total area with Fe particles subtracted.

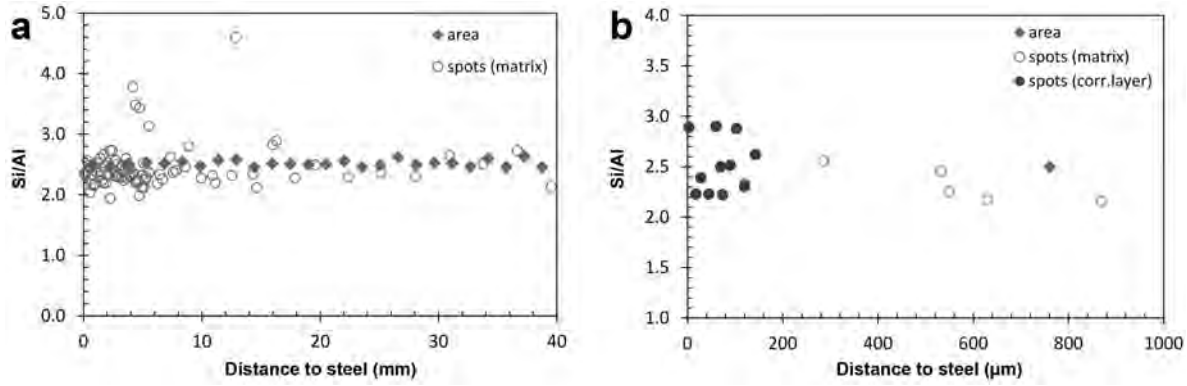

Figure 13. Si/Al atomic ratio as a function of the contact with the Fe source: (a) area and spot measurements; (b) area and spot measurements (in the clay matrix as well as in the corrosion layer) within the first mm. The range of area measurements (five measurements with identical distance from metal) is less than the size represented by the symbols.

with significantly higher Mg/Al ratios and low Si. Siderite, a prominent constituent of the corrosion layer (see above), may incorporate Mg (and Ca) in its lattice. This is probably the main reason for the observed large Mg/Al values compared to the bulk clay. The slightly higher Mg/Al ratios noted for the first group of spot measurements, which contains more Si, Al, and lower Fe contents (*cf.* section on corrosion layer), are similar to the ratios in the matrix close to the contact (see the Discussion section below).

Ca/Na elemental ratios of the total area analyses show important variations between 0.39 and 0.70, but no trend with regard to distance from the metal source (data not shown). The large variation is interpreted as a consequence of the inhomogeneous distribution of calcite and anhydrite particles in the clay in the contact area.

DISCUSSION

Quantification of the Fe-transfer process

The amount of Fe transferred to the clay can be estimated roughly from EDX analysis of Fe profiles. The Fe is concentrated in a layer ~10 mm thick (Figure 15). The data also hint at a slight Fe enrichment at a distance of 10−22 mm, but this is close to the range of analytical uncertainty (see the Results section). The background Fe concentration in the clay, $[Fe]_{c,\mathrm{true}}$ (wt.% and g/kg dry clay), is derived from the averaged XRF analyses of the clay not affected by the Fe enrichment front (Table 2). First, the Fe concentrations from (semi)-quantitative EDX data need to be calibrated. This is done by averaging the EDX analyses from the samples located at 25−39 mm from the contact which yields $[Fe]_c$. This apparent background Fe is related to the "true" background Fe by the calibration factor f_c where $[Fe]_{c,\mathrm{true}} = f_c \times [Fe]_c$. The total increase in Fe, ΔM_{Fe}, is obtained by accounting for the cylindrical geometry of the Fe source (Figure 15) and the dry density, ρ_b, of the clay:

$$\Delta M_{\mathrm{Fe}} = \sum_{n=1}^{z} (r_n^2 - r_{n-1}^2)\pi h \rho_b f_c (|Fe|_n - |Fe|_c) \qquad (1)$$

where n is the area number corresponding to the measured Fe concentration $[Fe]_n$ and r_n is the radius of the circle including the radius of the Fe source (r_o) and the distance from the source to the area n; z is the

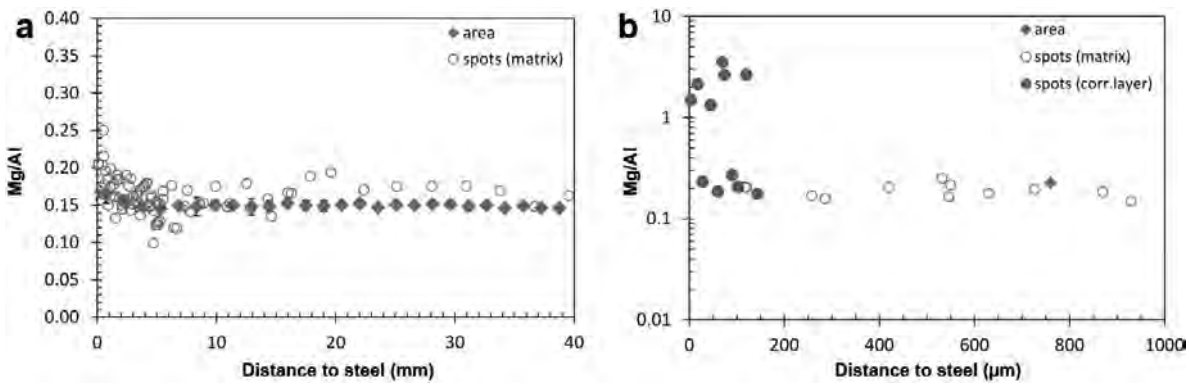

Figure 14. Mg/Al atomic ratio as function of the contact with the Fe source: (a) area and spot measurements; bars represent the range of five measurements with identical distance to steel; (b) area and spot measurements (in the clay matrix as well as in the corrosion layer) within the first mm.

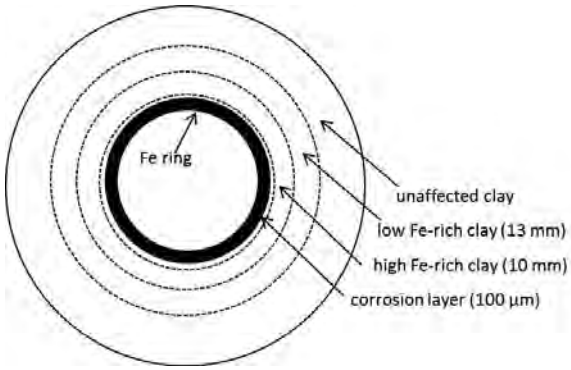

Figure 15. Top view of the inner metal ring of the cage surrounded by the corrosion layer and the Fe-enriched clay layer (not to scale, see text).

number of areas in which Fe is increased. The parameter h is the unit height of the cylinder, taken to be 10 mm.

The amount of Fe transferred to the clay can be converted to the average corrosion depth d_{corr} of the Fe source:

$$d_{corr} = \frac{\Delta M_{Fe}}{\rho_{Fe}} \frac{1}{A_s} \quad (2)$$

where ρ_{Fe} is the density of Fe metal and A_s is the unit surface of the Fe source, equal to $2r_o\pi h$.

In order to estimate a lower and upper range of d_{corr}, two cases (with the parameter values shown in Table 3) were considered.

In the first case, it was assumed that the Fe increase in the clay is limited to the area of ~10 mm and that only 50% of the Fe in the 100 µm thick corrosion layer stems from the corrosion process, the remaining 50% being attributed to the initial corrosion layer before the start of the experiment. The latter assumption is arbitrary as it is not known what the average thickness of the corrosion layer at the start of the experiment was. The calculation yields a corrosion depth of 22.2 µm. Considering a test duration of ~800 days, an average corrosion rate (CR) of ~10 µm/y was deduced.

In the second case, the Fe increase in the clay was assumed to extend to an area distance of 22 mm and that all of the Fe in the corrosion layer stems from the corrosion process. This yields a corrosion depth of 35.3 µm and a corresponding average CR of ~16 µm/y.

The above estimates are associated with considerable uncertainties, but the corrosion rates obtained are not unreasonable. They reflect variable redox and saturation conditions in the corrosion history with residual O_2 occurring in the partially saturated pores of the clay and in the gaps. Upon O_2 consumption by corrosion reactions, conditions changed and became reducing for the remainder of the test period. This process is expected to lead to a significant decrease in the corrosion rates with time (*e.g.* King, 2008). Applying the semi-empirical relationships for a mean CR (mm/y) as a function of temperature (ºK) from Foct and Gras (2003):

$$CR = 1.042 \times e^{-1340/T} \text{ (aerobic conditions)} \quad (3)$$

$$CR = 0.364 \times e^{-1300/T} \text{ (anaerobic conditions for corrosion times of 0.5–15 y)} \quad (4)$$

one obtains, for an average temperature of 100ºC, 29 µm/y and 11 µm/y for aerobic and anaerobic conditions, respectively. The estimated CR values derived above are closer to the anaerobic rate obtained from equation 4.

As a further exercise, an average apparent diffusion coefficient (D_a) for Fe(II) can be estimated from the relationship:

$$x \approx 2\sqrt{D_a t} \quad (5)$$

where x is the mean diffusion distance that a species will have diffused in time t, taken to be 5 mm, and t is the diffusion time, taken to be 800 days. This yields a diffusion coefficient D_a of 9×10^{-14} m^2/s. The calculation implicitly assumes near-saturated conditions, required for Fe^{2+} diffusion to take place. The saturation history in block 3 is not known. Assuming that conditions around the Fe source were saturated for half of the test period only (400 days) and that diffusion under unsaturated conditions is slow compared to saturated ones, then application of the above equation yields a value for $D_a = 1.8 \times 10^{-13}$ m^2/s.

The estimated D_a values are supported by a laboratory study on Fe^{2+} diffusion through bentonite by Xia *et al.* (2005) who evaluated the Fe profile in the

Table 3. Parameters used to estimate corrosion depth (see text).

Parameter	Description	Value	Comment
r_0	Radius of the iron ring	62.0 mm	
ρ_b	Bentonite dry density	1.44 g/cm^3	See Table1
$[Fe]_{b,true}$	'true' background Fe	30.5 g/kg$_{clay}$	Av. conc. of samples C6–C8 from XRF analyses (Table2)
$[Fe]_b$	Measured background Fe	25.1 g/kg$_{clay}$	Av. conc. of EDX area meas., 25–39 mm from Fe contact
H	Height of the cylinder	10 mm	
ρ_{Fe}	Fe density	7.874 g/cm^3	

clay by proposing a fast and slow diffusion process, with $D_a \approx 10^{-12}$ m^2/s and $\approx 10^{-14}$ m^2/s, respectively. D_a values for Ni^{2+}, another divalent transition element, for compacted bentonite were found to be $\sim 5 \times 10^{-12}$ m^2/s (compilation of Yu and Neretnieks, 1997), which is distinctly greater than the values obtained for Fe^{2+} by Xia *et al.* (2005). For diffusion of Co^{2+} in compacted bentonite, Molera and Eriksen (1998) determined D_a values in the range $1-2 \times 10^{-13}$ m^2/s , which is similar to the values for Fe^{2+} estimated here.

Fe–clay interaction and mineral alteration

The Fe phases formed by corrosion of the steel on the other side of the interface with the clay, as identified by Raman spectroscopy, were found to be magnetite, siderite, and, to lesser extent, hematite and Fe(III) oxyhydroxides (goethite and lepidocrocite). This indicates that the sample experienced both reducing and oxidizing conditions, assuming the sample did not experience oxidation during preparation/analysis (see discussion below).

The redox conditions in the test were initially oxidizing with residual air in the unsaturated bentonite material, the inner gap between the steel tube and the cage, and the outer gap between the cage and the rock. As indicated by the presence of siderite and magnetite, conditions switched to reducing, presumably due to the reaction of molecular O_2 with the Fe metal and Fe(II) minerals (*e.g.* pyrite) in the clay (*e.g.* Wersin *et al.*, 1994). After termination of the test, caution was taken during sampling to minimize contamination by O_2. No rigorous measures were taken, however, during sample preparation for EDX and Raman analyses. Thus, the presence of Fe(III) oxyhydroxides may either reflect conditions during the test or O_2 contamination during sample preparation and/or during Raman spectroscopy measurements. On the clay side, both siderite and magnetite as were identified dominant phases in addition to goethite and lepidocrocite close to the contact of the Fe source (100–150 μm). This finding indicates that reduced Fe(II) was at least partly preserved in the sample analyzed by SEM and μ-Raman spectroscopy.

The nature of the Fe phase in the iron-enriched clay matrix could not be identified, but this does not mean that other phases, such as Fe(III) oxyhydroxides or green rusts, did not form. As outlined in the Results section, Fe phases were more difficult to resolve in the clay by μ-Raman spectroscopy. Adjacent to the ~100 μm thick corrosion layer, which consists of a wedge-shaped structure of iron-rich and iron-poor aggregates, only newly formed siderite could be identified. In the Fe-enriched clay, however, most of the Fe is located in the matrix and not in separate particles, as indicated by image analysis. The form in which this Fe occurs is not clear. Various possibilities exist, including: (1) Fe oxyhydroxides (including green rusts); (2) Fe silicates; (3) Fe sorbed to the clay minerals; and (4) incorporation in the octahedral sheet of the clay, are discussed below.

(1) The presence of fine-grained Fe oxyhydroxide precipitates in the clay matrix is a viable possibility. This could be green rust of mixed Fe(II/III) oxidation state (*e.g.* fougerite) or some Fe(III) oxyhydroxide, such as lepidocrocite or ferrihydrite. Poorly crystallized or amorphous Fe oxyhydroxide would not be identified by XRD (Svensson and Hansen, 2013), but was observed using focused ion beam nanotomography combined with transmission electron microscopy (Lukas M. Keller, pers. comm.).

(2) The presence of newly formed Fe silicates, such as Fe serpentines (*e.g.* berthierine, cronstedite) or chlorite (*e.g.* chamosite) is not deemed to be likely. Such phases have not been identified in this study or in previous studies based on the ABM1 test (Kaufhold *et al.*, 2013; Svensson and Hansen, 2013). The characteristic 7 Å (~12.5°2θ Cu$K\alpha$) basal reflection of such non-swelling clays was not observed in any XRD pattern (Figure 4) and have not, to the present authors' knowledge, been identified in other experiments with compacted bentonite in contact with iron under repository-type settings (*e.g.* Carlson *et al.*, 2007).

(3) Fe(II) may be sorbed to the clay, either to interlayer sites by cation exchange reactions, or to edge surface sites by surface complexation (Tournassat, 2003). To evaluate the importance of sorbed Fe(II), it is useful to compare the amounts of measured Fe with the CEC of the clay. The maximum Fe content above the background in the clay observed is ~2 wt.% which corresponds to ~72 meq/100 g as Fe(II). This is close to the CEC (82 meq/100 g) for the reference MX-80 material (Svensson *et al.*, 2011). If all of the increase in Fe were to be sorbed to the clay it would make up almost all of the CEC. This would mean that the main exchangeable cation Na^+ would have been released into solution and moved diffusively along the Na gradient away from the metal. The Na and Na/Al profiles (not shown) indicate no decrease toward the metal contact, however. Sorbed Fe(II) cannot explain all of the measured Fe increase, therefore, but perhaps can account for a small fraction of it.

(4) Incorporation of Fe(II) into the octahedral sheets by substitution is not considered likely because of steric constraints. In fact, experimental data suggest a destabilization of the smectite structure upon reduction of Fe(III) to Fe(II) in the octahedral sheet (Lantenois *et al.*, 2005).

No indication of montmorillonite alteration in the (hot) Fe-clay contact zone from XRD data was found. The same finding was made in other bentonite samples in ABM1 in previous studies by Svensson and Hansen (2013) and Kaufhold *et al.* (2013). This is also supported by EDX analyses pointing to constant Si/Al ratios even in the corrosion layer. The only feature noted from EDX was the slight increase in Mg very close to the metal contact (<1 mm). This increase is not noted from XRF analyses, probably because of the coarser profile data.

The reason for the slight increase remains unclear, but it is interesting to note that a similar trend was observed for other bentonite materials in the ABM1 test (Kaufhold *et al.*, 2013) and also in a previous *in situ* experiment, termed LOT (Long-term Test of Buffer Material) (Karnland *et al.*, 2009). Moreover, an Mg increase in Febex bentonite close to a heating source was observed in a long-term laboratory test (Fernandez and Villar, 2010). Kaufhold *et al.* (2013) suggested tentatively the formation of Mg-rich trioctahedral domains in the clay based on FTIR spectroscopy. On the other hand, Svensson and Hansen (2013) suggested the neo-formation of separate trioctahedral clay phases (*e.g.* saponite).

The weakening of the XRD reflections for cristobalite close to the iron and heat source suggests that some SiO_2 dissolution occurred during the test. Similar XRD observations were made previously on other samples from the ABM1 test (Kaufhold *et al.*, 2013; Svensson and Hansen, 2013) and also in another similar *in situ* test termed TBT (Temperature Buffer Test) in which MX-80 blocks had been exposed to temperatures of up to 150ºC (Svensson and Hansen, 2013).

The increased temperature also induced precipitation of gypsum and anhydrite close to the heat source as shown by XRD and Raman data. Raman data indicate the predominance of anhydrite whereas XRD data indicate the predominance of gypsum. The reason for this difference may be related to the exposure of the XRD samples to air and moisture uptake during sample preparation. This may have induced conversion of anhydrite to gypsum. The presence of anhydrite close to the heat source in other bentonite samples of ABM1 was also found by Kaufhold *et al.* (2013) and the same observation was made in the *in situ* experiment LOT experiment (Karnland *et al.*, 2009).

CONCLUDING REMARKS

In the present microscopic study, a fully homogenized and saturated MX-80 pellet sample exposed to temperatures of up to 115ºC and artificial water for ~800 days close to an iron metal contact from the ABM1 test package was analyzed. The corrosion process led to the formation of a ~100 μm thick corrosion layer containing siderite, magnetite (identified by μ-Raman and XRD) as well as goethite and lepidocrocite (identified by XRD) associated with the montmorillonitic clay. On the rear side of the metal, which had been in direct contact with water during the test, hematite could also be identified. The formation of Fe(II) mineral phases demonstrates the reducing conditions in the *in situ* test. The presence of Fe(III) oxyhydroxides may either reflect the early oxic conditions in the test or be related to O_2 contamination during sample preparation and/or μ-Raman analysis.

Most of the Fe released by corrosion of metal infiltrated the first 10 mm of the clay. The Fe profiles from EDX analysis hint at a maximum distance of ~22 mm of increased Fe levels in the clay. From mass-balance considerations, Fe corrosion depleted an Fe metal layer of ~22−35 μm average thickness, which corresponds to an average corrosion rate of ~10−16 μm/y. In view of the variable redox conditions, the corrosion rate was also likely to be variable, albeit decreasing during the test. The estimated values are similar to those proposed for 'short-term' anaerobic iron corrosion rates at 100ºC, however, suggesting that test conditions were mostly anaerobic.

From the observed Fe enrichment front, an average apparent diffusivity for Fe^{2+} was also estimated to be in the range $1-2\times10^{-13}$ m^2/s. This is similar to the Fe^{2+} diffusivities determined in Kunigel bentonite (Xia *et al.*, 2005).

The corrosion-derived Fe that diffused into the clay beyond the corrosion layer occurs predominantly in the clay matrix and not in discrete Fe particles. The nature of this Fe could not be identified. From the current data, fine-grained Fe oxyhydroxides, presumably in a mixed Fe(II/III) oxidation state, seem most likely. Sorbed Fe may constitute only a minor proportion of the total Fe transferred.

No indication of montmorillonite transformation or newly formed clay phases was found. Thus, no Fe-rich silicates, such as 1:1 clays, trioctahedral smectite, or newly-formed illite were observed. This finding confirms previous XRD results on different bentonite materials in the ABM1 tests. The EDX data indicate a slight increase in Mg in the clay close to the contact, confirming the result obtained by Kaufhold *et al.* (2013) and also data from the LOT experiment (Karnland *et al.*, 2009). The reason for this Mg increase close to the metal heater has not been resolved here. According to the work of Svensson and Hansen (2013) and Kaufhold *et al.* (2013) the enrichment may be related to the formation of trioctahedral smectites.

The stability of montmorillonite in contact with steel and exposed to rather elevated temperatures for ~2.5 y in a repository-like setting shown in these experiments is generally consistent with previous studies with similar settings (Karnland *et al.*, 2009; Fernandez and Villar, 2010; Kaufhold *et al.*, 2013; Svensson and Hansen, 2013).

Future analysis of the test packages ABM2 and ABM3, exposed to heat and Fe-bentonite interaction for longer time periods, will enable more conclusive statements on montmorillonite stability in repository settings. The study presented here is considered to represent a good basis for further investigations of Fe−bentonite interaction, notably on ABM samples exposed to corroding iron for longer periods of time.

ACKNOWLEDGMENTS

The authors thank Margarita Koroleva for her support with sampling and laboratory work, Thomas Aebi for sample preparation, and Urs Eggenberger and Samuel

Gilgen for their help with XRD and XRF analyses. Olivier Leupin (NAGRA) and Daniel Svensson (SKB) and Thomas Gimmi are acknowledged for fruitful discussions. The reviews by Michael Velbel, Eric Ferrage, Nicolas Michau and two anonymous reviewers helped significantly to improve this paper. This work was supported partially by NAGRA.

REFERENCES

Bradbury, M., Berner, U., Curti, E., Hummel, W., Kosakowski, G., and Thoenen, T. (2014) The long term geochemical evolution of the nearfield of the HLW repository. NAGRA Technical Report NTB 12-01, Wettingen, Switzerland. www.nagra.ch/en/downloadcentre.htm

Carlson, L., Karnland, O., Oversby, V.M., Rance, A.P., Smart, N.R., Snellman, M., Vähänen, M., and Werme, L.O. (2007) Experimental studies of the interactions between anaerobically corroding iron and bentonite. *Physics and Chemistry of the Earth*, **32**, 334–345.

Carrado, K.A. and Komadel, P. (2009) Acid activation of bentonites and polymer–clay nanocomposites. *Elements*, **5**, 111–116.

Charpentier, D., Devineau, K., Mosser Ruck, R., Cathelineau, M., and Villieras, F. (2006) Bentonite–iron interactions under alkaline condition: An experimental approach. *Applied Clay Science*, **32**, 1–13.

Christidis, G.E. and Huff, W.D. (2009) Geological aspects and genesis of bentonites. *Elements*, **5**, 93–98.

De Combarieu, G., Schlegel, M.L., Neff, D., Foy, E., Vantelon, D., Barboux, P., and Gin, S. (2011) Glass-iron-clay interactions in a radioactive waste geological disposal: An integrated laboratory-scale experiment. *Applied Geochemistry*, **26**, 65–79.

Didier, M., Leone, L., Greneche, J.-M., Giffaut, E., and Charlet, L. (2012) Adsorption of hydrogen gas and redox processes in clays. *Environmental Science and Technology*, **46**, 3574–3579.

Dohrmann, R., Olsson, S., Kaufhold, S., and Sellin, P. (2013) Mineralogical investigations of the first package of the alternative buffer material test. II. Exchangeable cation population rearrangement. *Clay Minerals*, **48**, 215–233.

Eisenhour, D.D. and Brown, R.K. (2009) Bentonite and its impact on modern life. *Elements*, **5**, 83–88.

Eng, A., Nilsson, U., and Svensson, D. (2007) Äspö Hard Rock Laboratory. Alternative Buffer Material. Installation report. SKB International Progress Report IPR-07-15, Stockholm, Sweden. http://www.skb.com/publication/1633130/

Fernández, A.M. and Villar, M.V. (2010) Geochemical behaviour of a bentonite barrier in the laboratory after up to 8 years of heating and hydration. *Applied Geochemistry*, **25**, 809–824.

Foct, F. and Gras, J.-M. (2003) Semi-empirical model for carbon steel corrosion in long term geological nuclear waste disposal. Pp. 92–102 in: *Prediction of Long Term Corrosion Behaviour in Nuclear Waste Systems* (D. Ferron and D.D McDonald, editors). European Federation of Corrosion. ISBN 1902653874.

Gates, W.P., Bouazza, A., and Churchman, G.J. (2009) Bentonite clay keeps pollutants at bay. *Elements*, **5**, 105–110.

Gaudin, A., Gaboreau, S., Tinseau, E., Bartier, D., Petit, S., Grauby, O., Foct, F., and Beaufort, D. (2009) Mineralogical reactions in the Tournemire argillite after *in situ* interaction with steels. *Applied Clay Science*, **43**, 196–207.

Guillaume, D., Neaman, A., Cathelineau, M., Mosser-Ruck, R., Pfeiffert, C., Abdeloula, M., Dubessy, J., Villéras, F., Baronnet, A., and Michau, N. (2003) Experimental synthesis of chlorite from smectite at 300ºC in the presence of metallic Fe. *Clay Minerals*, **38**, 281–302.

Guillaume, D., Neaman, A., Cathelineau, M., Mosser-Ruck, R., Peiffert, C., Abdelmoula, M., Dubessy, J., Villiéras, F., and Michau, N. (2004) Experimental study of the transformation of smectite at 80 and 300ºC in the presence of Fe oxides. *Clay Minerals*, **39**, 17–34.

Güven, N. (2009) Bentonites – clays for molecular engineering. *Elements*, **5**, 89–92.

Jodin-Caumon, M.-C., Mosser-Ruck, R., Rousset, D., Randi, A., Cathelineau, M., and Michau, N. (2010) Effect of a thermal gradient on iron-clay interactions. *Clays and Clay Minerals*, **58**, 667–681.

Jodin-Caumon, M.-C., Mosser-Ruck, R., Randi, A., Pierron, O., Cathelineau, M., and Michau, N. (2012) Mineralogical evolution of a claystone after reaction with iron under thermal gradient. *Clays and Clay Minerals*, **60**, 443–455.

Johnson, L., Marschall, P., Wersin, P., and Gribi, P. (2008) HMCBG processes related to the steel components in the KBS-3H disposal concept. SKB Report R-08-25, SKB, Stockholm, Sweden. 127 pp. http://www.skb.com/publication/1857594/

Karnland, O., Olsson, S., and Nilsson, U. (2006) Mineralogy and sealing properties of various bentonites and smectite-rich clay materials. SKB Technical Report TR-06-30, Stockholm, Sweden. http://www.skb.com/publication/1419144/

Karnland, O., Nilsson, U., Weber, H., and Wersin, P. (2008) Sealing ability of Wyoming bentonite pellets foreseen as buffer material – laboratory tests. *Physics and Chemistry of the Earth*, **33**, S472–S475.

Karnland, O., Olsson, S., Dueck, A., Birgersson, M., Nilsson, U., and Hernan-Hakansson, T. (2009) Long term test of buffer material at the Äspö Hard Rock Laboratory, LOT project. Final report on the A2 test parcel. SKB Technical Report TR-09-29, Stockholm, Sweden. http://www.skb.com/publication/1961944/

Kaufhold, S., Dohrmann, R., Sanden, T., Sellin, P., and Svensson, D. (2013) Mineralogical investigations of the first package of the alternative buffer material test. I. Alteration of bentonites. *Clay Minerals*, **48**, 199–213.

King, F. (2008) Corrosion of carbon steel under anaerobic conditions in a repository for SF and HLW in Opalinus Clay. NAGRA Technical Report NTB 08-12, Wettingen, Switzerland. www.nagra.ch/en/downloadcentre.htm

Kumpulainen, S., Carlsson, T., Muurinen, A., Kiviranta, L., Svensson, D., Sasamoto, H.,Yui, M., Wersin, P., and Rosch, D. (2010) Long-term alteration of bentonite in the presence of metallic iron. Posiva Working Report 2010-71, Olkiluoto, Finland and SKB Report R-10-52, Stockholm, Sweden. http://www.skb.com/publication/2255832/

Lanson, B., Lantenois, S., Van Aken, P.A., Bauer, A., and Plançon, A. (2012) Experimental investigation of smectite interaction with metal iron at 80ºC: Structural characterization of newly formed Fe-rich phyllosilicates. *American Mineralogist*, **97**, 864–871.

Lantenois, S., Lanson, B., Mulller, F., Bauer, A., Jullien, M., and Plançon, A. (2005) Experimental study of smectite interaction with metal Fe at low temperature: 1. Smectite destabilization. *Clays and Clay Minerals*, **53**, 597–612.

Martin, F.A., Bataillon, C., and Schlegel, M.B. (2008) Corrosion of iron and low alloyed steel within a water saturated brick of clay under anaerobic deep geological disposal conditions: An integrated experiment. *Journal of Nuclear Materials*, **379**, 80–90.

Marty, N.C.M., Fritz, B., Clément, A., and Michau, N. (2010) Modelling the long term alteration of the bentonite barrier in an underground radioactive waste repository. *Applied Clay Science*, **47**, 82–90.

Meier, L.P. and Kahr, G. (1999) Determination of the cation exchange capacity (CEC) of clay minerals using the complexes of copper(II) ion with triethylenetetramine and tetraethylenepentamine. *Clays and Clay Minerals*, **47**, 386–388.

Molera, M. and Eriksen, T.E. (1998) Cation diffusion in compacted bentonite. *Mineralogical Magazine*, **62A**, 1007–1008.

Mosser-Ruck, R., Cathelineau, M., Guillaume, D., Charpentier, D., Rousset, D., Barres, O., and Michau, N. (2010) Effects of temperature, pH, and iron/clay and liquid/clay ratios on experimental conversion of dioctahedral smectite to berthierine, chlorite, vermiculite, or saponite. *Clays and Clay Minerals*, **58**, 280–291.

NAGRA (2002) Project Opalinus Clay: Safety report. Demonstration of disposal feasibility for spent fuel, vitrified high-level waste and long-lived intermediate-level waste (Entsorgungsnachweis). NAGRA Technical Report NTB 02-05, Wettingen, Switzerland.
www.nagra.ch/en/downloadcentre.htm

NAGRA (2009) Performance of bentonite as buffer and sealing material: Status of R and D programme. NAGRA Arbeitsbericht NAB 09-12, Wettingen, Switzerland.
www.nagra.ch/en/downloadcentre.htm

NAGRA (2011) Alternative Buffer Material – Status report. NAGRA Arbeitsbericht NAB 11-19, NAGRA, Wettingen, Switzerland.
www.nagra.ch/en/downloadcentre.htm

Osackýa, M., Šucha, V., Czímerová, A., and Madejová, J. (2010) Reaction of smectites with iron in a nitrogen atmosphere at 75ºC. *Applied Clay Science*, **50**, 237–244.

Papillon, F., Jullien, M., and Bataillon, C. (2001) Carbon steel behaviour in compacted clay: two long-term tests for corrosion prediction. Pp. 439–454 in: *Prediction of Long Term Corrosion, Behaviour in Nuclear Waste Systems*. (D. Feron and D.D. MacDonald, editors). European Federation of Corrosion Publications.

Perronnet, M., Jullien, M., Villieras, F., Raynal, J., Bonnin, D., and Bruno, G. (2008) Evidence of a critical content in Fe(0) on FoCa7 bentonite reactivity at 80ºC. *Applied Clay Science*, **38**, 187–202.

POSIVA (2013) Safety case for the disposal of spent nuclear fuel at Olkiluoto. Report Posiva 2012–14, Olkiluoto, Finland.
www.posiva.fi/en/databank/posiva_reports#.VM4v0yxARrQ

Schlegel, M.L., Bataillon, C., Blanc, C., Prêt, D., and Foy, E. (2010) Anodic activation of iron corrosion in clay media under water-saturated conditions at 90 degrees C: characterization of the corrosion interface. *Environmental Science & Technology*, **44**, 1503–1508.

Schlegel, M.L., Bataillon, C., Brucker, F., Blanc, C., Prêt, D., Foy, E., and Chorro, M. (2014) Corrosion of metal iron in contact with anoxic clay at 90ºC: Characterization of the corrosion products after two years of interaction. *Applied Geochemistry*, **51**, 1–14.

SKB (2011) Long-term safety for the final repository for spent nuclear fuel at Forsmark. SKB Technical Report TR-11-01, Stockholm, Sweden.
http://www.skb.com/publication/2345580/

Svensson, D., Dueck, A., Nilsson, U., Olsson, S., Sandén, T., Lydmark, S., Jägerwall, S., Pedersen, K., and Hansen, S. (2011) Alternative buffer material. Status of the ongoing laboratory investigation of reference materials and test package 1. SKB Technical Report TR-11-06, Stockholm, Sweden.
http://www.skb.com/publication/2442994/

Svensson, D., and Hansen, S. (2013) Iron redox chemistry in two iron-bentonite field experiments at Äspö Hard Rock Laboratory, Sweden – studied by Fe K XANES and XRD. *Clays and Clay Minerals*, **61**, 566–579.

Tournassat, C. (2003) Cations–clays interactions: the Fe(II) case. Application to the problem of the French deep nuclear repository field concept. PhD thesis, University of Grenoble, France, 199 pp.

Wersin, P. and Birgersson, M. (2014) Reactive transport modelling of iron-bentonite interaction within the KBS-3H disposal concept: the Olkiluoto site as a case study. Pp. 237–250 in: *Clays in Natural and Engineered Barriers for Radioactive Waste Confinement* (S. Norris, J. Bruno, M. Cathelineau, P. Delage, C. Fairhurst, E.C. Gaucher, Höhn, E.H., A. Kalinichev, P. Lalieux, and P. Sellin, editors). Special Publications, **400**, Geological Society, London.

Wersin, P., Spahiu, K., and Bruno, J. (1994) Time evolution of dissolved oxygen and redox conditions in a HLW repository. SKB Technical Report TR 94-02, Stockholm, Sweden.
http://www.skb.com/publication/9933/

Wersin, P., Johnson, L., and Schwyn, B. (2004) Assessment of redox conditions in the near field of nuclear waste repositories: Application to the Swiss high-level and intermediate level waste disposal concept. *MRS symposium proceedings*, **807** (V.M. Oversby and L.O. Werme, editors). Materials Research Society (MRS), Pittsburgh, Pennsylvania, pp. 539–544. (Scientific basis for nuclear waste management XXVII: Symposium held 15–19 June, 2003, Kalmar, Sweden.)

Wersin, P., Birgersson, M., Olsson, S., Karnland, O., and Snellman, M. (2007) Impact of corrosion-derived iron on the bentonite buffer within the KBS-3H disposal concept – the Olkiluoto site as case study. Posiva Report 2007-11, Olkilouto, Finland.
www.posiva.fi/en/databank/posiva_reports#.VM4v0yxARrQ

Whitney, D.L. and Evans, B.W. (2010) Abbreviations for names of rock-forming minerals. *American Mineralogist*, **95**, 185–187.

Williams, L.B., Haydel, S.E., and Ferrell, R.E. Jr. (2009) Bentonite, bandaids, and Borborygmi. *Elements*, **5**, 99–104.

Wilson, J., Cressey, G., Cressey, B., Cuadros, J., Ragnarsdottir, K.V., Savage, D., and Shibata, M. (2006) The effect of iron on montmorillonite stability: (II) Experimental investigation. *Geochimica et Cosmochimica Acta*, **70**, 323–336.

Wollenberg, R. and Schröder, H. (2006) Herstellung und Charakterisierung von Bentonitsystemen für den Einsatz als Versiegelungsmaterial (Fabrication and characterization of bentonite systems for the use as sealing material). NAGRA Arbeitsbericht NAB 06-20, Wettingen, Switzerland.

Xia, X., Idemitsu, K., Arima, T., Inagaki, Y., Ishidera, T., Kurosawa, S., Iijima, K., and Sato, H. (2005) Corrosion of carbon steel in compacted bentonite and its effect on neptunium diffusion under reducing condition. *Applied Clay Science*, **28**, 89–100.

Yu, J.-W. and Neretnieks, I. (1997) Diffusion and sorption properties of radionuclides in compacted bentonite. SKB Technical Report TR 97-12, Stockholm, Sweden.
http://www.skb.com/publication/13606/

(*Received 16 September 2014; revised 18 March 2015; Ms. 913; AE: E. Ferrage*)

Clays and Clay Minerals, Vol. 63, No. 1, 69–72, 2015.

CORRIGENDA

In the paper "Mineralogy, geochemistry, and genesis of mudstones in the Upper Miocene Mustafapaşa member of the Ürgüp Formation in the Cappadocia region, central Anatolia, Turkey'' from *Clays and Clay Minerals*, Vol. **62** (2014), 267−285, by Külah *et al*.

Page 276: Change the average value of Cr in the ophiolitic rocks from 1850 ppm to 2530 ppm.

Page 276: Change the average values of Cr from the south and the north in the mudstones of the Mustafapaşa member from 475 to 556 ppm and from 136 to 66 ppm, respectively.

Page 276: Replace "LaN/Yb_N ratios from 0.41 to 5.96" with "average LaN/Yb_N ratios from 0.42 to 1.13".

Page 276: Replace the paragraph that begins with "The averages" with "The NASC-normalized *REE* patterns for mudstones show mostly small positive Eu and Yb anomalies and small negative Ce anomalies. The ranges are $(Eu/Eu^*)_{NASC}$ = 0.99−1.40, $(Yb/Yb^*)_{NASC}$ = 0.98−1.17, and $(Ce/Ce^*)_{NASC}$ = 0.75−1.06 (Table 2, deposited)."

Page 284: Delete "and ophiolites" from the first sentence.

Figure 7: Replaced by new figure below.

Figure 10: Replaced by new figure below.

Figure 11d: Replaced by new figure below.

Figure 12: Replaced by new figure below.

Replace Table 2 with the corrected table below. A corrected long version of Table 2 has been deposited with the Editor in Chief and is available from http://www.clays.org/JOURNAL/JournalDeposits.html.

DOI: 10.1346/CCMN.2015.0630106

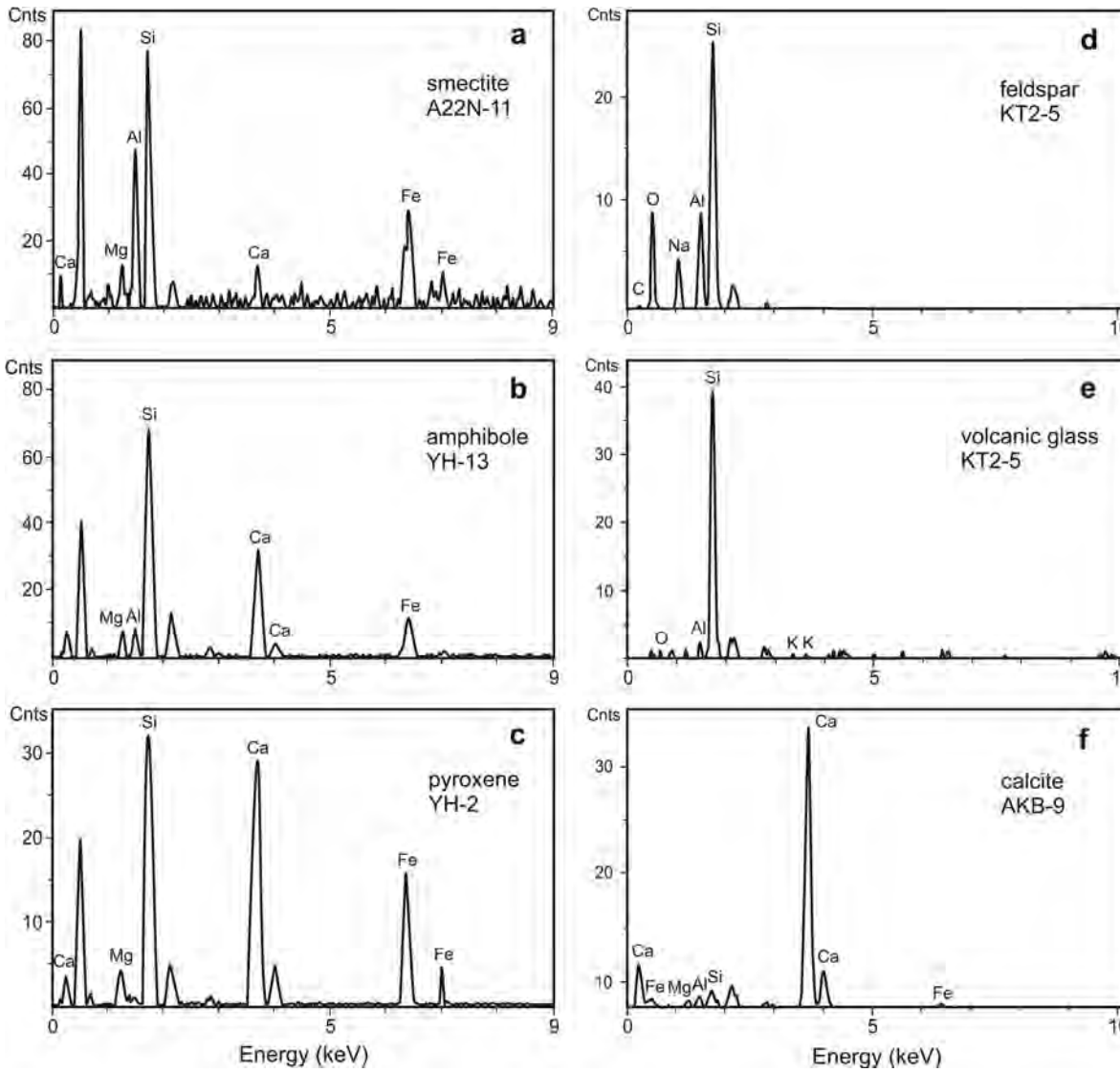

Replacement Figure 7. EDX analyses of smectite and precursors in mudstone samples.

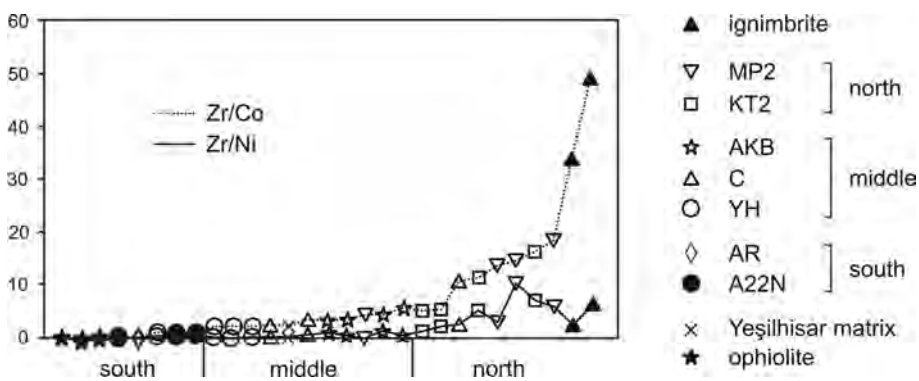

Replacement Figure 10. Plots of Zr/Ni *vs*. Zr/Co for the smectite-dominated mudstone samples from the south, middle, and north of the study area.

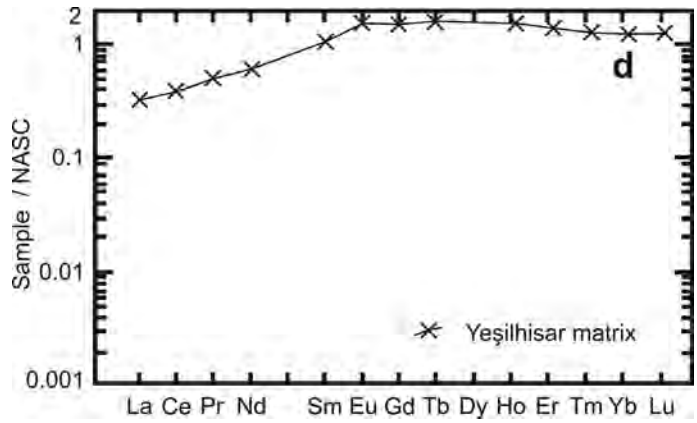

Replacement Figure 11d. NASC-normalized *REE* patterns (Gromet *et al.*, 1984) from the smectite-dominated mudstone samples from: (a) the south; (b) the middle; (c) the north, and (d,e) north of the study area.

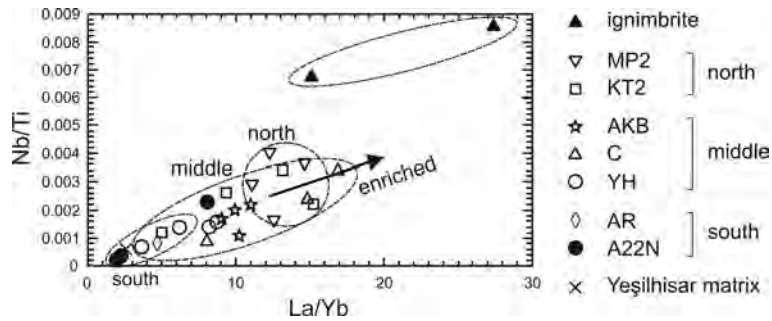

Replacement Figure 12. Plots of La/Nb *vs.* Nb/Ti for the smectite-dominated mudstone samples from the south, middle, and north of the study area.

Table 2. Major oxides (wt.%), trace elements (ppm), and *REE* contents (ppm) of ophiolite, the Yeşilhisar conglomerate matrix, mudstones, and ignimbrites in the study area.

Major oxides (wt.%)	Ophiolite Avg. (n = 3)	Yeşilhisar matrix (n = 1)	Mudstone South Avg. (n = 4)	Mudstone Middle Avg. (n = 11)	Mudstone North Avg. (n = 8)	Ignimbrite Avg. (n = 2)
SiO_2	39.04	58.57	50.35	44.70	57.87	70.20
Al_2O_3	1.10	19.04	16.96	11.70	15.22	14.29
ΣFe_2O_3	8.05	4.58	9.12	6.23	6.11	1.73
MgO	36.51	2.15	4.38	4.24	1.57	0.39
CaO	0.16	1.26	2.71	11.68	3.06	1.76
Na_2O	<0.01	1.83	2.09	1.24	1.57	2.33
K_2O	<0.01	0.41	0.56	0.92	1.74	3.64
TiO_2	⩽0.01	0.68	0.50	0.58	0.56	0.26
P_2O_5	<0.01	0.02	0.04	0.08	0.11	0.03
MnO	0.07	0.02	0.07	0.09	0.06	0.05
LOI	13.80	11.20	12.95	18.29	11.98	5.20
Total	99.76	99.72	99.75	99.83	99.86	
TOT/C	0.10	0.03	0.24	2.42	⩽0.23	<0.03
TOT/S	<0.02	0.03	<0.25	<0.06	⩽0.03	<0.02
Trace elements (ppm)						
Ba	5	61	50	144	609	761
Be	2	2				
Co	98.5	34.8	40.1	26.0	14.8	3.5
Cr	2530	595	556	402	66	79
Cs	<0.1	0.9	3.4	6.2	3.4	5.0
Ga	<0.9	17.3	13.5	10.9	14.2	13.6
Hf	<0.1	2.4	1.4	2.3	3.8	4.2
Nb	<0.1	2.6	3.1	6.0	8.8	11.7
Ni	1917	567	475	226	46	34
Rb	<0.2	10.4	29.3	42.3	76.4	123
Sc	8	44	28	18	12	4
Sn	<1	<1	<1	<1	⩽1	<1
Sr	5.0	72.2	100	216	222	217
Ta	<0.1	0.2	⩽0.2	0.4	0.6	0.9
Th	<0.2	1.5	1.9	5.4	12.7	21.9
U	⩽0.3	0.4	1.9	1.6	2.6	6.5
V	37	255	128	109	72	<10
W	<0.8	<0.5	<1.2	<1.7	2.2	2.7
Zr	0.4	77.1	51.2	85.2	146	148
Y	0.2	38.9	10.3	15.4	19.5	15.6
La	<0.2	9.8	4.7	15.1	24.6	36.9
Ce	<0.2	26.1	10.3	26.7	44.4	60.4
Pr	<0.02	3.87	1.17	3.29	4.87	5.93
Nd	<0.3	19.5	5.3	12.7	17.8	20.0
Sm	<0.05	5.82	1.29	2.63	3.20	3.05
Eu	<0.02	1.96	0.42	0.73	0.85	0.64
Gd	<0.05	7.26	1.58	2.65	3.08	2.60
Tb	<0.01	1.23	0.26	0.42	0.50	0.39
Dy	<0.05	7.30	1.77	2.73	3.20	2.44
Ho	<0.02	1.52	0.37	0.55	0.68	0.52
Er	<0.03	4.62	1.09	1.56	1.93	1.59
Tm	<0.01	0.60	0.16	0.22	0.30	0.26
Yb	<0.06	3.77	1.16	1.55	2.17	1.89
Lu	<0.01	0.56	0.18	0.23	0.34	0.29
Mo	⩽0.1	0.2	0.9	⩽0.3	<0.3	1.5
Cu	12.7	30.3	56.5	24.8	12.5	3.3
Pb	<0.4	3.2	3.8	8.2	5.8	1.7
Zn	18	52	53	39	20	8
As	3.1	4.7	8.1	7.0	14.9	<0.5
Cd	<0.1	<0.1	<0.1	⩽0.1	<0.1	<0.1
Sb	<0.1	<0.1	<0.1	<0.2	⩽0.1	<0.1
Bi	<0.1	<0.1	<0.1	⩽0.1	⩽0.1	<0.1
Ag	<0.1	<0.1	<0.1	<0.1	<0.1	<0.1
Au (ppb)	2.6	<0.5	⩽1.0	<1.4	<1.6	<1.5
Hg	<0.01	<0.01	0.02	<0.02	<0.01	<0.01
Tl	<0.1	<0.1	<0.1	<0.2	⩽0.1	<0.1
Se	<0.5	0.6	<0.5	<0.8	<0.6	<0.5
Σ*REE*	<1.2	132.8	40.0	86.4	127.4	152.4
Σ*LREE*	<0.7	59.3	21.5	57.7	91.7	123.2
Σ*MREE*	<0.20	25.09	5.69	9.71	11.51	9.63